

Project 2020-366

Postdoctoral researcher: Pouria Bahrami Ataabadi – 9397156

Supervisor: Prof. Dr. Marcilio Alves

2024

Abstract

The principal focus of the current project plan for 2024-2025 is to characterize the friction coefficient between various material pairs under different contact pressures (up to 4 MPa) and slip rates (up to 3 m/s). In the previous year (2023), the friction coefficient between a range of soft materials (such as artificial skin, seat covers, airbags, and seat belts) and rigid materials (including durable plastics, aluminum, and steel automotive components) was empirically determined using the friction rig developed in the GMSIE laboratory. However, the GMSIE team and BMW's corresponding engineers identified several issues and inconsistencies. The primary objective of the proposed project plan for 2024-2025 is to address these challenges by troubleshooting, developing a new dynamic friction rig, and re-performing all experimental friction tests (both quasi-static and dynamic) across approximately 20 surface pairs.

Additionally, a comprehensive experimental-numerical study will be conducted to investigate the low-energy impact on Carbon Fiber fiber-reinforced polymer (CFRP) sandwich panels with a Nomex honeycomb core. Two primary pieces of laboratory equipment will be employed: a low-energy drop hammer and a gas gun. The primary aim of this segment of the study is to examine the damage performance of CFRP sandwich panels when subjected to hailstone impact (25 mm diameter), serving as a standard test in the aerospace industry.

Similar to previous academic periods of the project 2020-366, additional experimental tests, not outlined in this project plan but required for industrial contracts with the GMSIE laboratory and projects of students from EPUSP, will be conducted under the supervision of the postdoctoral researcher.

Keywords: Impact on sandwich panels; Nomex honeycomb core; CFRP; Static friction coefficient; Dynamic friction coefficient; Material characterization; New friction test rig.

Introduction

This section is structured into three subsections: (I) Friction Tests, (II) Low-Energy and Hailstone Impact on CFRP Sandwich Panels, and (III) Additional Experimental Tests at the GMSIE Laboratory.

Friction tests

The aims and objectives of the friction study remain consistent with those proposed in the 2023-2024 project plan, specifically, to establish a constitutive model for the friction coefficient of different materials as functions of contact pressure and slip rate. However, in the 2024-2025 project plan, the primary focus initially will be to address and resolve the significant issues and problems associated with the friction rig to mitigate the inconsistency observed during the previous year. Figure 1 depicts the current friction rig located in the GMSIE laboratory. Nineteen pairs of surfaces with varying degrees of softness, such as rubber dummy skin and steel plates, as shown in Figure 2, will be subjected to tests ranging from quasi-static (3 mm/min) to dynamic conditions (1 and 2 m/s) at three distinct contact pressures (1, 2, and 3 MPa).

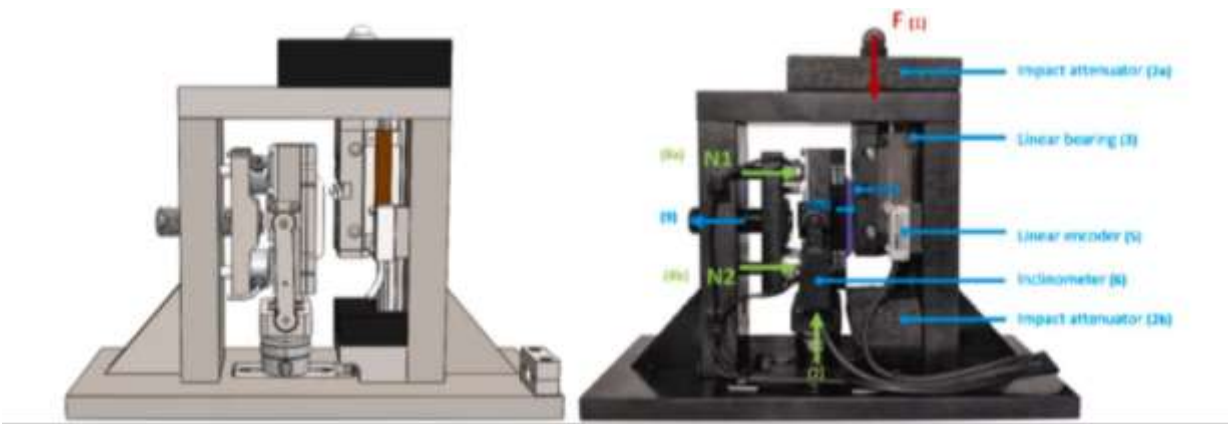
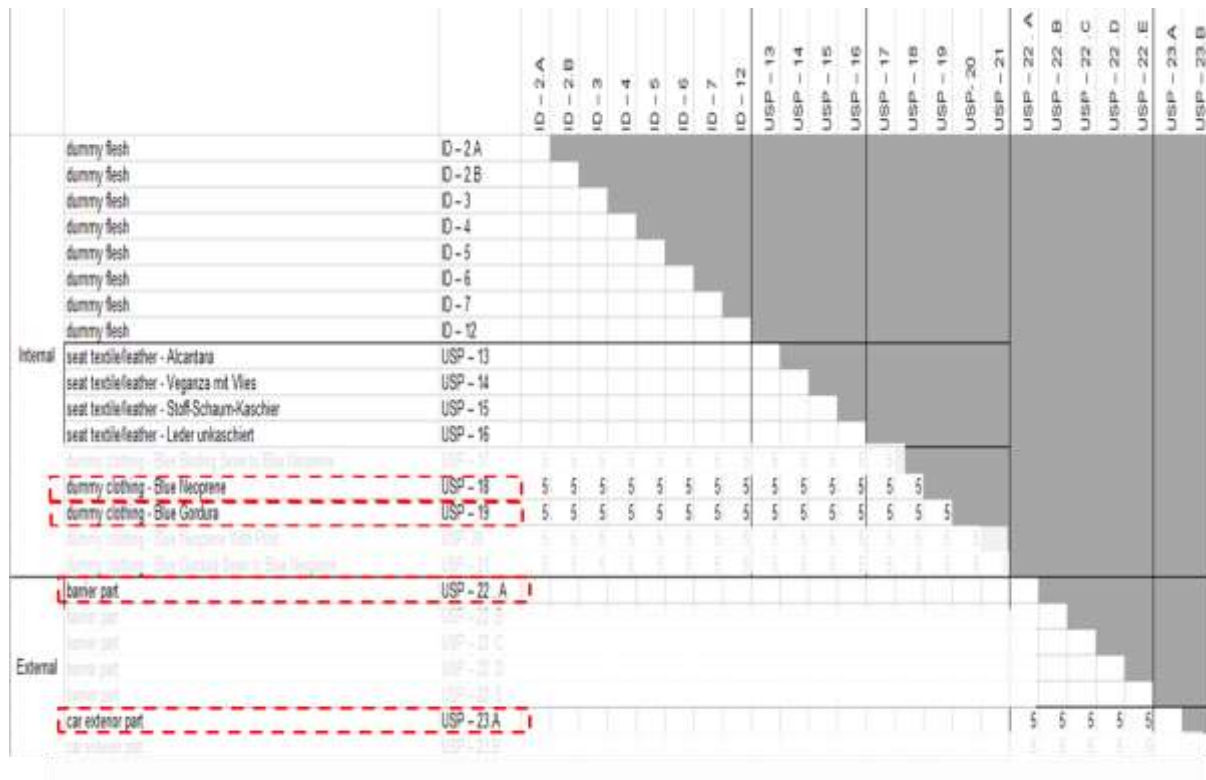
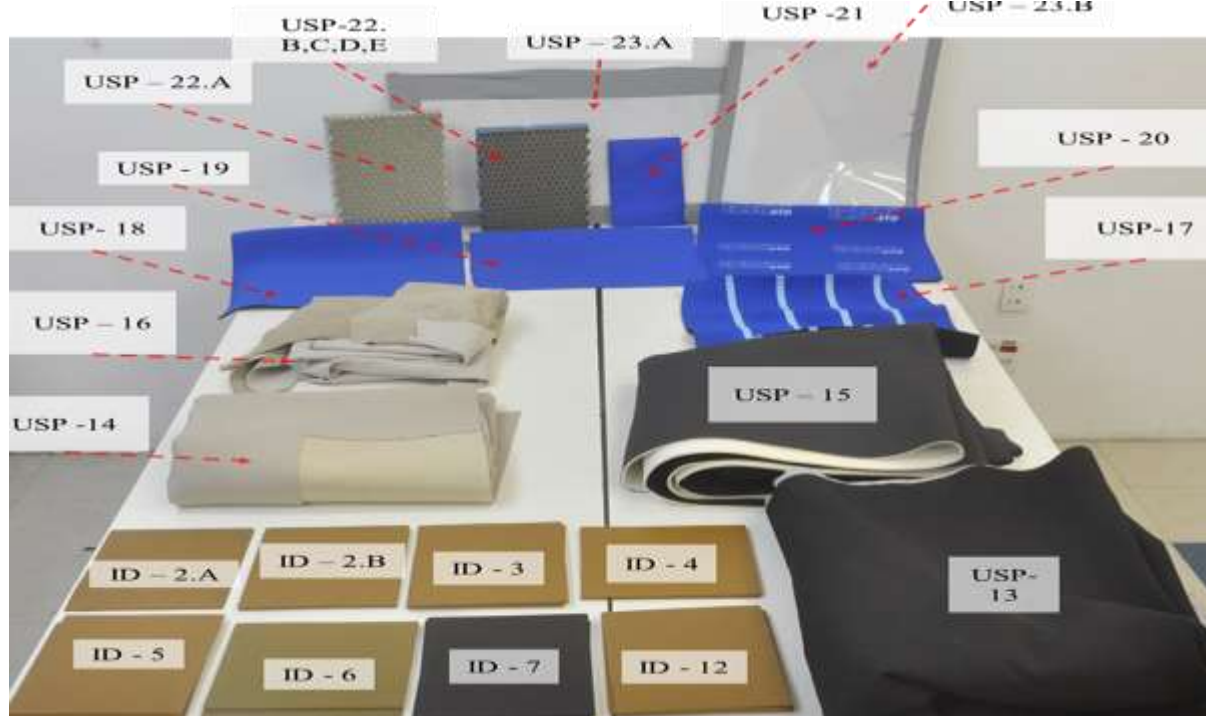


Figure 1: Actual friction rig at GMSIE laboratory



(a): Test matrix.



(b): Surfaces

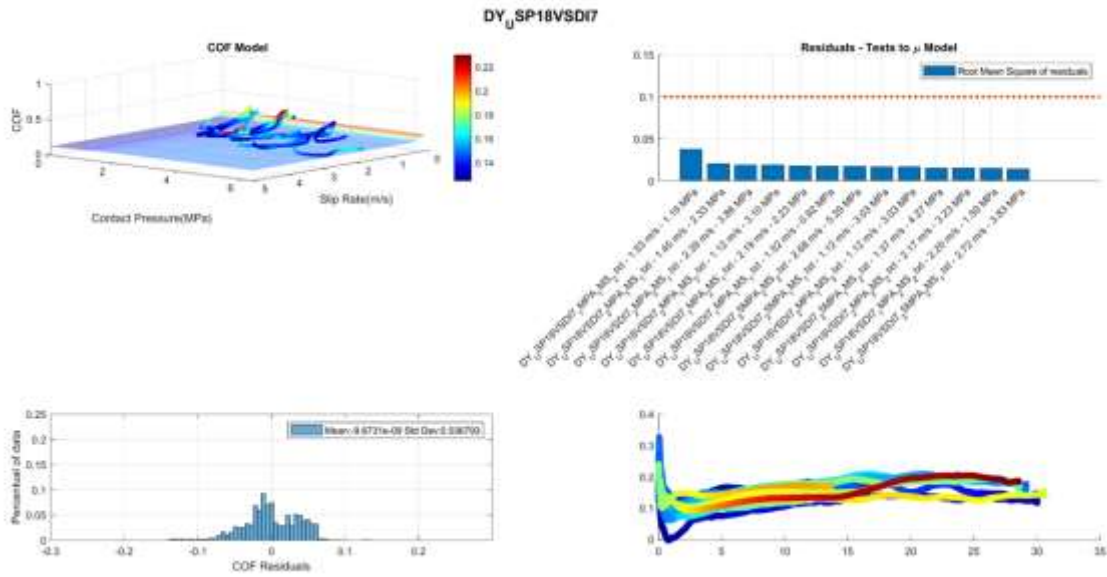
Figure 2: Surface pairs.

During the testing procedure and subsequent analysis of results, several issues were identified, particularly in calibrating the parameters of the friction coefficient constitutive model.

(I) The fixing method that works properly for thin surfaces (up to 3 mm thickness), is not suitable for soft and thick surfaces like dummy skins with 7 mm thickness (samples ID-2A, ID-5 ...).

(II) The sample preparation (fixing on the friction rig) was not user-friendly (around 500 pairs of samples were prepared and glued on the friction rig).

(III) The chosen method for measuring friction and contact (normal) forces, as well as the positioning of the load cells, resulted in unreliable measurements. This issue was particularly prominent in the dynamic friction tests, serving as the primary motivation for redesigning the friction rig. Figures 3 and 4 depict examples of acceptable and poor results from friction tests conducted on rigid and soft materials, respectively.



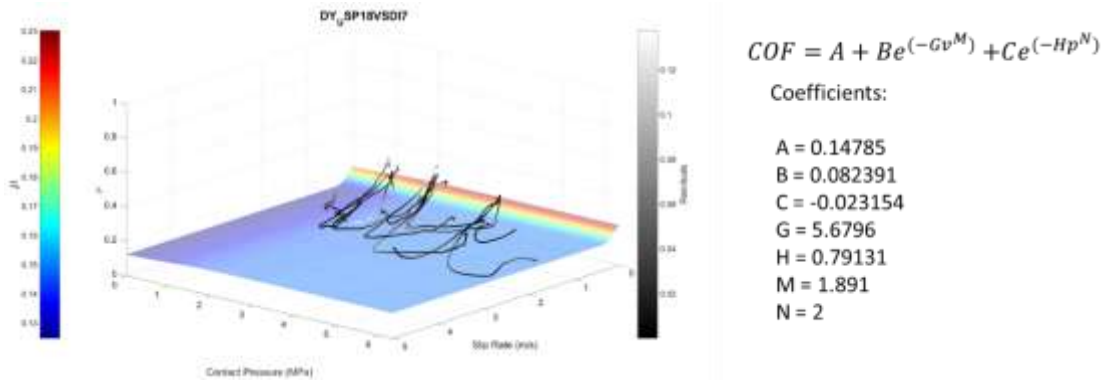


Figure 3: Friction tests for Blue Neouperen (USP-18) vs. dummy flesh (ID7), (Example of tests between hard surface and cloth which led to acceptable results).

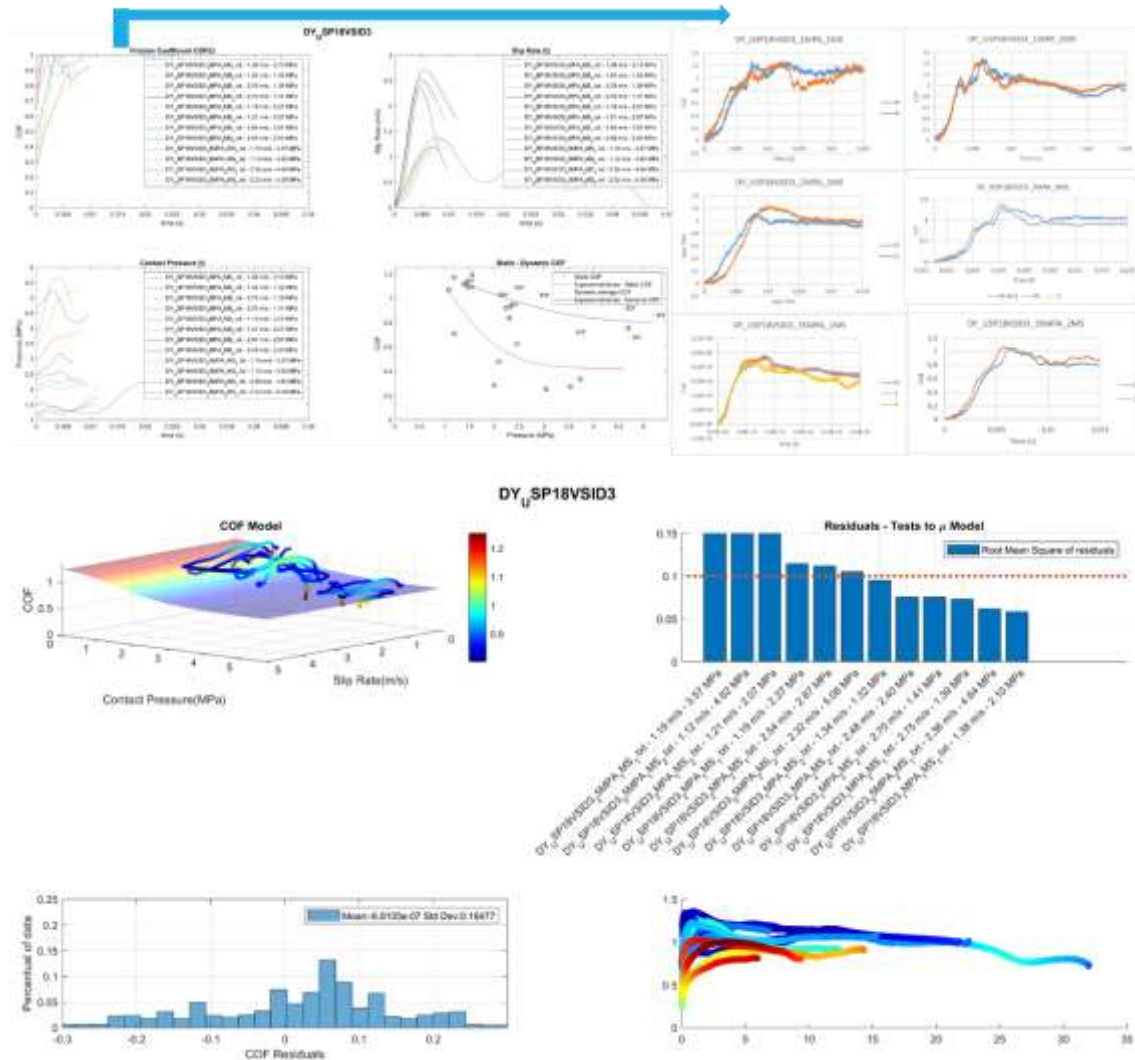


Figure 4: Friction tests for Blue Neouperen (USP-18) vs. dummy flesh (ID3) (Example of tests between soft/thick surface and cloth which led to poor results).

Figure 5 illustrates the schematic presentation of the preliminary design for a new friction rig, aimed at mitigating issues arising from the undesired rotation of the stationary surface. The principal modifications are as follows:

- (I) Three load cells (two for measuring normal force and one for measuring friction force) will be replaced by a tri-axis load cell. This modification will make the friction rig less complicated, and make it possible to restrict the undesired movement of the stationary surface that had been observed during experimental tests.
- (II) Modifying the method of applying high velocities, the actual friction rig uses a low-energy drop hammer to move test surfaces against each other at high velocities (up to 5 m/s). We are trying to replace this method with a linear actuator mechanism that meets the required specifications. Since the linear actuators (with high velocity at around 1 kN bearing load) are expensive, a simple and reliable mechanism will be designed for the new friction rig.

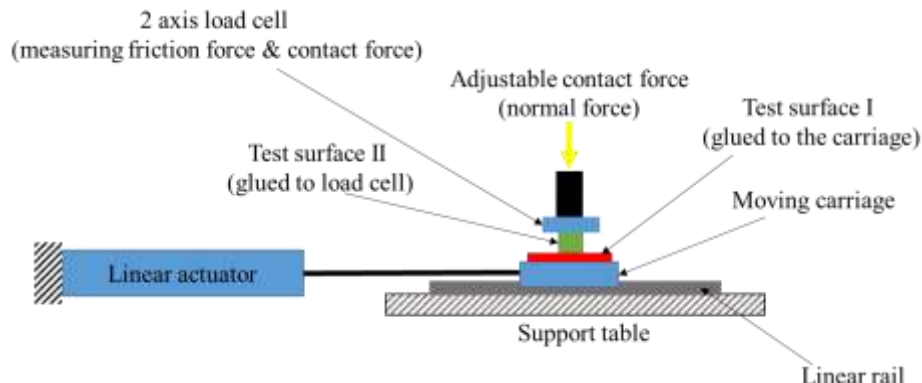


Figure 5: Schematic presentation of new friction rig.

Following the modification of the friction rig, both quasi-static and dynamic tests will be conducted on all surface pairs outlined in the test matrix (Figure 2) across various contact pressures. Subsequently, constitutive models for the friction coefficient will be derived for each surface pair based on the experimental results.

Part II: Low-energy and Hailstone impact on CFRP sandwich panels

Sandwich structures, consisting of two monolithic face sheets and a cellular core, have been extensively employed in the aerospace and transportation industries due to their exceptional mechanical properties and significant weight reduction advantages. Throughout the operational lifespan of these sandwich structures, the impact of external objects, such as debris, hailstones, and shockwaves, poses a substantial safety concern. Over recent decades, considerable attention has been devoted to studying the impact behavior of hybrid sandwich structures composed of composite face sheets and conventional cellular cores.

In the 2022-2023 project plan, which centered on ballistic impact tests conducted on sandwich panels (Figure 6) and aluminum plates, the primary emphasis was placed on the aluminum targets, resulting in a publication in the International Journal of Impact Engineering. The revised project plan will concentrate on the dynamic and damage response of CFRP sandwich panels subjected to two crucial impact scenarios prevalent in the aerospace industry¹. Two impact scenarios on the sandwich panels are as follows (Figure 7):

- (I) Low-energy impact with hemispherical impactor (25 mm diameter), using low-energy drop hammer test at GMSIE laboratory.

Major objectives:

- (a) Dynamic response of CFRP sandwich panel with Nomex honeycomb core to low-energy impact
- (b) Developing a finite element model of low-energy impact on the sandwich panels
- (c) Post-impact residual bending stiffness of impacted sandwich panel, static and cyclic 3-point bending tests.

- (II) Hailstone impact on the CFRP sandwich panel

Major objectives:

¹ For both impact scenarios, the CFRP sandwich panels provided by Embraer will be used.

- (a) Mechanical strength and dynamic response of sandwich panels subjected to hailstone impact (25-30 mm diameter at maximum 90 m/s) using the gas gun at GMSIE laboratory.
- (b) Modeling of hailstone impact using Abaqus/Explicit finite element package.
- (c) Damage assessment on the sandwich panel after impact
- (d) Investigating the post-impact residual strength of the sandwich panel.

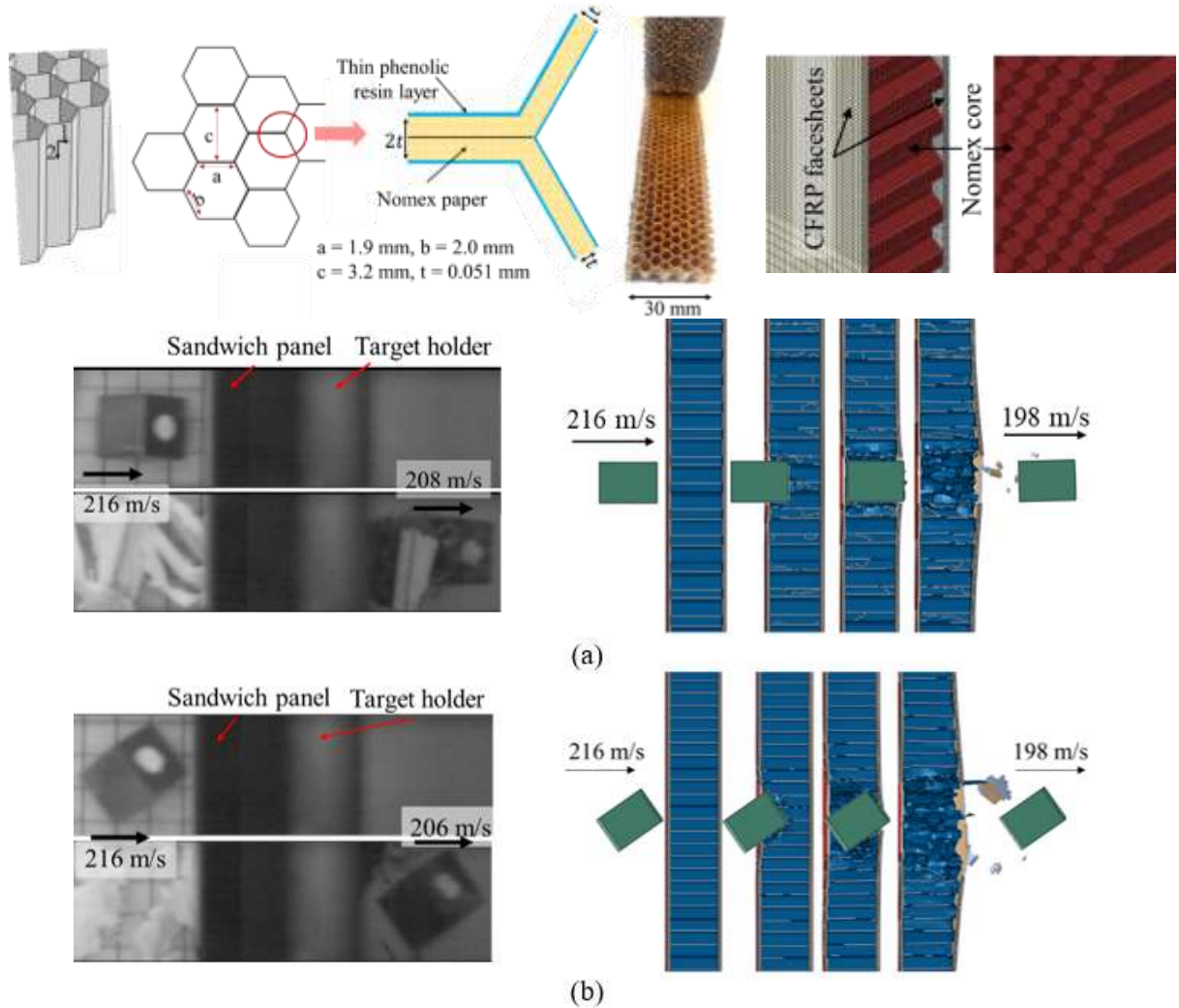
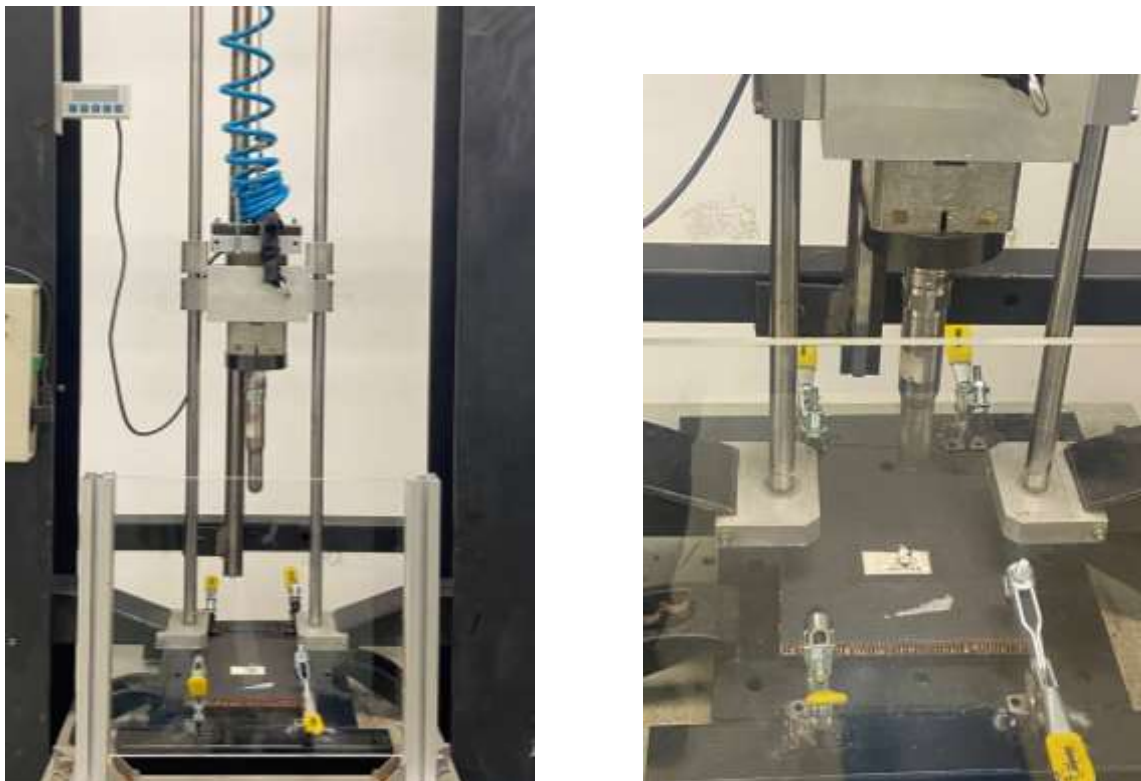
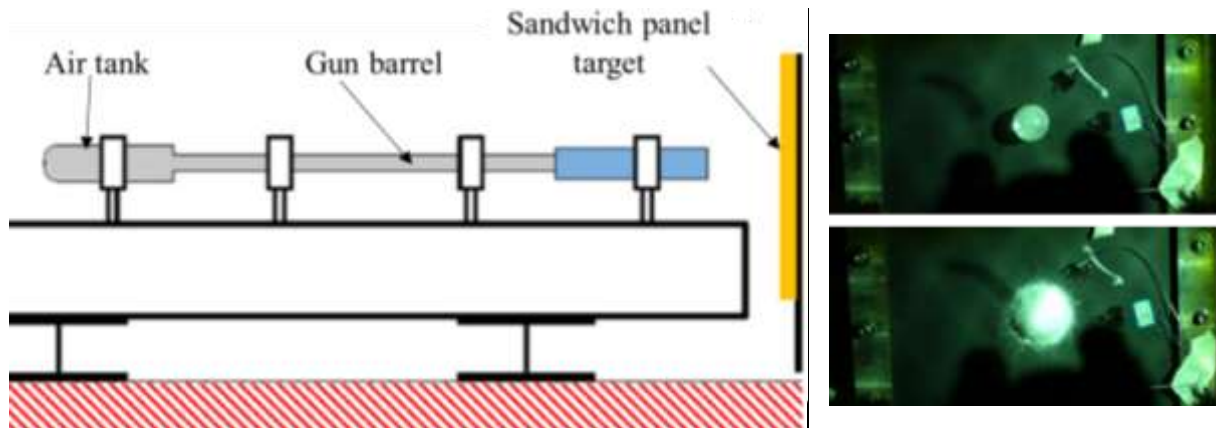


Figure 6: Ballistic impact on the CFRP sandwich panel impacted by the cubical projectile (FE model used a user material subroutine (VUMAT) to model CFTP facesheets.



(a): Low-energy drop hammer rig and sandwich panel fixture



(b) Schematic presentation of gas gun and impact of ice sphere on the sandwich panel

Figure 7: Impact scenarios on the CFRP sandwich panels.

After each impact test, the damage quantity and residual mechanical strength of the impact panel will be assessed using static and cyclic 3-point bending tests (Figure 8).

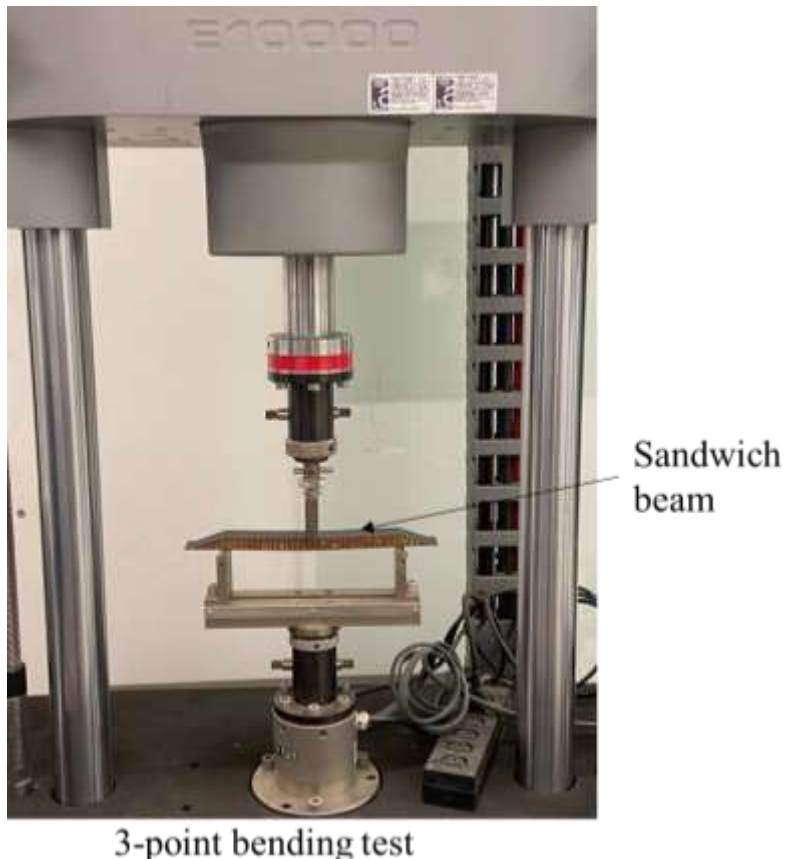


Figure 8: 3-point bending test of the beam cut from the impacted panel (investigating the residual strength of the sample after impact)

Available equipment at the GMSIE laboratory to perform the impact studies on the sandwich panels.

- (i) High-speed cameras
- (ii) Gas gun (developed in the previous phase of the project)
- (iii) Low-energy Dorp hammer rig
- (iv) Optical velocity measurement sensors
- (v) Finite element packages
- (vi) Daq systems with 1.25 MHz sample rate
- (vii) Quasi-static and dynamic universal testing machines (for post-impact residual strength assessment).
- (viii) Dynamic Instron E10000 test machine (fatigue test)

Part III: Additional Experimental Tests at the GMSIE Laboratory (minor projects)

All experimental tests at the GMSIE laboratory, which are part of the contracts with factories, will be carried out by the postdoctoral researcher. The scheduled experimental tests are as follows:

1. Material characterization of steels using quasi-static and high-strain rate (Hopkinson's pressure bar) for Marcopolo company.

....

Activities and timetable

The research duration is segmented into four periods: P1, P2, P3, and P4, as detailed in the subsequent timetable.

A. Activities related to the friction investigation (part I: Friction tests):

- A1. Redesigning the friction test rig to improve the consistency of the results
- A2. Conducting quasi-static (3 mm/min) friction tests on the 20 surface pairs (test matrix Figure 2) at three contact pressures (1, 2,3 MPa).
- A3. Conducting dynamic (1, 2,3 m/s) friction tests on the 20 surface pairs (test matrix Figure 2) at three contact pressures (1, 2,3 MPa).
- A4. Data analysis and calibrating the parameters of friction constitutive equation (function of slip rate and contact pressure).
- A5. Preparing the final report of the friction test²

B. Activities related to the impact on sandwich panels (Part II: Low-energy and hailstone impact on CFRP sandwich panels):

- B.1 Low-energy impacts on sandwich panel (3,6, 12 J) using the small drop hammer

² It is not likely to publish any paper from the friction tests.

B.3 Hailstone impact on the sandwich panels (velocity max 90 m/s) using gas gun apparatus, including preparation of the gas gun, designing sabot for launching hailstone

B4. After impact residual strength assessment on sandwich beam (cut from impacted sandwich panel)

B5. Developing FE model of low impact and ice impact on the sandwich panel and residual strength tests (preliminary FE model of sandwich panel is developed, it requires to be validated for hailstone and low-energy impact).

B6. Preparing and submitting at least one paper for an academic journal.

C. Activities related to high-strain rate material characterization (Part III: Minor projects, the project for Marcopolo company)

C1. Designing tensile specimens for QS and high-strain tensile tests,

C2. Conducting quasi-static tensile test,

C3. Conducting high-strain rate tensile tests using SHTB,

C4. Obtaining the JC plasticity model parameters,

C5. Preparing final report.

Preliminary timetable of activities (2024-2025) is presented in Table 1.

Activity	P1			P2			P3			P4		
A1,B1, C1,C2	Red	Red	Red									
A2,A3,B2				Green	Green	Green	Green	Green				
A4,A5, B4, C3, C4,C5				Green	Green	Green	Blue	Blue	Blue	Blue	Blue	Blue
B5,B6							Yellow	Yellow	Yellow	Yellow	Yellow	Yellow

Publications of 2023-2024



International Journal of Impact Engineering

Volume 187, May 2024, 104913



High-velocity impact performance of AA 7475-T7351 aluminum square plates struck by steel projectiles: Assessing leakage limit velocity

Pouria, B. Ataabadi^a, Caio Magno de Assunção^b, Purnashis Chakraborty^c, Marcilio Alves^a

^a Group of Solid Mechanics and Structural Impact, Department of Mechatronics and Mechanical Systems Engineering, University of São Paulo, São Paulo 05508900, Brazil

^b Department of Mechanical Engineering, Universidade Federal de Itajubá, Brazil

^c Indian Institute of Technology Delhi, New Delhi 110016, India

Received 21 October 2023, Revised 23 January 2024, Accepted 5 February 2024, Available online 10 February 2024, Version of Record 21 February 2024.

International Journal of Rail Transportation >

Latest Articles

Enter keywords, authors, DOI, etc

Submit an article

Journal homepage



Research Article

Dynamic response of polymeric railway sleepers under harsh loading and environmental conditions

P. B. Ataabadi^a, Renato Vargas^b, Marcilio Alves^a

Received 03 Apr 2023, Accepted 12 Oct 2023, Published online: 25 Oct 2023

Cite this article | <https://doi.org/10.1080/23248378.2023.2271507> | Check for updates

Full Article

Figures & data

References

Citations

Metrics

Reprints & Permissions

View PDF

View

Response of a novel all-solid-state sodium-based-electrolyte battery to quasi-static and dynamic stimuli

Bruno G Christoff¹ , Denys Marques^{2,3}, Maisa M Maciel³ ,
Pouria Ataabadi⁴, João Carmo⁵, Maria H Braga⁶, Rui M Guedes^{1,7},
Marcílio Alves⁴ and Volnei Tita^{1,3} 

GQ2 Abstract

GQ4 In response to growing environmental and economic concerns, developing new technologies prioritising safety, sustainability, and reliability has become imperative. In the energy sector, batteries play an increasingly significant role in applications such as powering electronic devices and vehicles. In this context, lithium-ion batteries have raised environmental concerns, driving the exploration of alternative technologies. Sodium-based batteries have emerged as an attractive option due to their environmental and economic advantages, as well as their potential for multi-functional applications. This study investigates a novel battery developed by a research team at the University of Porto, with a specific focus on its strain-sensing capabilities for potential applications in damage detection of structures. The battery under investigation is a novel all-solid-state design, comprised of a sodium-ion ferroelectric electrolyte and Zinc and Copper as the negative and positive electrodes, respectively. A series of quasi-static and dynamic tests are conducted to qualitatively assess the piezoelectric behaviour of the battery. The consistent findings show that the battery generates a difference in the electric potential in response to mechanical stimuli, thus confirming its piezoelectric nature. Furthermore, the results demonstrate the battery can accurately detect the operating frequencies of a shaker, despite encountering inherent electromagnetic interference noise from the electrical grid during testing. These promising outcomes highlight the substantial potential of this emerging technology for a wide range of applications, including but not limited to structural health monitoring systems. Given its novelty, this technology presents multi-functional capabilities for diverse practical future applications, such as energy harvesting that leads to self-powered structural health monitoring systems.

Keywords

Novel piezoelectric battery, sensing capabilities, multi-functional battery, structural health monitoring

Date received: 31 October 2023; accepted: 31 March 2024

The subsequent paper is derived from the postdoctoral project (PIPAE), which was conducted in partnership with the University of São Paulo (USP) in São Carlos and EPUSP-GMSIE. The project was coordinated by Professors Tita and Marcílio from 2022 to 2023.

Project progress and accomplishments		
2021-2022	2022-2023	2023-2024
<p>1. Design a new gas gun (for high-speed and ballistic impact tests)</p> <p>2. Conducting and Finalizing material characterization and lateral impact tests on polymeric composite rail sleepers (For Braskem company)</p> <p>3. Developing VUMAT material subroutine for impact on composite materials (Paper 1, 2)</p> <p>4. Test preparation for ballistic impact test on sandwich panel+Aluminuim plates (launching cubical projectile with precise orientations)</p> <p>5. Conference paper from tests for Braskem (C1, C2)</p>	<p>1. Conducting and finalizing ballistic impact tests on aluminum plates and CFRP sandwich panels (Embraer tests).</p> <p>2. Preparation+submission and revising Paper 3 from partial results of the impact on composite sleepers.</p> <p>3. Conducting extra ballistic tests on the aluminum plates with cubical and spherical projectiles for preparation of paper 3.</p> <p>4. Developing a numerical model of high-velocity impact simulation for Paper 4.</p> <p>5. Designing and performing experimental tests for the PIPAE project at GMSIE-EPUSP (Conference paper C3).</p>	<p>1. Submitting/revising Paper 4 of ballistic impact on CFRP sandwich panel and aluminum plates.</p> <p>2. Reviewing methods of characterization of friction Coefficient as a function of contact pressure and dynamic slip rate (velocity)/preliminary tests and conducting quasi-static and dynamic friction tests on 20 surface pairs.</p> <p>3. Reassembly/minor modification of Split Hopkinson Tensile Bars (SHTB) and practicing tests and analysis of data</p> <p>4. Dynamic material characterization (calibrating Johnson –Cook model) using SHTB apparatus for SENAI</p> <p>5. Dynamic material characterization on tubular steel components (quasi-static and SHTB tests) Johnson- Cook material model and different axial impact tests on tubular energy absorber, for IPT</p>

Paper 1. [Finite element modeling of crushing of CFRP cylindrical tubes under low-velocity axial impact](#), Composite Structures, 2022.

Paper 2. [Finite element modeling of CFRP composite tubes under low-velocity axial impact](#), Polymer Composites 42 (3), 1543-1564, 2021.

C1. [Impact response of polymeric train sleepers](#), Mecsol 2022.

C2. [Polymeric sleepers: a new development methodology](#), 6th BccM conference.

Paper 3. [Dynamic response of polymeric railway sleepers under harsh loading and environmental conditions](#), International Journal of Rail Transportation, 2023.

C3. [Structural Health Monitoring of Thermoplastic Composite Beams via Vibration-based Method](#), Mecsol 2022.

Paper 4. [High-Velocity Impact Performance of AA 7475-T7351 Aluminum Square Plates Struck by Steel Projectiles: Assessing Leakage Limit Velocity](#). International journal of impact engineering, 2024.

Activities 2023-2024

Part 1: numerical and experimental Ballistic impact on the aluminum plates (these tests are different from those we delivered to the Embraer)

Part 2: Dynamic Friction test results (Report is different from that one delivered to BMW)

Part 3: High strain rate material characterization and Axial impact on tubular components, (Report to IPT)

Part 4: High strain rate tensile material characterization, (Report to SENAI)

Part 1

High-Velocity Impact Performance of AA 7475-T7351 Aluminum Square Plates Struck by Steel Projectiles: Assessing Leakage Limit Velocity

Abstract

This paper presents numerical and experimental findings of high-velocity impact tests conducted on thin AA 7475-T7351 aluminum plates subjected to the impact of small cubical and spherical projectiles. The investigation includes an examination of the influence of different impact angles, namely edge-on, corner-on, and face-on orientations, on the target performance. Following each impact test, the damaged plates underwent a leakage test, to determine the leakage threshold caused by the impact event. To gain a deeper insight into the failure modes and penetration mechanisms of thin-walled aluminum plates, finite element models were developed for various impact scenarios. The results revealed that both the shape and orientation of the projectile significantly impact the ballistic and liquid leakage limit velocities of targets. Notably, the cubical projectile exhibited lower ballistic and leakage limits than the spherical projectile. In terms of the leakage limit, a clear correlation was identified between the sharpness of the projectile's nose and leakage limit velocity. As the projectile's nose became sharper, the consistent trend was a decrease in leakage limit velocity i.e. the corner-on impact orientation (having the sharpest nose) exhibited the lowest leakage limit velocity, while the face-on impact orientation (having a blunt nose) displayed the highest leakage limit velocity. However, in contrast to the leakage limit velocity, a definitive relationship between the projectile nose sharpness and ballistic limit velocities was not observed. This is evident as the corner-on impact orientation, associated with the sharpest nose, registered the highest ballistic limit velocity, while the edge-on impact orientation, with an intermediate nose sharpness, recorded the lowest ballistic limit velocity.

Keywords: Ballistic limit velocity; Leakage limit velocity; Impact resistance; Cubical projectile; Impact orientation; Finite element analysis.

1. Introduction

The impact of high-velocity small projectiles, for instance, debris due to uncontained turbine failure, is recognized as a significant hazard that can jeopardize aircraft and passengers' safety.

Consequently, any potential risks stemming from high-velocity projectiles should undergo thorough scrutiny during the initial design phases. Thin-walled aluminum plates find extensive use in the aerospace industry, and while their ballistic performance has been extensively studied, it remains a critical area of investigation.

Depending on the target location (fuselage, fuel tank...) and required level of protection, different limit velocity definitions can be considered. For example, the ballistic limit velocity, the average of the highest striking velocity that results in partial penetration and the lowest striking velocity that causes complete penetration, has been extensively used to assess the high-velocity impact performance of targets. There are three distinct definitions for complete penetration, each with its own criteria: (I) The Navy definition stipulates that the projectile should pass through the plate, penetrating at least one-half of the projectile, (II) The Army definition requires that light should be able to pass through the breached plate and (III) The Protection definition mandates that a thin aluminum sheet (witness) placed six inches behind the target should be perforated either by the projectile or by target debris [1].

The experimental investigation of high-velocity impacts on metallic targets has been extensively explored in prior studies [2–8]. Typically, these studies employ gas gun apparatus to propel projectiles at high velocities toward the target, yielding valuable data on ballistic limit velocity and ballistic curves. Publications in this field often differ primarily in three key aspects: I) the range of velocities examined, II) the shapes and dimensions of projectiles employed, and III) the materials used for both projectiles and targets. Ballistic limits and ballistic curves obtained from experimental investigations in the literature are contingent upon numerous factors, including the shape/size of projectiles, target thickness, target /projectile material, and boundary conditions of the target. Consequently, applying these findings to a new study with differing parameters may not yield precise outcomes in high-velocity impact scenarios [7]. Furthermore, it is important to note that a distinct impact scenario can potentially result in a catastrophic event, even when impact velocities are below the established ballistic limit (with various criteria used for determining this limit). For instance, in the case of uncontained aircraft engine failure, high-velocity small debris may impact the fuselage and fuel tank walls, with hazard levels and consequences varying significantly for each target. While prior experimental studies have contributed valuable insights into failure modes such as petaling, plugging, and dishing, as well as penetration mechanisms in

metallic targets, it becomes evident that specific experimental impact tests are indispensable when addressing a unique impact scenario.

Numerous experimental studies have led to the development of several penetration limit velocity equations, such as the Thor limit velocity equation [9]. Utilizing these equations can offer initial designs without requiring additional experimental tests. However, it is crucial to acknowledge that these equations may provide only approximate predictions, especially when applied to new scenarios involving different target and projectile materials and dimensions than those used to derive the limit velocity equations [1]. In general, these limit velocity equations were formulated based on assumptions and constraints prevalent at the time of their development. For instance, the groundwork for the Thor equation dates back to the 1940s, and its relatively simplistic structure reflects the limited computational capabilities available during that period [10]. Although computational power has seen significant advancements, and commercial finite element software packages have greatly improved in modeling high-velocity dynamic problems, recent research efforts [10–12] have focused on deriving analytical penetration equations based on extensive experimental data.

Given the significant expenses associated with experimental tests and the vast array of potential impact scenarios, finite element models have become indispensable tools in high-velocity impact testing [2–7,12–20]. To ensure the reliability of a finite element model, it necessitates calibration and validation against both quantitative and qualitative outcomes derived from experimental trials. Consequently, at present, an approach combining experimental and numerical methods stands out as the most efficient means of developing new structures expected to encounter high-velocity impacts throughout their operational lifetime.

AA7475-T7351 aluminum finds widespread application in critical aerospace components such as wing spars, stringers, and fuselages [21]. This study focuses on investigating the high-velocity impact performance of thin-walled AA 7475-T7351 aluminum plates. Unlike traditional concerns related to ballistic limits and complete penetration definitions, the primary focus here is on assessing liquid fuel leakage resulting from impact on targets. Specifically, the aim is to determine the leakage limit velocity, which is evaluated as the average of the highest striking velocity that induces damage without leakage and the lowest striking velocity at which liquid (water) begins to escape from the damaged target. After each impact test, the impacted plate was

installed on a pressurized water tank to check for any water droplets. Spherical and cubical projectiles, with three distinct orientations (edge-on, corner-on, and face-on), impacted aluminum plates to assess the effect of the projectile's nose sharpness on the leakage limit velocity, considering different thicknesses of the targets.

A finite element model of the high-velocity impact of small debris on the aluminum plate has been formulated and fine-tuned through calibration using ballistic experimental results. The numerical analysis explores how variations in pitch and yaw from ideal edge-on, corner-on, and face-on orientations affect the leakage and ballistic limit velocities of the aluminum targets.

2. Description of the Experimental and Numerical Studies

2.1 Description of the Experimental Study

The gas gun located in the GMSIE laboratory at the University of São Paulo was employed to launch the projectiles, as illustrated in Fig. 1. To capture high-velocity impact events, three high-speed cameras were positioned; one on the side (lateral), another on top, and the third one at the rear of the plate targets, as depicted in Figs. 2(b-d). Top and side high-speed cameras, operating at 135 kfps, were placed perpendicular to the trajectory path of the projectile to monitor the impact angle of the cubical projectile against the target. A valid impact test with the cubical projectile was defined as one in which the deviation from the desired impact orientations did not exceed ± 5 degrees. Three distinct impact orientations were considered for cubical projectiles: (I) edge-on, (II) corner-on, and (III) face-on, as shown in Fig. 2(a). Figures 2(b,c) provide visual representations of the impact angle verification from both top and side views for the edge-on and corner-on impact orientations. Images captured by the side camera were used to extract impact and residual velocities for each test. To achieve the desired velocities and orientations, both spherical and cubical projectiles were positioned within 3D-printed sabots for launch.

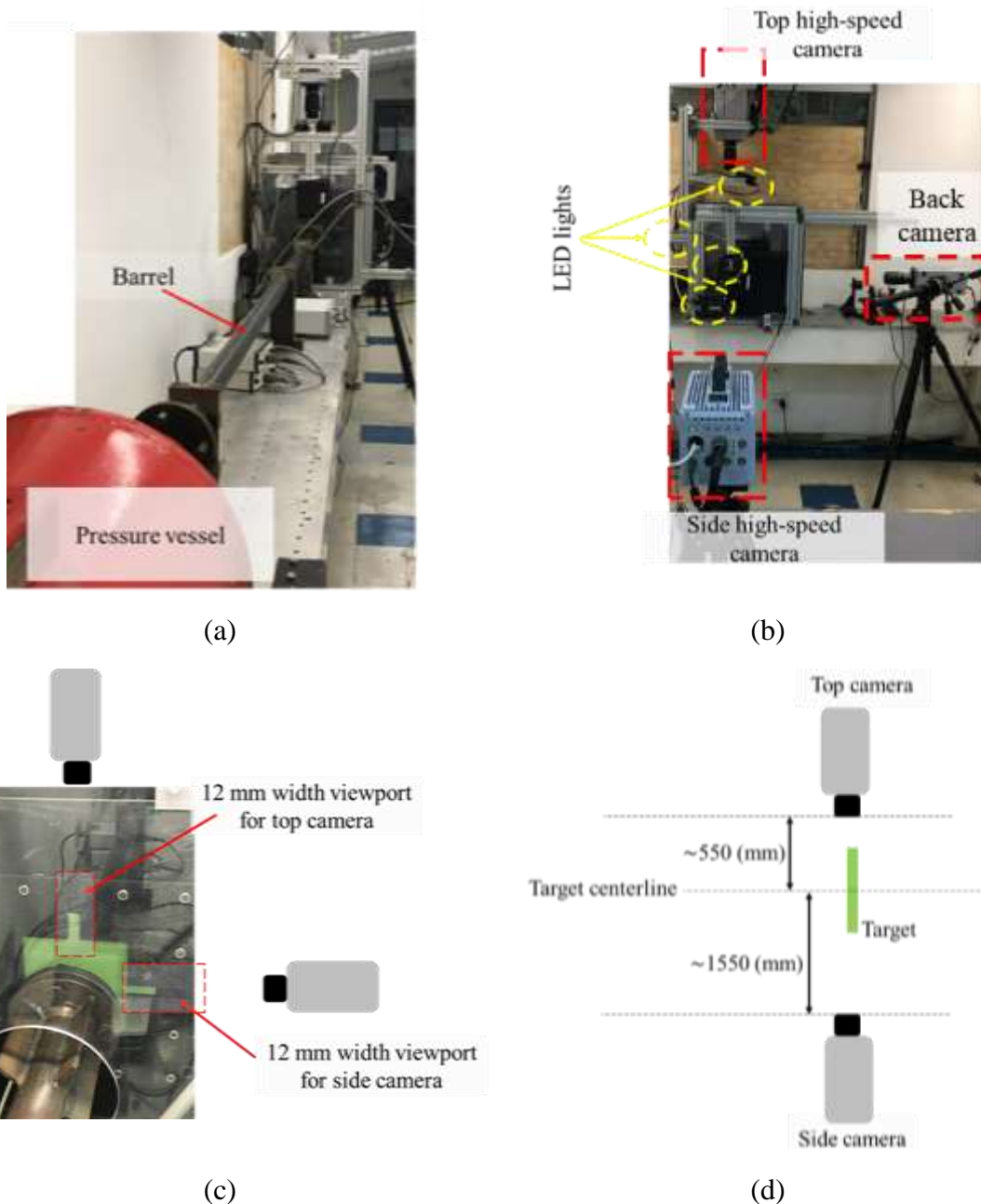
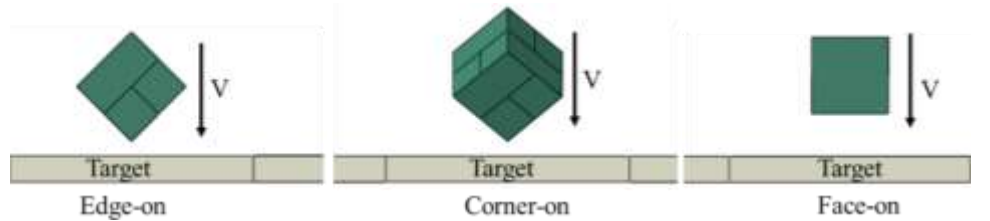


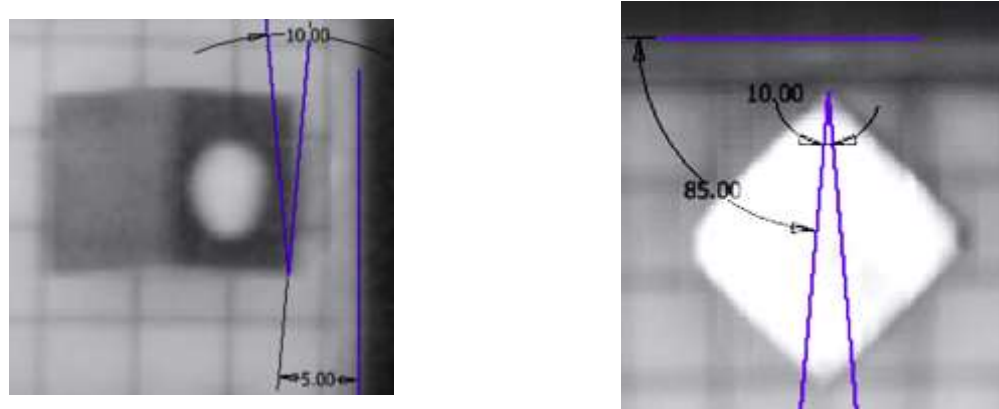
Fig. 1. Small debris impact test setup; (a) Gas gun overview, (b) High-speed cameras, and (c,d) Positions of cameras.

Square AA7475-T7351 aluminum plates ($200 \times 200 \text{ mm}^2$) with four distinct thicknesses [3.2 mm, 3.8 mm, 4.2 mm, and 4.66 mm] were fixed on the target holder at their four edges, excluding the small viewports regions (Fig. 1(c)). This configuration ensured a free impact area for the targets measuring $130 \times 130 \text{ mm}^2$. Two types of steel projectiles were chosen for this study: (I) a cubical

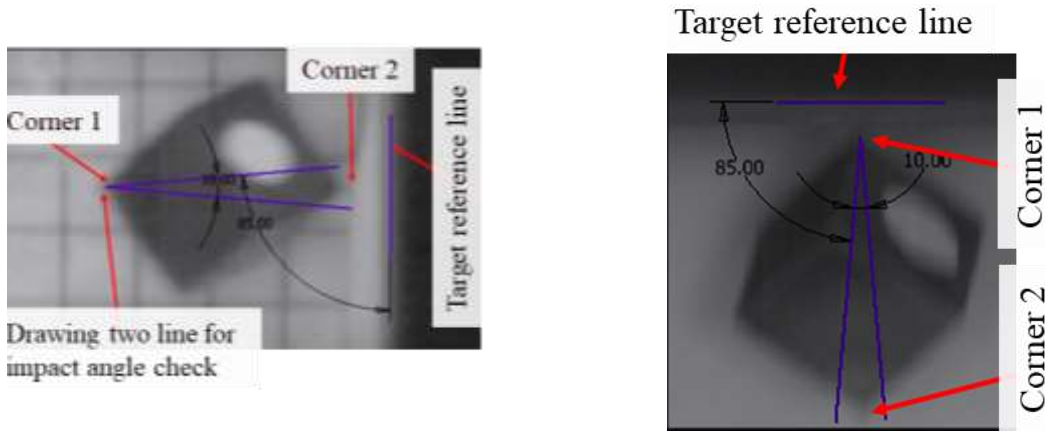
projectile with a mass of 7 grams and an edge length of 9.5 mm, and (II) a spherical projectile with an 11 mm diameter, possessing a mass approximately equivalent to that of the cubic projectile.



(a)



(b)



(c)

Fig. 2. Impact orientations of the cubical projectile; (a) Three different impact orientations of the cubical projectile, (b) Side and Top views impact angle check for an edge-on orientation, and (c) Side and top views impact angle check for a corner-on orientation.

Immediately following each valid impact test, the damaged aluminum plate was removed from the impact plate holder and positioned on the leakage test fixture, as shown in Fig 3. The fixture comprised two identical flat transparent plates, the upper and the lower, each featuring a 100 mm diameter hole at its center, along with a rubber gasket and a long transparent acrylic tube with a 100 mm outer diameter. To conduct the leakage test, the aluminum plate was firmly secured between the lower and upper plates using four M10 bolts. Subsequently, the tube was filled with water until the water level reached a height of 1.4 m (this pressure is assumed to represent the pressure of the fuel tank in this study). The impacted plate should withstand twenty minutes without any water droplet generation to pass successfully the leakage test criterion.

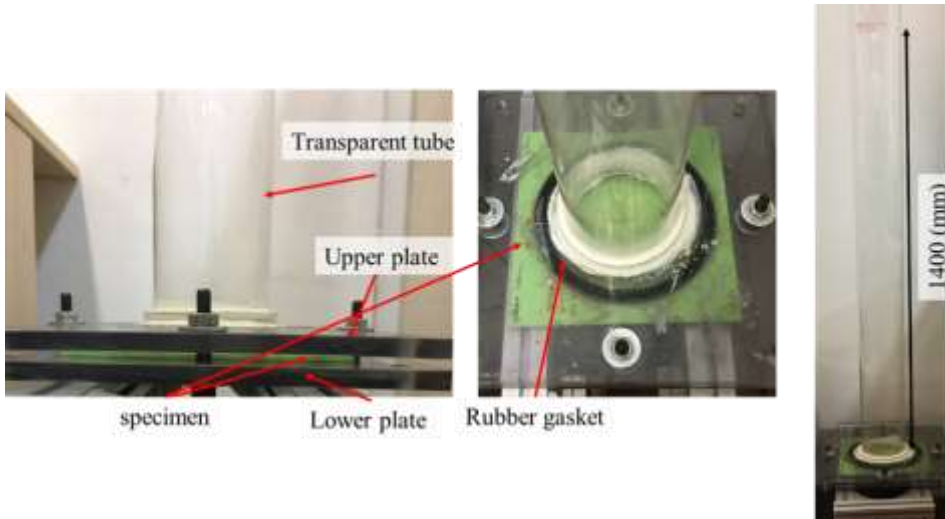


Fig. 3. Leakage test fixture.

2.2 Description of the Numerical Study

2.2.1 General Overview

The Abaqus\Explicit code was employed to simulate the impact of small debris on the aluminum plates, aiming to gain a more comprehensive understanding of their perforation mechanisms. The modeling approach adopted a 3D solid element (C3D8R) with reduced integration and hourglass control, to represent the projectiles and targets (aluminum plates).

The mesh size for each component in the finite element (FE) model was carefully chosen, taking into account the suggestions from the literature, precision requirements, and computational efficiency in terms of time. Within the $30 \times 30 \text{ mm}^2$ impact region of the aluminum targets, a fine

mesh size of $0.4 \times 0.4 \text{ mm}^2$ is applied, while a coarser mesh size of $1.5 \times 1.5 \text{ mm}^2$ is implemented outside the impact region, as illustrated in Fig 4(a). The global mesh size for the projectiles is established at 0.5 mm. To simulate the interaction between the part instances, the hard contact condition and tangential behavior were implemented. Specifically, a friction coefficient of 0.35 was assumed to govern the tangential behavior between the plate and the projectile. Clamped boundary conditions were enforced along the borders of the targets to replicate the actual boundary conditions observed in the experimental study, as depicted in Fig 4(b).

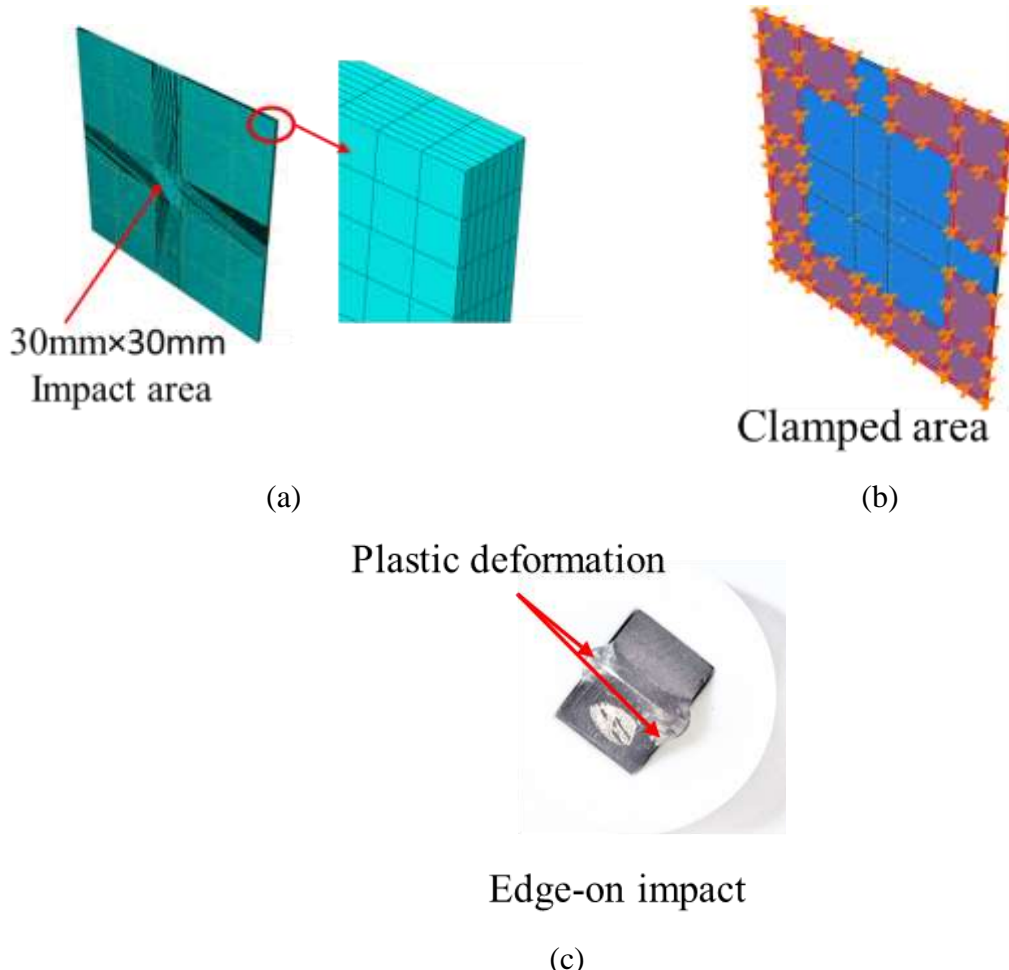


Fig. 4. A few details of numerical modeling; (a) FE presentation of an aluminum target, (b) Boundary condition of targets, (c) Plastic deformation of the cubical projectile with the edge-on impact orientation.

2.2.2 Material Models for Projectile and Aluminum Targets

2.2.2.1 Johnson-Cook Plasticity Model for Projectiles and Aluminum Targets

Plastic yielding has been taken into account for both the aluminum targets and steel projectiles. This consideration stems from the observation of substantial plastic deformation in the cubical projectiles during experimental tests, as illustrated in Fig. 4(c). However, a more sophisticated material model is employed in the FE model for the aluminum targets. The elastoplastic model with the phenomenological Johnson-Cook (JC) plasticity [22] was utilized for both the aluminum targets and projectiles. The JC plasticity model represents flow stress as a function of strain hardening, rate dependency, and temperature dependency as expressed by Eq. 1 [22]. In Eq.1 the effective stress, σ_0 , is expressed as a function of effective plastic strain, $\bar{\varepsilon}^{pl}$, nondimensional plastic strain rate, $(\frac{\dot{\varepsilon}^{pl}}{\dot{\varepsilon}_0})$, and a nondimensional temperature, $\hat{\theta}$ by using material parameters, A, B, n, C, and m [22].

$$\sigma_0 = (A + B(\bar{\varepsilon}^{pl})^n(1 + C \ln(\frac{\dot{\varepsilon}^{pl}}{\dot{\varepsilon}_0}))(1 - \hat{\theta}^m)) \quad (\text{Eq.1})$$

Table 1 lists the material properties of both the steel projectiles and the aluminum targets utilized in this study. The material properties for AA 7475-T7351 were sourced from a recent publication [21].

Table 1. Material properties for the projectiles and targets.

Elastic parameters		
	Aluminum	Steel
ρ (kg/m ³)	Density	2810
E (GPa)	Elastic modulus	71.35 [21]
ν (-)	Poisson's ratio	0.33
Plasticity model (Johnson-Cook) parameters		
$\sigma_0 = (A + B(\bar{\varepsilon}^{pl})^n(1 + C \ln(\frac{\dot{\varepsilon}^{pl}}{\dot{\varepsilon}_0}))(1 - \hat{\theta}^m))$ [22]		

		Aluminum	Steel [23]
A (MPa)	Static Yield stress	474.82 [21]	363
B (MPa)	Strain hardening modulus	397.78 [21]	792.71
n	Strain hardening exponent	0.5948 [21]	0.5756
C	Strain rate coefficient	0.0064 [21]	0.0054
m	Thermal softening exponent	1.0728 [21]	1.6456
T _{room} (°K)	Reference temperature	298.15 [21]	298.15
T _{melt} (°K)	Melting temperature	908.15 [21]	1798.0
C _p (J/kg °K)	Specific heat	875.00 [14]	510.00

$\dot{\varepsilon}_0$ is reference strain rate value, 0.0001 s⁻¹.

2.2.2.2 Johnson-Cook Damage Model for AA 7475-T7351 Aluminum

In the Johnson-Cook damage model, failure will occur when the damage parameter, D in (Eq.2) reaches one (The initial value of the damage parameter associated with no damage state is equal to zero).

$$D = \sum \frac{\Delta \bar{\varepsilon}^{pl}}{\bar{\varepsilon}_f^{pl}} \quad (\text{Eq.2})$$

where $\Delta \bar{\varepsilon}^{pl}$ is incremental equivalent plastic strain and $\bar{\varepsilon}_f^{pl}$ is the failure strain. The failure strain can be expressed by Eq. 3 which calculates the failure strain as a function of stress triaxiality, η , nondimensional strain rate, $(\frac{\dot{\varepsilon}^{pl}}{\dot{\varepsilon}_0})$, nondimensional temperature, $\hat{\theta}$ and five damage parameters, $d_1 - d_5$.

$$\bar{\varepsilon}_f^{pl} = (d_1 + d_2 \exp(d_3 \eta) (1 + d_4 \ln(\frac{\dot{\varepsilon}^{pl}}{\dot{\varepsilon}_0})) (1 + d_5 \hat{\theta})) \quad (\text{Eq.3})$$

The damage parameters ($d_1 - d_5$) constitute a pivotal aspect of the numerical model, and their values are obtained through experimental extraction in this study. However, the procedure is concisely explained below to minimize any deviation from the primary objectives of this study.

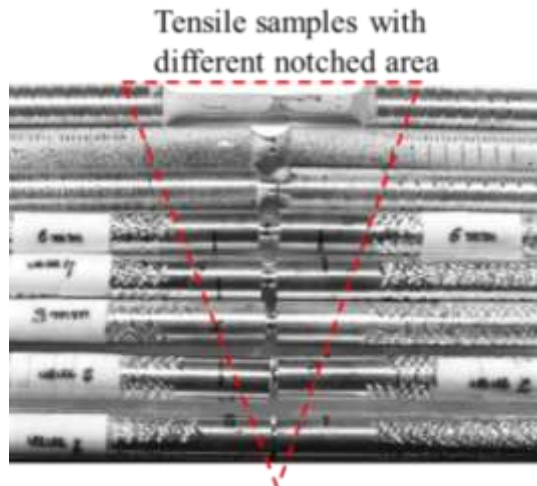
Several tests were conducted under different stress states and strain rate conditions to calibrate the five JC damage model parameters. Quasi-static tensile tests on both smooth and notched specimens were carried out at room temperature (25°C) and elevated temperature (250)°C using the Zwick Roll/Z50 universal testing machine, featuring a maximum load capacity of 50 kN. Additionally, a 3D DIC strain measurement system was employed to quantify specimen deformation. High-strain rate tensile experiments were conducted using the split Hopkinson tensile bar (SHTB) apparatus. Comprehensive details regarding the high strain rate experimental procedure, are thoroughly addressed in Ref [24]. Figures 5(a-c) depict the fracture of smooth and notched tensile specimens under quasi-static, elevated temperatures, and high strain rates, respectively. Figure 5(d) displays the Digital Image Correlation (DIC) strain contour of the 6 mm notched tensile specimen.

Considering room temperature (25°C) and the reference strain rate (10e-4 s⁻¹), the thermal and strain rate dependency terms in Eq. 3 will be canceled out, simplifying Eq. 3 to $\bar{\varepsilon}_f^{pl} = (d_1 + d_2 \exp(d_3 \eta))$. Utilizing experimental results from quasi-static tensile tests as depicted in Fig. 6(a), the equivalent fracture strains of the notched tensile specimens are plotted in Fig. 6(b) as a function of stress triaxiality (η), d_1 , d_2 , and d_3 . Damage parameters (d_1-d_3) are determined through regression analysis using the curve fitting method, as illustrated in Fig. 6(b).

To evaluate the damage parameter, d_4 related to the rate dependency of material, the fracture strain data measured from SHTB tests (from 10e-4 to 3000 s⁻¹) were utilized. Under ambient temperature and different loading rates, Eq. 3 is simplified to $\bar{\varepsilon}_f^{pl}/(d_1 + d_2 \exp(d_3 \eta)) = 1 + d_4 \ln(\dot{\bar{\varepsilon}}_f^{pl}/\dot{\varepsilon}_0)$. The rate-dependent fracture parameter d_4 can be evaluated by calculating the slope of $\bar{\varepsilon}_f^{pl}/(d_1 + d_2 \exp(d_3 \eta))$ vs $\ln(\dot{\bar{\varepsilon}}_f^{pl}/\dot{\varepsilon}_0)$ as depicted in Fig. 6(c).

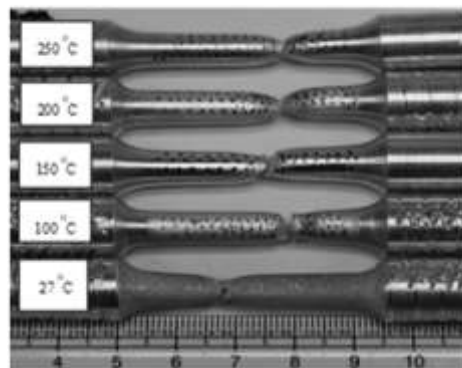
The fracture strain data of tensile experiments conducted at reference strain rates and different temperatures will be used to calibrate the temperature-dependent fracture parameter (d_5)

of AA7475-T7351. Fracture parameter d_5 is calculated by finding the slope of the curve $\bar{\varepsilon}_f^{pl}/(d_1 + d_2 \exp(d_3 \eta))$ vs $\hat{\theta}$ as shown in Fig. 6(d).



(a)

Fracture of tensile samples at different thermal conditions



(b)

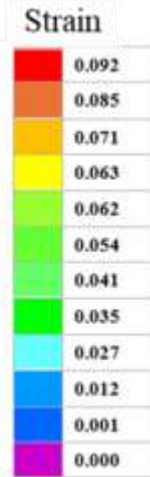
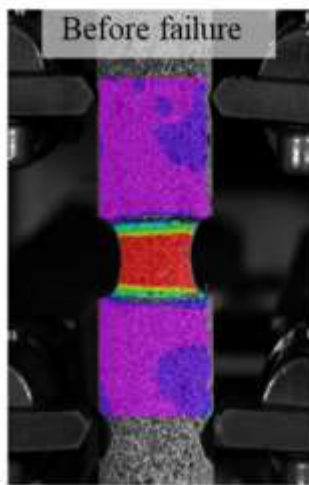


Strain rate: $\sim 1000 \text{ s}^{-1}$



Strain rate: $\sim 2100 \text{ s}^{-1}$

(c)



(d)

Fig. 5. Several aspects of experimental evaluation of JC damage parameters; (a) Fracture of tensile samples having different notched areas under quasi-static test, (b) Fracture at elevated temperatures, (c) Fracture of SHTB samples, and (d) Example of 3D DIC strain measurement.

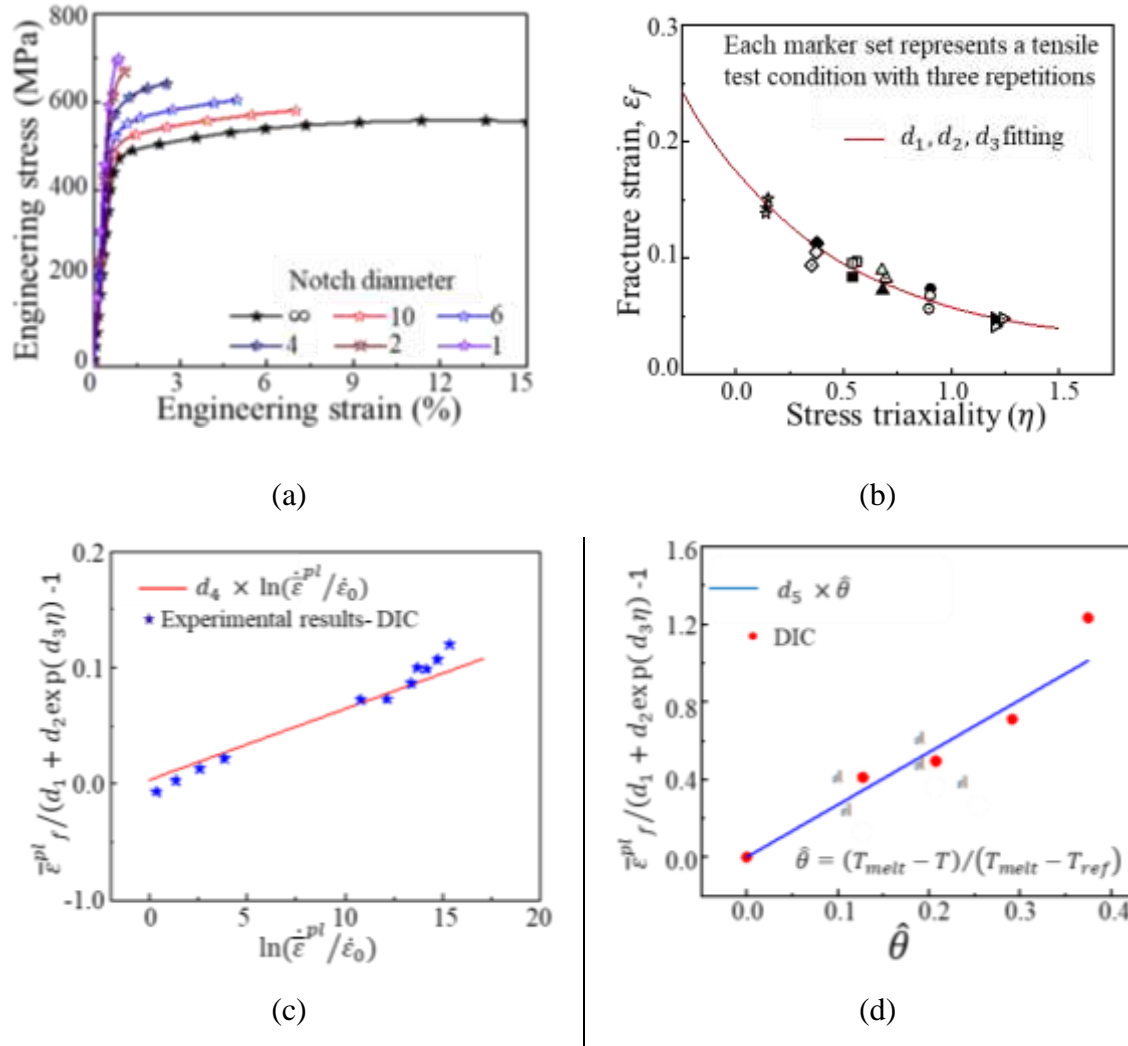


Fig. 6. Evaluation of JC damage model parameters; (a) Quasi-static tensile test results for samples with different notched areas, (b) Evaluation of triaxiality parameters (d_1, d_2, d_3), (c) Evaluation of strain rate sensitive fracture strain parameter (d_4) and (d) Evaluation of temperature-sensitive fracture strain parameter d_5 .

All JC damage parameters (d_1 - d_5) for AA 7475-T7351 targets are listed in Table 2. These parameters underwent fine-tuning through a series of trial-and-error impact simulations in the subsequent section. The calibration process involved conducting experimental impact tests using both spherical and cubical projectiles on the thinnest aluminum plate investigated in this study. Consequently, the calibrated parameters were selected to establish an exceptional quantitative and qualitative correlation between the finite element (FE) simulation results and the corresponding experimental outcomes. The calibrated values are presented in Table 2.

Table 2. JC damage parameters for AA 7475-T7351 aluminum.

$\bar{\varepsilon}^{pl}_f = (d_1 + d_2 \exp(d_3 \eta))(1 + d_4 \ln(\dot{\varepsilon}^{pl}/\dot{\varepsilon}_0))(1 + d_5 \hat{\theta})$				
Experimentally evaluated values				
d_1	d_2	d_3	d_4	d_5
0.131±0.03	0.146±0.022	0.146±0.031	0.0053±0.003	2.1
Calibrated values based on experimental ballistic test results*				
d_1	d_2	d_3	d_4	d_5
0.115	0.123	1.150	0.007	2.1

* Calibrated value using impact tests on the aluminum plate having 3.2 mm thickness.

η is stress triaxiality.

$\dot{\varepsilon}_0$ is reference strain rate value, 0.0001s^{-1} .

3. Results and discussion

In this section, first, the results of the high-velocity impact on the aluminum targets were presented. The experimental results were employed for the calibration and validation of the numerical model. This process aimed to enable the numerical model to predict the leakage velocity limits for aluminum plates with different thicknesses. Subsequently, the numerical model was applied to

explore the influence of pitch and yaw deviations from ideal corner-on, face-on, and edge-on orientations on the ballistic and leakage limit velocities of aluminum targets.

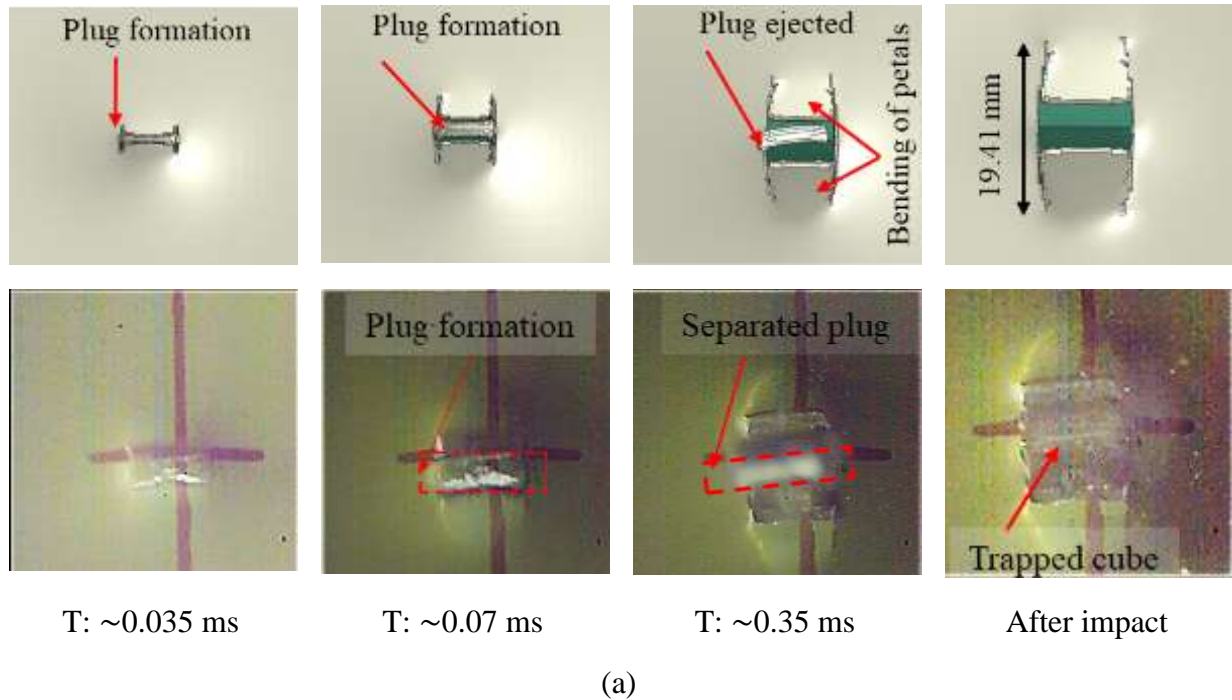
3.1 Experimental and Numerical Impact Test Results

Figures 7 and 8 illustrate the penetration process of the 3.2 mm thick plates hit by the cubical projectile with edge-on impact orientation and spherical projectile at maximum striking velocities. In these cases, the projectiles did not pass through the plates. Ductile hole enlargement (petals formation), adiabatic shearing (plugging), and global bending (dishing) [25] were observed for both impact scenarios, as shown in Figs. 7 and 8. Since the kinetic energies were not sufficient, the projectiles only perforated the targets. The plug was generated (ejected or not ejected) in all impact tests conducted with the spherical projectile.

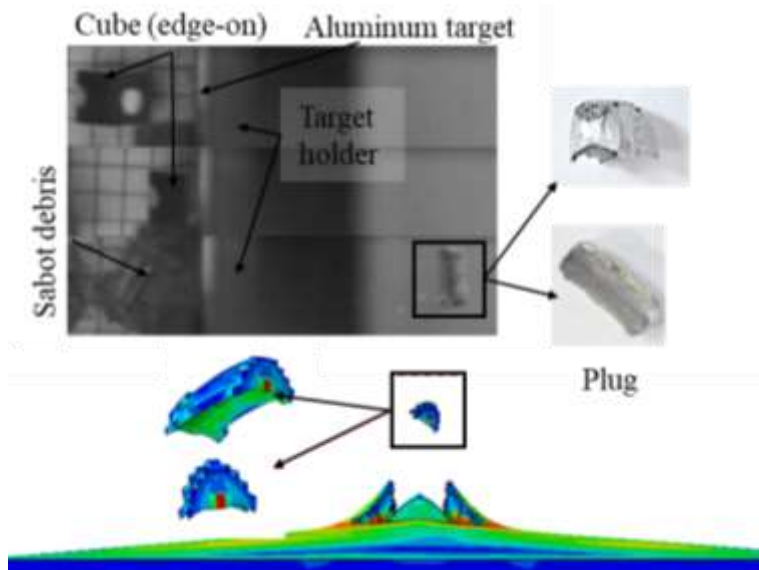
In the case of the edge-on cubical projectile, the plug was generated and ejected in only a few of the impact tests. After the plug was ejected, two petals were initiated and bent outwardly in the case of the edge-on impact test. It is worth noting that due to the insufficient kinetic energy of the cube, the petals did not detach from the target.

For the spherical projectile, more than nine petals were observed on the target. In this case, even when the sphere had enough kinetic energy, the petals were not removed from the targets.

Based on the observations in this study concerning edge-on impacts, it was noted that plug formation/ejection depends on the velocity of the projectile and impact orientation, with approximately zero deviation. While plug generation was observed in the numerical simulation, it was found that, in addition to an accurate impact angle and sufficient velocity, it was highly dependent on mesh density. Figure 7(b) provides a visual representation of the ejected plugs in both the experimental test and numerical simulation. In Ref. [2] plug was not generated for the edge-on impact on the AA2024-T351 aluminum plate. Plug ejection may become somewhat important since in empirical residual velocity equations, like Recht-Ipson [19], the multiplier is a function of the masses of the projectile and ejected plug.

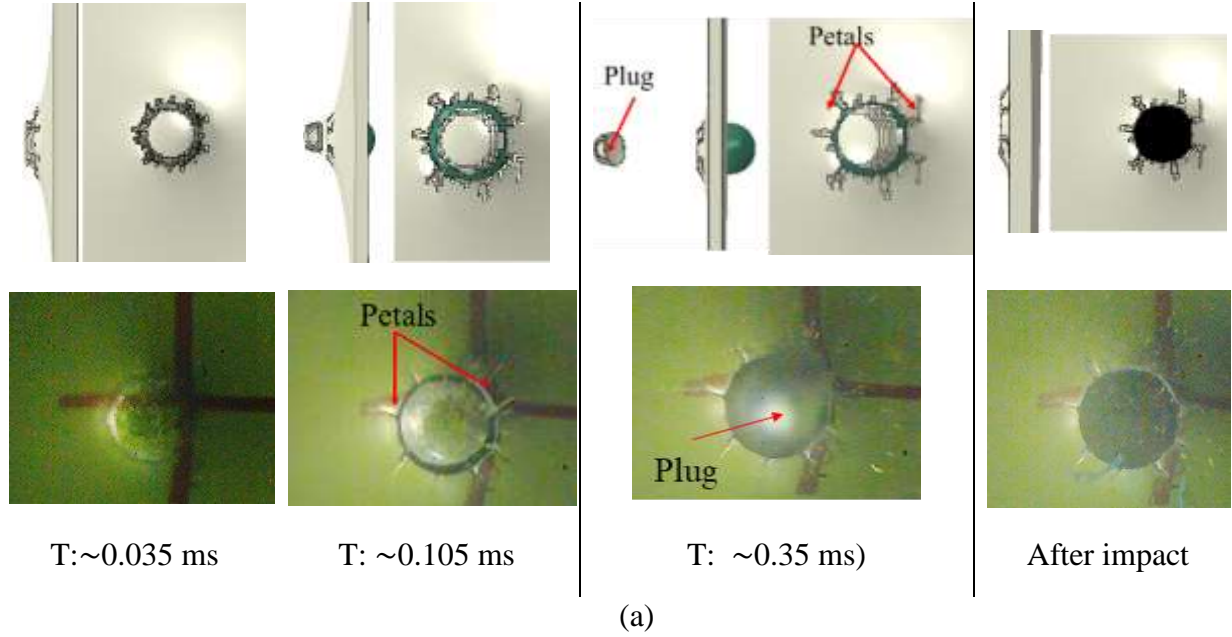


(a)

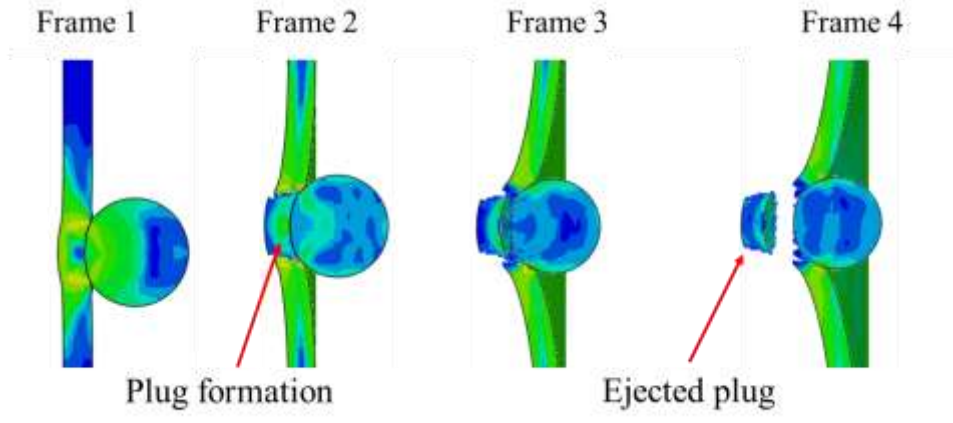


(b)

Fig. 7. The failure mechanism of a 3.2 mm thick aluminum target impacted by the cubical projectile having edge-on orientation; (a) Sequential snapshots of partial penetration and (b) Plug ejection for experimental and numerical simulation.



(a)



(b)

Fig. 8. The failure mechanism of a 3.2 mm thick aluminum target impacted by a spherical projectile; (a) Sequential snapshots of partial penetration and (b) Plug ejection process numerical simulation.

Figure 9 illustrates the results of the experimental test and numerical simulation of impact on the 3.2 mm thick target, striking velocity of 235 m/s. Since the projectile had sufficient kinetic energy, it completely went through the target. The petals formed and underwent bending and finally sheared off from the plate. However, the plug was not generated in this case. This experimental test was used to calibrate the JC damage parameter in the FE model. In addition to

the good agreement between residual velocities, i.e. experimental residual velocity equals 81 m/s and numerical one equal to 85 m/s, there is a reasonable agreement between the dimensions of the elliptical hole on the plates in experimental and numerical results, as shown in Fig. 9.

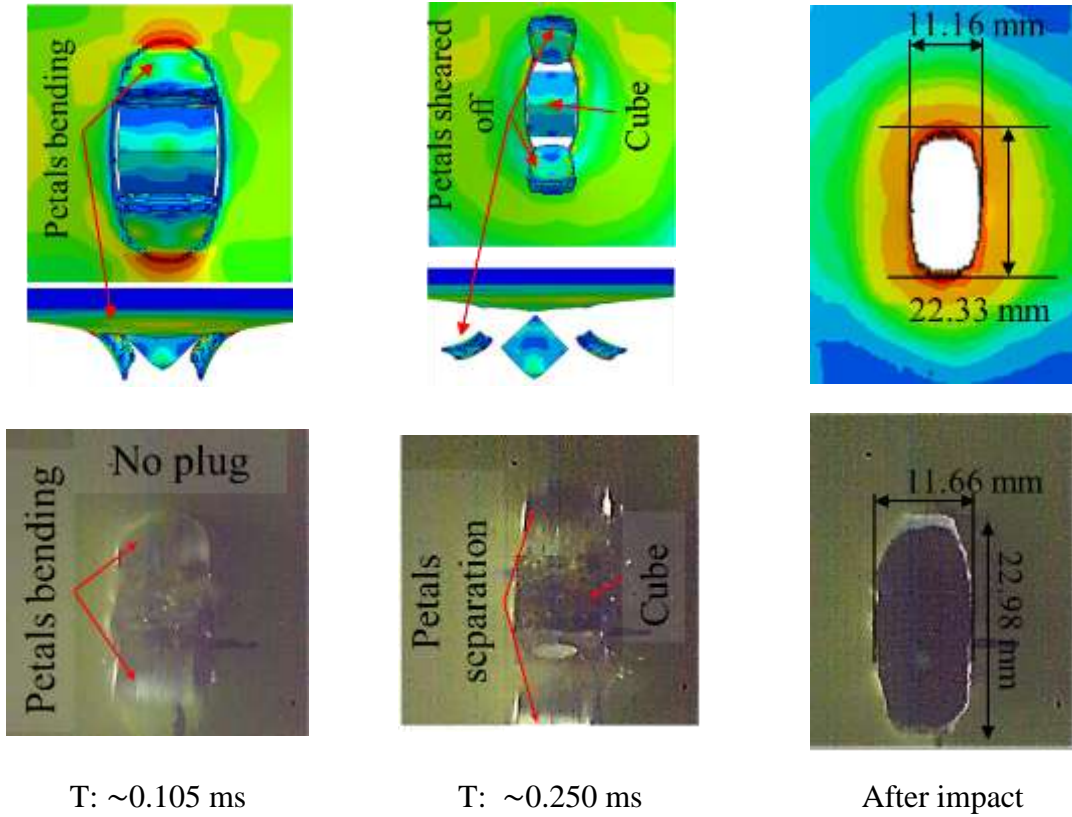
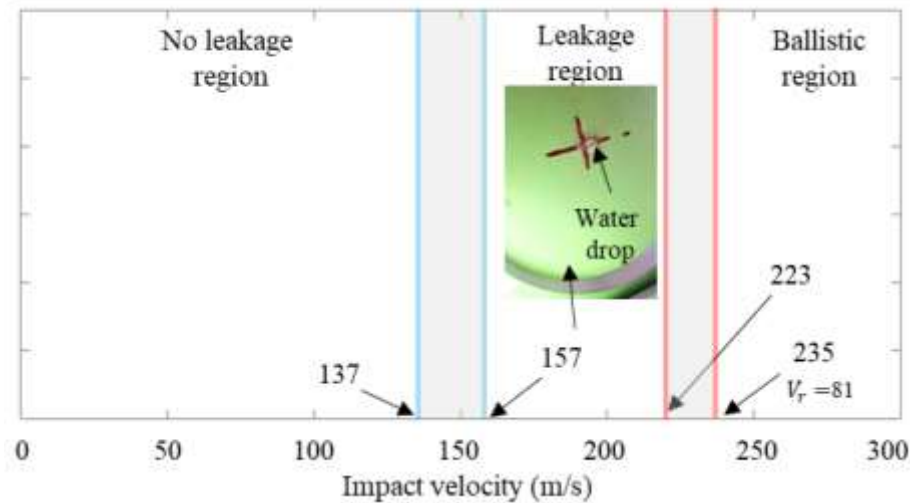


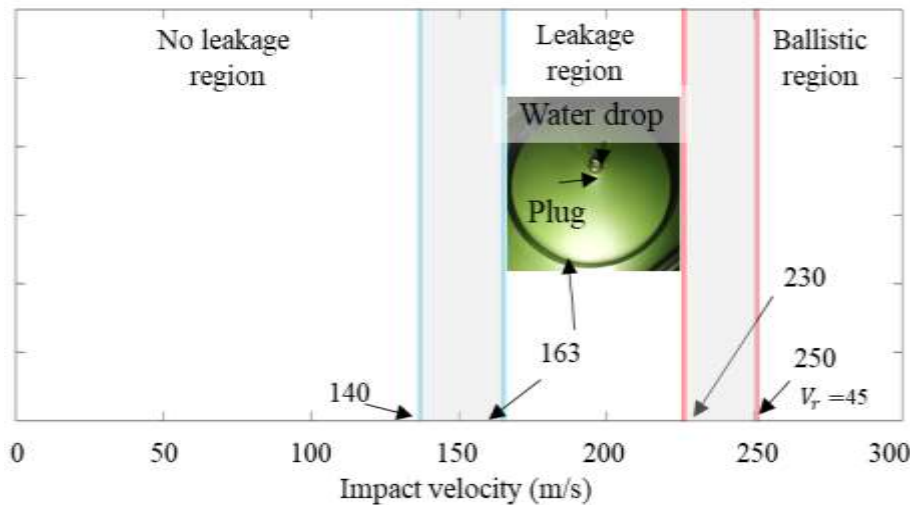
Fig 9. Sequential snapshots of full penetration of cubic projectile in 3.2 mm thick aluminum plate, impact velocity 235 m/s.

Figure 10 presents the results of impact tests and subsequent post-impact leakage tests conducted on 3.2 mm thick targets, impacted by both spherical and edge-on cubical projectiles. Varying projectile velocities produced graphs with three distinct regions, as follows.

- (I) No leakage region: This region represents cases where the impacted target successfully passed the leakage test.
- (II) Leakage region: In this region, the impacted target failed to pass the leakage test.
- (III) Ballistic region: This region indicates scenarios where the projectile fully penetrated through the target.



(a)



(b)

Fig 10. Impact test results on the 3.2 mm thick aluminum plate; (a) Cubical projectile with edge-on orientation and (b) Spherical projectile (V_r is residual velocity).

Table 3 provides a summary of the leakage test details for impact tests conducted on aluminum plates with varying thicknesses. Notably, for plates impacted by the cubical projectile, there is a strong agreement between the leakage start velocities observed in the experimental tests and those simulated in the numerical finite element analysis. However, the experimental leakage limit velocities, the average of the maximum striking velocity without leakage, and the minimum

striking velocity with leakage, are remarkably lower than their numerical counterparts. This discrepancy can be attributed to the relatively larger velocity increment (approximately 20 m/s) utilized in the experimental impact tests, as compared to the 5 m/s) velocity increment selected in the FE simulations.

Table 3. Summary of leakage test results on the aluminum targets after impact test.

Projectile	Method	Thickness (mm)							
		3.2		3.8		4.2		4.6	
		Velocity ranges (m/s)							
Spherical	EXP	NL ^a	140	151	207 ^c	207	232	238	-
		SL ^b	163		228		244		-
	FE	NL	145	147	185	187	205	207	215
		SL	150		190		210		220
Cubical	EXP	NL	137	147	172	183	219	220	227 ^c
		SL	157		195		222		>227
	FE	NL	155	157	190	192	215	217	230
		SL	160		195		220		235

^a NL: No leakage.

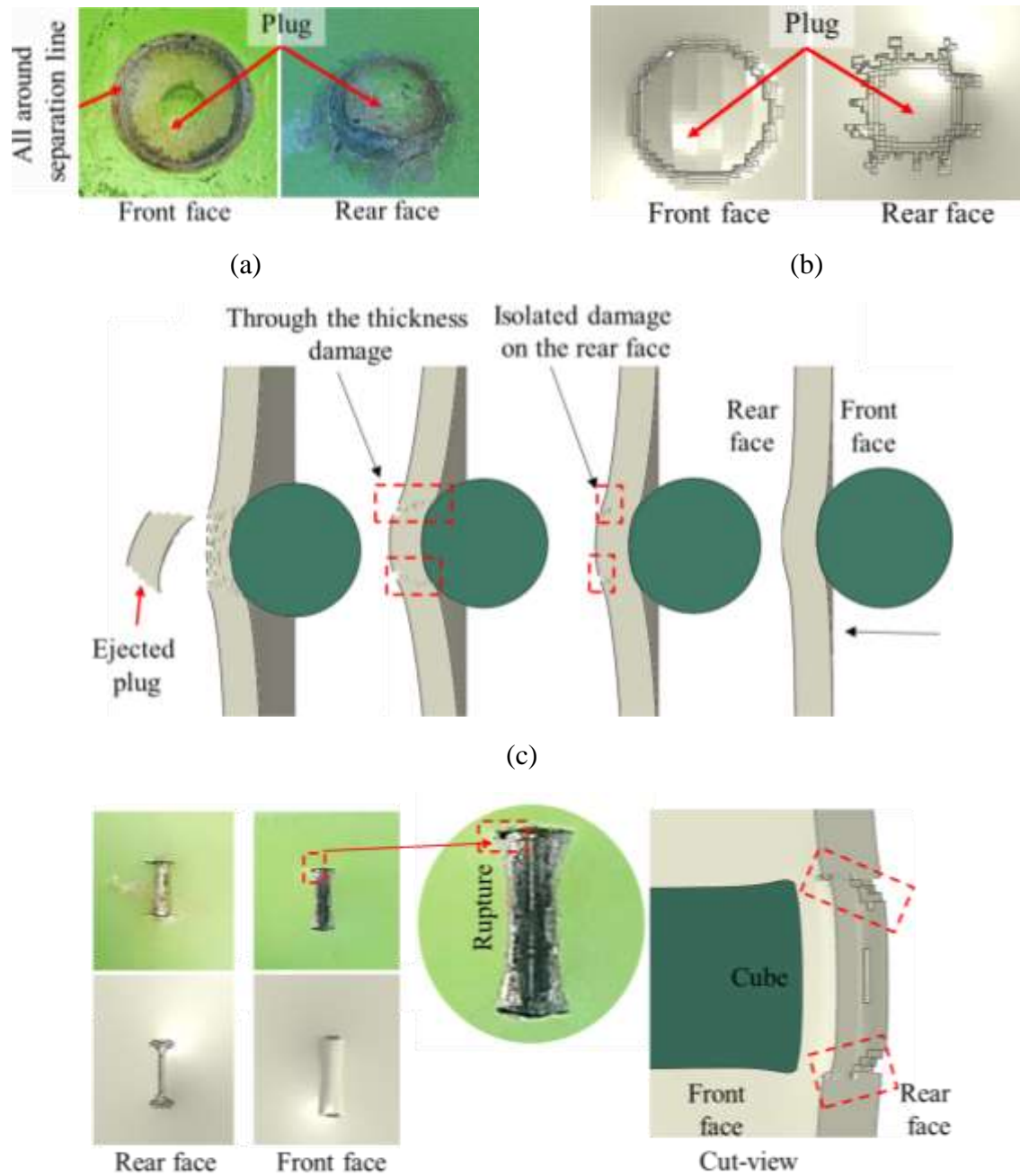
^b SL: Start to leak.

^c Wetted only (no droplet).

In all experimental impact tests involving spherical projectiles, a significant disparity was observed between the initiation of leaking and the velocity at which the plug was ejected. In fact, in between the leaking initiation and plug ejection, the plug has been sheared off from the target (the separation line is highlighted in Fig. 11(a)). However, due to elastic-plastic deformation, high pressure, and friction between the plug and hole, the plug was trapped in the hole and sealed again. Therefore, the targets could pass the water leakage test criterion in some cases. However, it is important to note that the finite element (FE) model could not predict the sealing process described

above. Consequently, the leakage initiation velocities predicted by the FE model were significantly lower than those observed in the experimental tests for spherical projectiles.

To assess leakage in the numerical simulations, such as for the plate impacted by the edge-on cubical projectile, cross-sectional cuts were employed at critical regions. These cuts were used to verify that damages on both the rear and front faces of the plate were connected through the plate thickness, as depicted in Fig. 11(d).



(d)

Fig. 11. Deformation of the plate impacted by a spherical projectile that failed the leakage test; (a) Experimental results, (b,c) Numerical results, and (d) An example of a plate impacted by the cubical projectile that failed to pass the leakage test.

The finite element (FE) model is employed to determine the leakage limit velocity of AA 7475-T7351 targets with varying thicknesses when subjected to impacts by cubical projectiles. Figure 12 illustrates the leakage limit velocities of targets impacted by cubical projectiles in face-on and corner-on orientations. With increments in target thickness from 3.2 to 4.66 mm, the leakage limit velocity exhibited a monotonically increasing trend for both corner-on and face-on orientations. The leakage limit velocity of the aluminum plate exhibited an increase of 85 m/s when the plate thickness rose from 3.2 to 4.66 mm in the case of a corner-on impact orientation. In contrast, for the face-on orientation, a more modest increment of 55 m/s was observed.

The ballistic limit velocities for aluminum targets under corner-on impact tests are not provided here, however, initial numerical simulations suggest that similar to the observations in edge-on impact orientation tests (depicted in Fig. 10), a substantial difference between the leakage limit and ballistic limit velocities is distinctly noticeable for corner-on impact orientation. Indeed, after the initial localized failures causing leakage, the plates underwent a sequence of destructive mechanisms, encompassing the plugging and bending of petals. These mechanisms played a crucial role in generating a noteworthy disparity between the leakage limit and ballistic limit velocities observed in both edge-on and corner-on impact orientations. For a detailed exploration of the damage mechanism in the context of edge-on impact orientation, please refer to the description provided here and in Ref [2]. Additionally, Ref [2] addresses the damage mechanism for corner-on impact on AA2024-T351 aluminum plates.

In contrast to corner-on impact orientation, there are insignificant differences between leakage limit and ballistic limit velocities for face-on impact orientation. Therefore, for the face-on impact scenario, the failure mechanisms leading to both leakage and complete penetration are ascribed to the same as plugging failure mode.

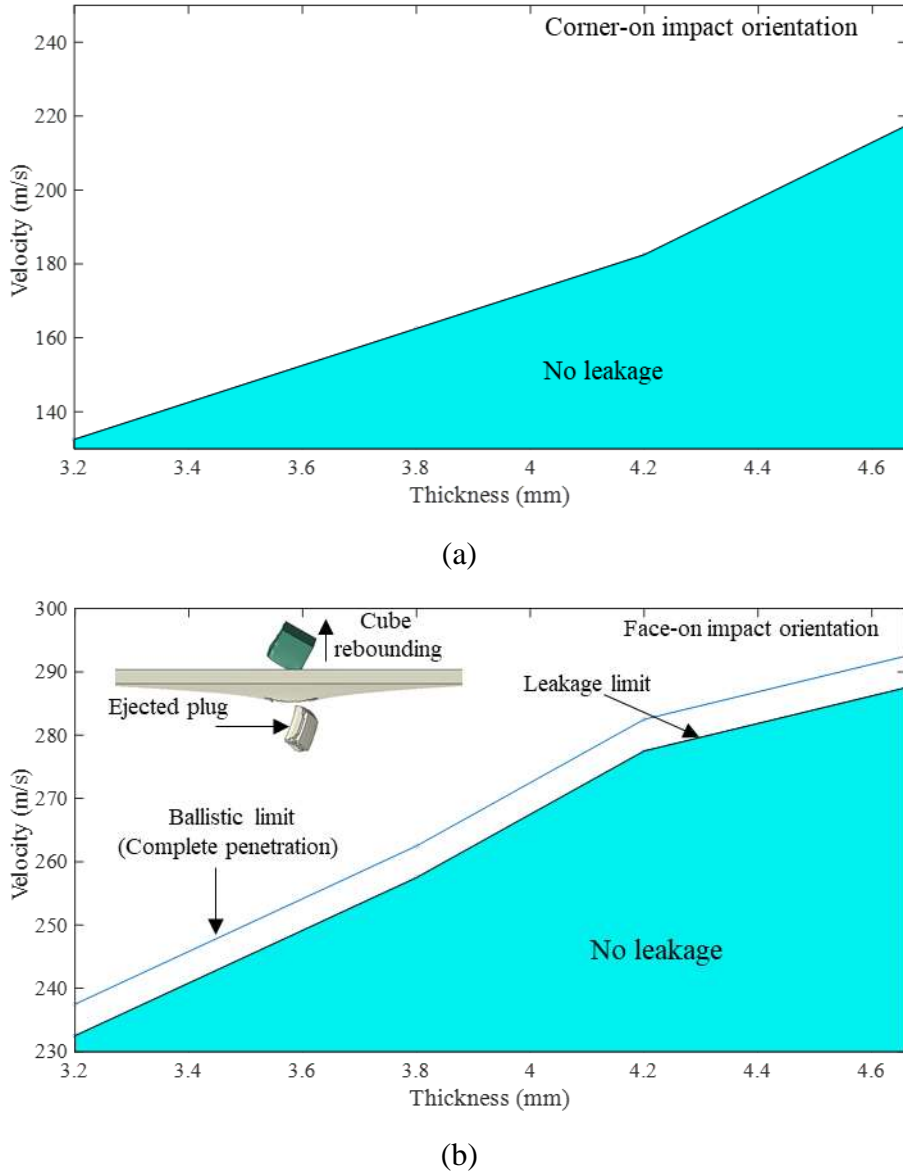


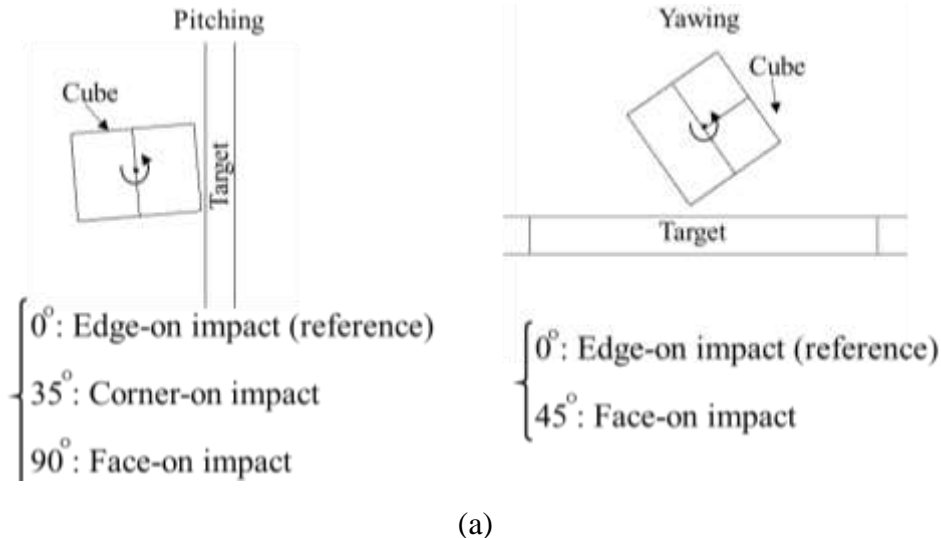
Fig. 12. Leakage limit velocity versus thickness of targets; (a) Corner-on impact orientation, (b) Face-on impact orientation.

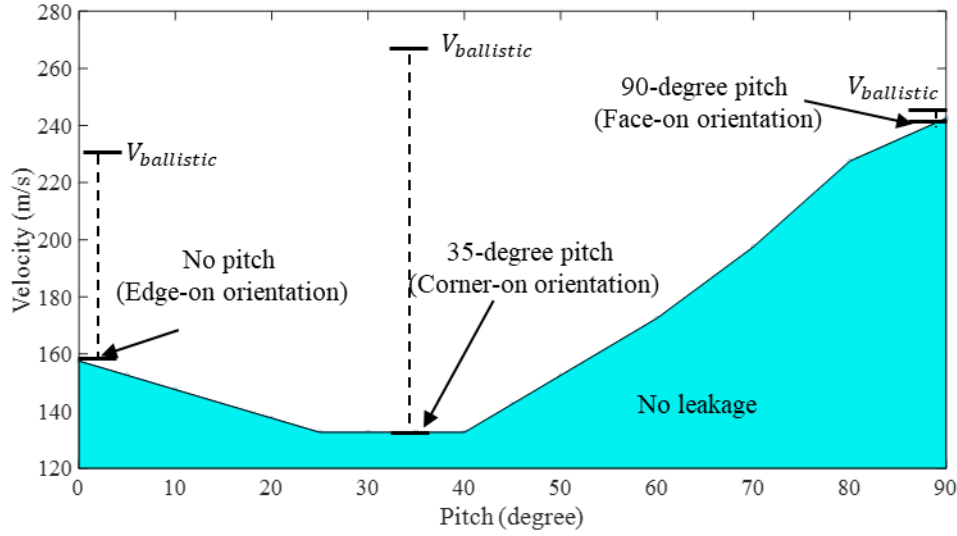
3.2 Effect of Pitch and Yaw Rotations on the Impact Resistance of Aluminum Plates

The results mentioned earlier were achieved while ensuring that the deviations of impact angle orientations were limited to below 5 degrees in two perpendicular view planes for experimental tests, and in the case of numerical simulations, ideal impact orientations (zero deviations) were considered. In this section the finite element (FE) model was employed to explore the effects of yaw and pitch rotations from the ideal edge-on orientation on the ballistic and leakage limits of a

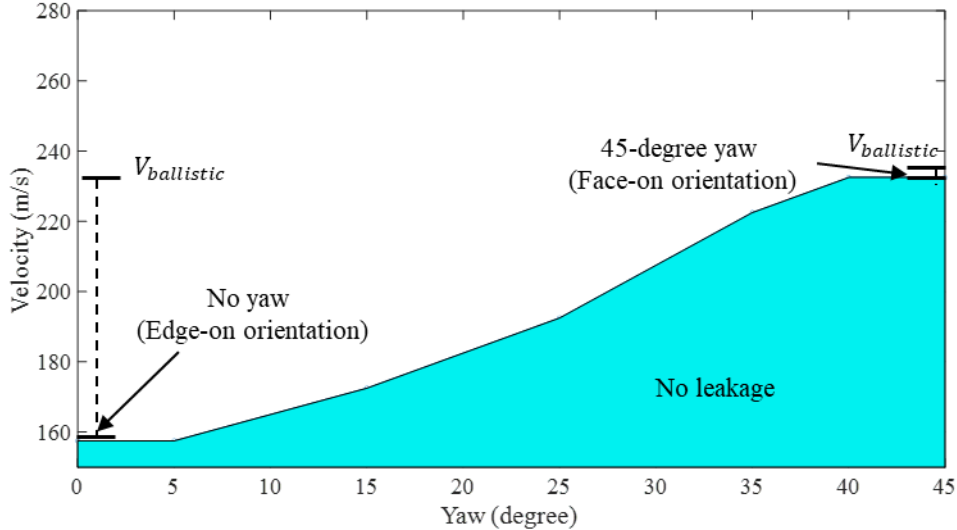
3.2 mm thick aluminum plate. The yaw and pitch rotations for the cubical projectile with an edge-on orientation are illustrated in Figure 13(a). It is worth noting that the edge-on orientation is used as a reference, as a 35-degree pitch and 45-degree yaw (or a 90-degree pitch) will result in the cube having corner-on and face-on orientations, respectively.

Figures 13(b,c) depict that the leakage limit velocity is directly related to the initial contact area between the projectile nose and the target surface. As the pitch rotation increases from an edge-on orientation to a corner-on orientation (35-degree pitch), the contact area between the cube and the target continuously decreases from an edge line to a sharp corner point. Consequently, the leakage limit velocity exhibits a monotonic decrease as a consequence of this rotation. As the rotation continues, one face of the cube progressively comes into greater contact with the target. When there is a 90-degree pitch rotation, the entire face of the cube impacts the target. Under these conditions, the leakage limit velocity reaches its maximum value, as depicted in Figure 13(b). In Figure 13(c) a similar trend can be observed for yaw rotation, ranging from zero degrees (edge-on orientation) to 45 degrees yaw (face-on orientation).





(b)



(c)

Fig. 13. Effect of yaw and pitch deviations from the edge-on impact orientation; (a) Yaw and pitch definitions, (b) Pitch deviation, and (c) Yaw deviation.

Figures 14 and 15 illustrate the deformation and damage on the aluminum targets when subjected to a constant striking velocity with varying pitch and yaw angles from an edge-on reference orientation. Figures 14(d) and 15(c) reveal that when projectiles with impact angles close to face-on orientation (blunt noses) impact the targets, their kinetic energy is uniformly dissipated

over a wide area on the targets, resulting in a global bending deformation mode. Consequently, no significant failure or damage occurred on the rear and front faces of the target.

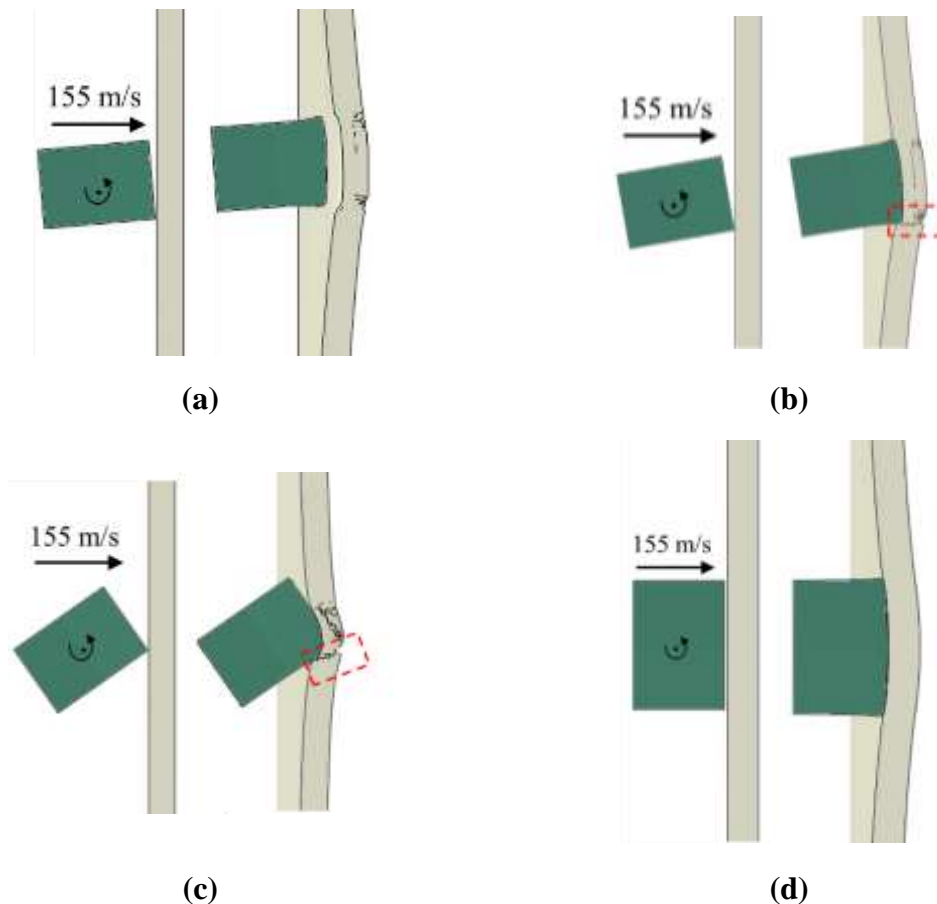


Fig. 14. Effect of pitch rotation from the edge-on orientation on the possibility of liquid leakage; (a) 5-degree pitch, (b) 10-degree pitch, (c) 35-degree pitch (corner-on orientation), and (d) 90-degree pitch (face-on orientation).

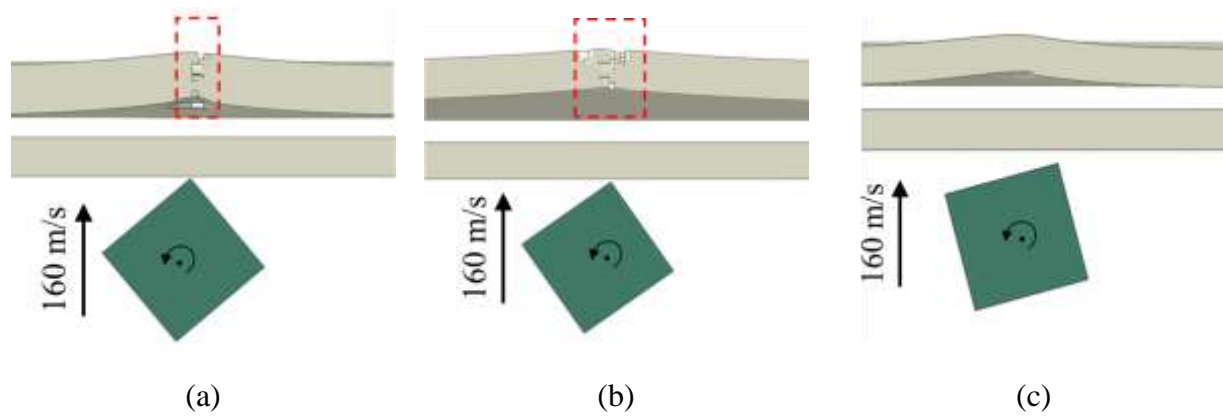


Fig. 15. Effect of yaw rotation from the edge-on impact orientation on the possibility of liquid leakage; (a) 5-degree yaw, (b) 10-degree yaw, and (c) 35-degree yaw.

Results presented in Fig. 13 indicate that projectiles with sharper noses (smaller contact area) led to lower leakage limit velocities (projectile's nose sharpness order: corner-on orientation > edge-on orientation > face-on orientation). The influence of projectile nose sharpness on the leakage limit velocity does not align with the effects of projectile nose sharpness on the ballistic limit velocities. For example, in Ref. [2], which studied the high-velocity impact performance of AA2024-T351 plates, it was reported that edge-on impact resulted in the lowest ballistic limit, whereas corner-on impact led to the highest ballistic limit velocity. It is worth noting that this observation is consistent with the numerical results obtained for AA 7475-T7351 targets in the current study for ballistic limit velocities (ballistic limit velocities: corner-on > face-on > edge-on).

4. Conclusions

AA 7475-T7351 aluminum finds extensive use in various aircraft components, including wing spars, stingers, fuel tanks, and the fuselage. This study focuses on examining high-velocity impacts on aluminum plates to evaluate the safety of aircraft when subjected to high-velocity debris such as uncontained engine failure debris striking the fuel tanks. In this work, instead of relying on conventional criteria such as ballistic limit velocity criteria with common definitions of complete penetration (e.g., navy definition, army definition, and protection definition), we employed a leakage limit velocity criterion to assess the high-velocity impact performance of AA 7475-T7351 aluminum plates.

This study followed an experimental-numerical approach. Following each impact on the target during experimental trials, a leakage test was performed on the damaged plate to detect any potential liquid leaks. Given the demanding and costly nature of experimental tests, a finite element (FE) model of the targets was developed and calibrated. The validation of the numerical model was assessed through various impact scenarios on the targets. In general, the developed

numerical model was capable of predicting the leakage limit velocity compared to the experimental tests.

The study delved into the influence of cubical projectile orientation, particularly its nose sharpness, on the high-velocity impact resistance of the targets. This was achieved by launching the cubic projectile in precise edge-on, corner-on, and face-on impact orientations. An evident correlation emerged between the sharpness of the projectile's nose and the leakage velocity limit of the aluminum targets. Notably, the sharper the contact area of the projectile, the lower the leakage velocity limit. However, it is worth highlighting that this relationship did not hold for ballistic limits, as the corner-on impact orientation (characterized by the sharpest projectile nose) exhibited the highest ballistic limit, whereas the edge-on impact orientation had the lowest ballistic limit velocity.

The numerical investigation examined the effects of pitch and yaw rotations starting from the edge-on impact orientation on the high-velocity impact resistance of the aluminum plates. Any rotations that alter the extent of the contact area, in this case transitioning from an edge line to a corner point or the face of the cube, would inevitably affect both the leakage and ballistic limits of the target. The study found that small rotations, specifically those less than 5 degrees, had negligible effects on both the leakage and ballistic limits of the aluminum targets.

Impact on sandwich panel (this part is removed from Paper 4. A comprehensive study on the impact response of CFRP plate will be done during the 2024-2025 academic year)

Material model for composite sandwich panel

The sandwich panel comprises plain weave (PW) carbon fiber epoxy facesheets paired with a hexagonal honeycomb core, as illustrated in Figure 6. The honeycomb core (HC) is constructed

from phenolic resin-impregnated aramid paper, commonly referred to as Nomex. Both the front and rear facesheets consist of four plain weave CFRP Hexply M92 plies. It is noteworthy that in the current study, both Nomex paper and CFRP fabric are treated as orthotropic materials, given their anisotropic properties. The equivalent orthotropic properties for Nomex paper and CFRP ply were sourced from literature and manufacturer datasheets, and these properties are listed in Table 1 and Table 2, respectively.

The impact velocities utilized in this study significantly exceed the ballistic limits of both the sandwich panel and its constituent parts, including the CFRP facesheets and the honeycomb core (HC). Therefore, to accurately simulate these high-velocity impacts, a simplified modeling approach was adopted. In the simulation, both the CFRP and HC were represented as single equivalent orthotropic layers. These layers were characterized by a non-progressive failure model, meaning that once the failure criterion was met, the elemental stress instantaneously reduced to zero, resulting in the complete failure of the damaged element. For the honeycomb core, a built-in material model designed for fiber-reinforced composites was employed. This model includes linear elastic properties and utilizes Hashin's failure criteria without incorporating a progressive damaging scheme.

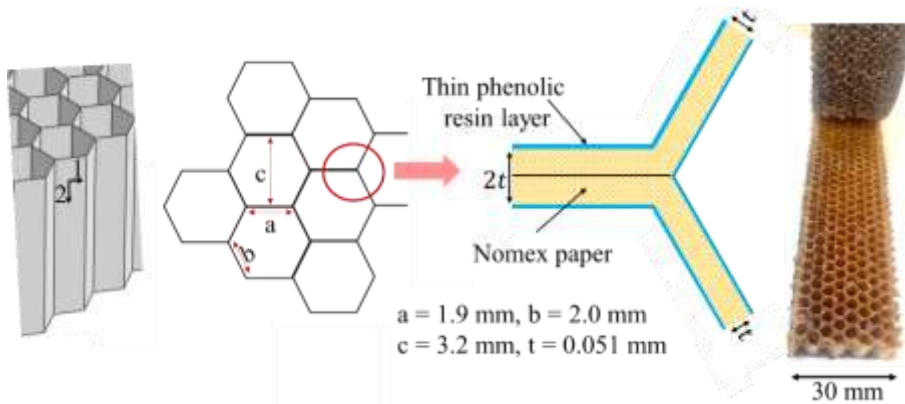


Fig. 1. The Nomex honeycomb core.

Table 1. Mechanical properties of Nomex material .

Properties	Symbol	Unit	Value
Elastic modulus 1-direction	E_1	GPa	5.00
Elastic modulus 2-direction	E_2	GPa	4.00
Shear modulus	G_{12}	GPa	1.45
Poisson's ratio	μ	-	0.2
Tensile strength 1-direction	X^T	MPa	90

Tensile strength 2-direction	Y^T	MPa	60
Compressive strength 1-direction	X^C	MPa	105
Compressive strength 2-direction	Y^C	MPa	90
Shear strength	S	MPa	44
Density	ρ	kg/m ³	1100
Single layer thickness	t	mm	0.051

Table 2. Mechanical properties of CFRP fabric.

Properties	Symbol	Unit	Value
Warp elastic modulus, 1-direction	E_1	GPa	50.2
Weft elastic modulus, 2-direction	E_2	GPa	50.2
Elastic modulus, the thickness direction	E_3	GPa	9.60
Shear moduli	$G_{12}, G_{13}^*, G_{23}^*$	GPa	2.5
Poisson's ratios	μ	-	0.13
Tensile strength (warp) 1-direction	X^T	MPa	687
Tensile strength (fill) 2-direction	Y^T	MPa	
Compressive strength (warp) 1-direction	X^C	MPa	564
Compressive strength (fill) 2-direction	Y^C	MPa	
Compressive strength 3-direction	Z^C	MPa	340 [23]
Shear strength	S, S_{13}^*, S_{23}^*	MPa	94
Density	ρ	kg/m ³	1440
Ply thickness	t	mm	0.239

*Assumed to be equal to G_{12} and S .

The response of the CFRP woven fabric plies is considered and modeled as an equivalent orthotropic elastic material until failure onsets, implemented through a VUMAT user-material subroutine in Abaqus/Explicit code. For composite materials, there are several failure theories such as Hashin's criteria and those presented by Hou et al., that consider two different failure mechanisms; fiber failure modes (in the 1-direction) and matrix failure modes (in the 2-direction). The failure theories mentioned are well-suited for unidirectional composite tapes, where mechanical properties in the fiber direction (1-direction) are controlled by the fibers, while properties and failure mechanisms in the transverse direction (2-direction) predominantly rely on matrix behavior. In this study, the woven fabric features an equal distribution of fibers in both in-plane orthogonal directions, resulting in the reinforcement of both directions (1 and 2) with fibers. Additionally, in alignment with references, a few adaptations were made to existing failure theories: (I) the incorporation of fiber failure criteria for both in-plane directions and (II) the exclusion of analogous matrix crushing and matrix cracking as seen in the model proposed by Hou et al..

The stress-based failure variables, denoted as d_i and expressed in Equations 4-7, have been established to account for various failure modes. These modes include fiber failure (d_{f1} , d_{f2}), in-plane shear failure (d_{m12}), and out-of-plane crushing (d_{m3}). The values of these failure variables can either be zero (indicating no damage) or one (the initiation of damage). When a damage variable reaches a value of one, the corresponding stress components are reduced to zero. The combination of the damage variables and the element deformation gradient was employed as a criterion for the element removal scheme.

$$\text{Fiber failure in the 1-direction: } d_{f1} = \begin{cases} \left(\frac{\sigma_{11}}{X^T}\right)^2 + \left(\frac{\sigma_{12}^2 + \sigma_{13}^2}{S^2}\right) & \sigma_{11} > 0 \\ \frac{|\sigma_{11}|}{X^C} & \sigma_{11} < 0 \end{cases} \quad (1)$$

$$\text{Fiber failure in the 2-direction: } d_{f2} = \begin{cases} \left(\frac{\sigma_{22}}{Y^T}\right)^2 + \left(\frac{\sigma_{12}^2 + \sigma_{13}^2}{S^2}\right) & \sigma_{22} > 0 \\ \frac{|\sigma_{22}|}{Y^C} & \sigma_{22} < 0 \end{cases} \quad (2)$$

In the event of fiber failure, as indicated by the fulfillment of Eqs. (1,2), all components of the elastic matrix are promptly nullified, resulting in a complete loss of material stiffness at the respective integration point. Conversely, for matrix failure, two distinct criteria, represented by Eqs. (3) and (4), can be expressed as follows.

$$\text{In-plane shear: } d_{m12} = \frac{\sigma_{12}}{S} \quad (3)$$

$$\text{Out-of-plane crushing: } d_{m3} = \frac{1}{4} \left(\frac{\sigma_{33}}{Z^C} \right)^2 + \frac{z^C \sigma_{33}}{4S_{13}S_{23}} + \frac{|\sigma_{33}|}{Z^C} + \max \left[\left(\frac{\sigma_{13}}{S_{13}} \right)^2, \left(\frac{\sigma_{23}}{S_{23}} \right)^2 \right] \quad (4)$$

The front and rear facesheets of the sandwich panel consist of four woven plies. However, in the finite element (FE) model, the facesheets are represented using two layers of three-dimensional solid elements. The surface-based cohesive interaction model is employed between the two layers of facesheets to allow intralaminar delamination. To ensure structural integrity, the front and rear CFRP facesheets are bonded to the Nomex core using a rigid tie interaction method.

The intralaminar behavior of adjacent CFRP plies was modeled using the built-in cohesive model with a traction-separation law in Abaqus software. The mechanical properties of the interface can be found in Table 3. Linear elastic and uncoupled behavior were assumed for the interface model until the point of failure onset, as defined by Eq. (5). Delamination onset was predicted using the quadratic nominal stress failure criterion outlined in Eq. (6).

$$\begin{Bmatrix} t_n \\ t_s \\ t_t \end{Bmatrix} = \begin{bmatrix} K_n & 0 & 0 \\ 0 & K_s & 0 \\ 0 & 0 & K_t \end{bmatrix} = \begin{Bmatrix} \varepsilon_n \\ \varepsilon_s \\ \varepsilon_t \end{Bmatrix} \quad (5)$$

where $\{t\}$ represents the traction vector, $\{\varepsilon\}$ represents the strain vector; K penalty stiffness parameters of interface material.

$$\left\{ \frac{\langle t_n \rangle}{t_n^0} \right\}^2 + \left\{ \frac{\langle t_s \rangle}{t_s^0} \right\}^2 + \left\{ \frac{\langle t_t \rangle}{t_t^0} \right\}^2 = 1 \quad (6)$$

where t_n^0 , t_s^0 and t_t^0 represent the peak values of the nominal stress when the deformation is either purely normal to the interface or purely in the first or the second shear direction, respectively. When the damage initiation criterion is met, delamination failure will propagate according to the mixed-mode energy-based law, assigned in the model with the Benzeggagh-Kenane (BK) formula, as expressed in Eq.7.

$$G_n^C + (G_s^C - G_n^C) \left(\frac{G_s + G_t}{G_n + G_s + G_t} \right)^\eta = G^C \quad (7)$$

Table 3. Mechanical properties of interface layers [31].

Peak strength (MPa)	t_n^0	64
	t_s^0	84
	t_t^0	84
	G_n	0.8
Critical fracture toughness (N/mm)	G_s	1.5
	G_t	1.5
	K_n	3000
Penalty stiffness (N/mm ³)	K_s	3000
	K_t	3000

Note: The cohesive property parameter $\eta= 1.45$ is selected.

Results and discussion

In this section, first, the results of the impact tests for ConfigI are presented. The experimental results of the initial configuration were employed for the calibration and validation of the numerical model. This process aimed to enable the numerical model to predict the leakage velocity limits for aluminum plates with different thicknesses.

In the second part of this section, the numerical results of impact ConfigII are presented alongside the experimental impact and leakage tests conducted on 4.66 mm thick aluminum targets. The aim was to evaluate whether the numerical model developed in this study can be considered a reliable tool for predicting the leakage limits of aluminum aircraft fuel tanks.

The striking velocities employed were significantly higher than the ballistic limit of the CFRP sandwich panel. Consequently, only minor velocity reductions, approximately amounting to 4% of the initial striking velocities, were observed for the projectile after it had passed through the sandwich panel, as depicted in Fig. 2. The velocity reductions resulting from the impact on the sandwich panel were indeed small. However, it is important to recognize that even these minor reductions could potentially affect the extent of damage to the aluminum target, consequently influencing the outcomes of the leakage tests. The FE model predicted residual velocities after impacting the sandwich panel approximately 5% lower than the observed experimental values. Alongside this good agreement between FE residual velocities and experimental measurements, there are similarities between the penetration modes of the cubical projectile and the extent of damage on the sandwich panels, as shown in Figs. 2 and 3.

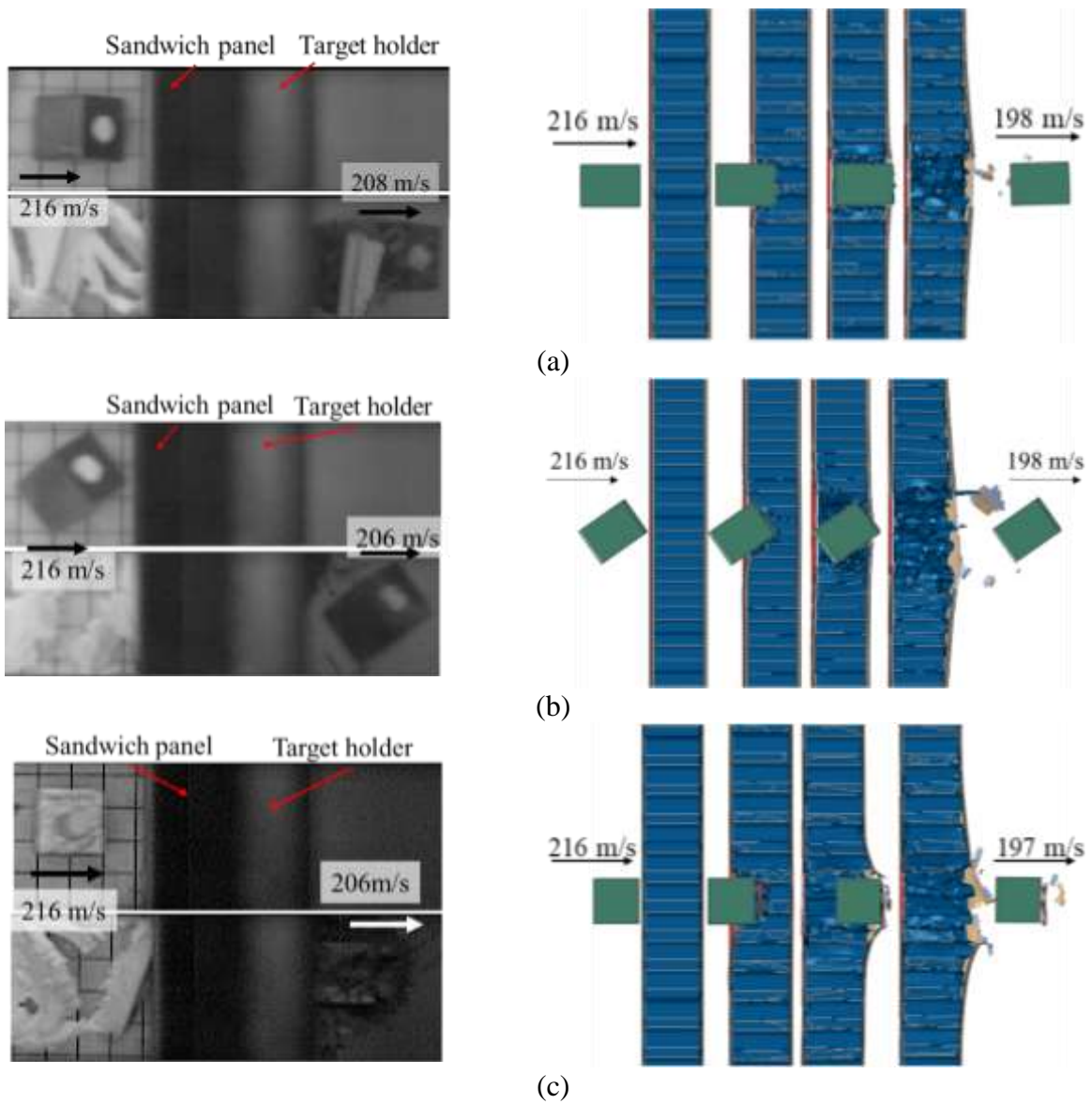


Fig. 2. High-velocity impact on CFRP sandwich panels; (1) Edge-on impact orientation, (b) Corner-on impact orientation, and (c) Face-on impact orientation.

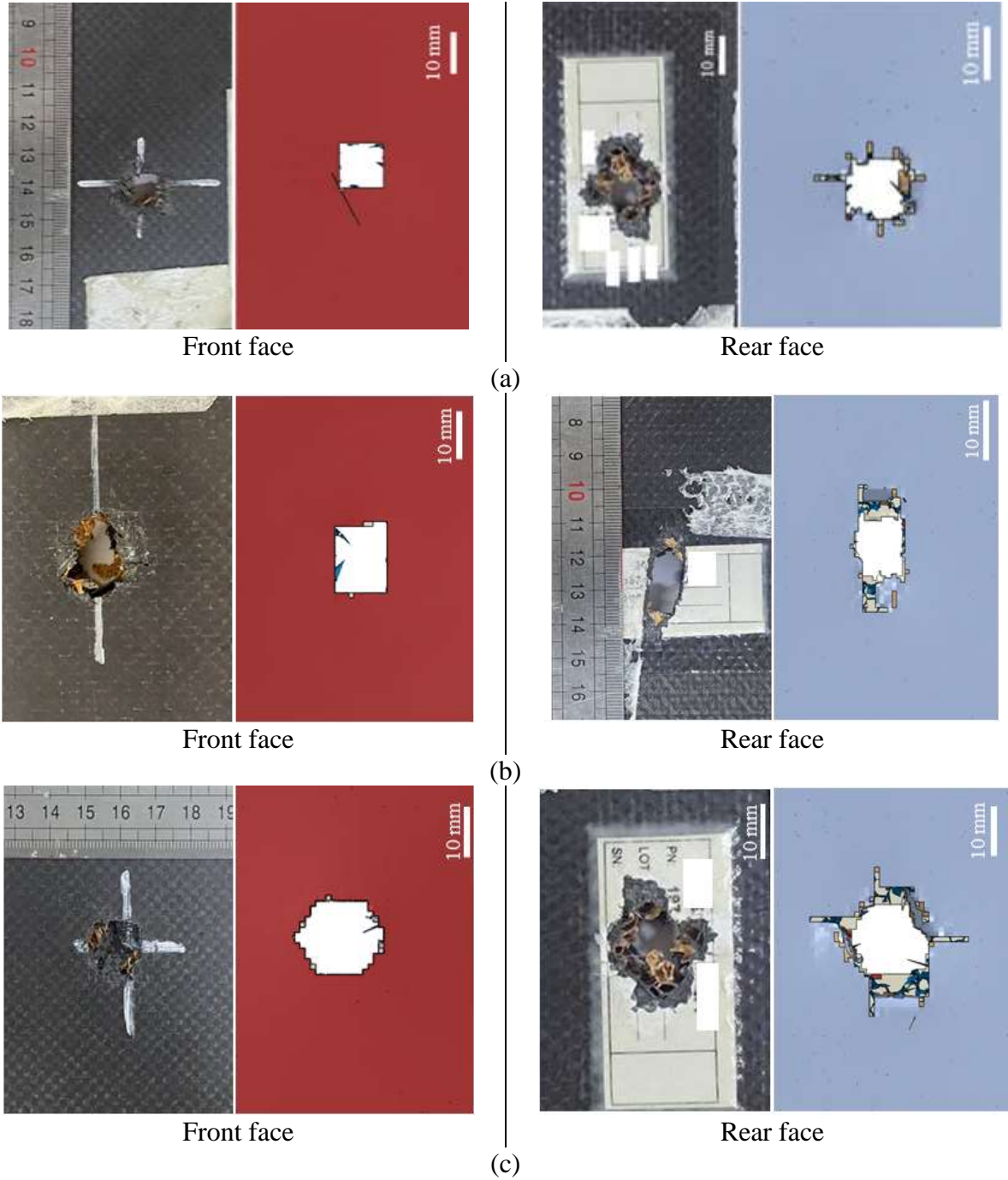


Fig. 3. Localized damage on the CFRP sandwich panel; (a) Face-on impact orientation, (b) Edge-on impact orientation, and (c) Corner-on impact orientation.

In addition to the reduction in velocity, the presence of the CFRP sandwich panel and the 200 mm air gap leading to the aluminum target had a notable impact on the angle at which cubical projectiles struck the aluminum target. Figure 15 illustrates the damage to the aluminum plates in Impact Config II. In general, it was observed that the change in the impact orientation was

remarkably significant for the face-on impact orientation rather than corner-on and edge-on impact orientations, as shown in Fig. 4. Figure 4 illustrates that even when there was zero deviation from the desired impact orientations, the numerical models, sandwich panel, and air gap resulted in a significant alteration of the impact angles on the second target (the aluminum plate). This effect is even more pronounced in the case of experimental tests. For all valid strikes (with less than ± 5 degrees deviation in two orthogonal view planes), there was a slight deviation from the ideal impact orientation in at least one view plane. The sandwich panel and air gap amplified this minor deviation when the cubical projectile reached the aluminum target. The effect of deviations from the edge-on orientation on the leakage limit velocity of the aluminum plate is explored in the following subsection.

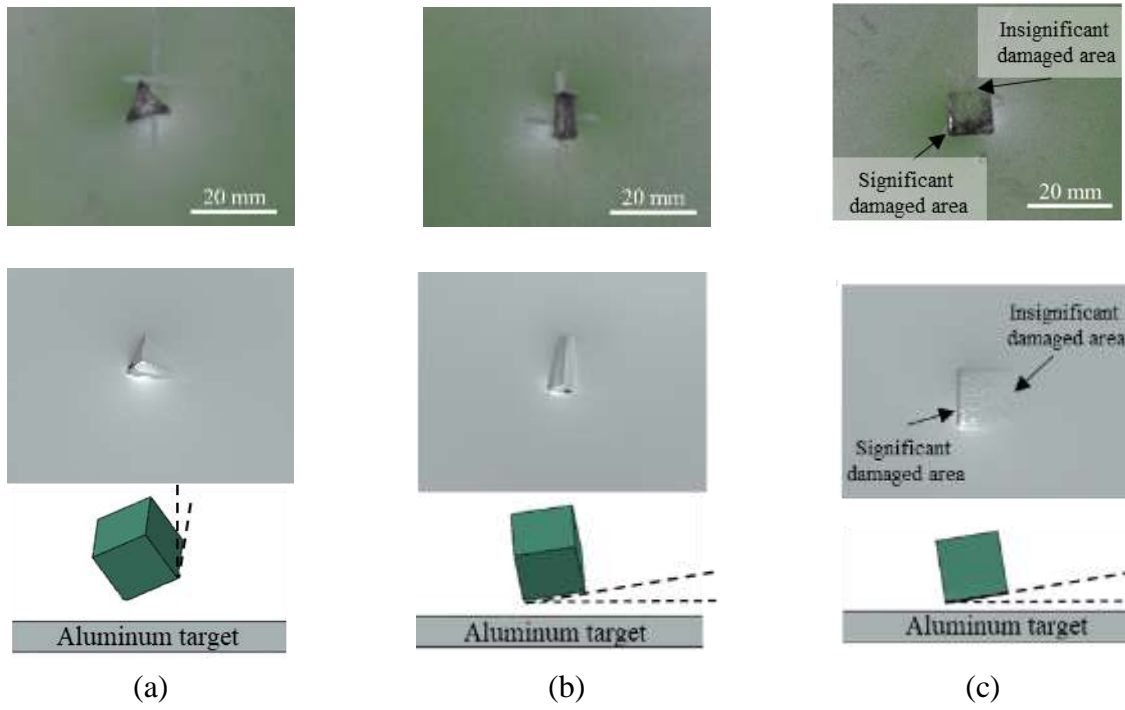


Fig. 4. Experimental and numerical impact-induced damage on the aluminum plates in impact ConfigII and change in the cube orientation due to sandwich panel and 200 mm air gap just before hitting the aluminum target; (a) Corner-on orientation, (b) Edge-on orientation, and (c) Face-on orientation.

Based on the results obtained from experimental impact and leakage tests conducted on the 4.66 mm thick aluminum targets in ConfigII, it was observed that all targets successfully passed the leakage test criteria. Consequently, using the finite element (FE) model, the leakage limit velocity for the 4.66 mm thick aluminum plate impacted by the edge-on, corner-on, and face-on

impact orientations was predicted. According to the results provided in Table 9, the corner-on impact orientation resulted in the lowest leakage limit velocity, while the highest leakage limit velocity was recorded for the face-on impact orientation. This indicates that projectiles with sharper noses led to lower leakage limit velocities. The influence of projectile nose sharpness on the leakage limit velocity does not align with the impact of projectile nose sharpness on the ballistic limit velocities. For example, in literature, that studied the performance of AA2024-T351 plates, it was observed that edge-on impact resulted in the lowest ballistic limit, whereas corner-on impact led to the highest ballistic limit velocity. It is worth noting that this observation is consistent with the numerical results obtained for AA 7475-T7351 targets in the current study for ballistic limit velocities.

VUMAT subroutine for CFRP facesheets

(VUMAT is used and validated in Paper 3- only damage(s) initiation criteria, damage evolution law, and element deletion scheme presented here)

```

*
E11 = strain(k,i_s33_Xx)
E22 = strain(k,i_s33_Yy)
E12 = strain(k,i_s33_Xy)

*
*      Failure evaluation 1
*      if ( (E11) .ge. zero ) then
*-- Tensile Fiber Mode
rft =(E11/E01t)**2
if ( (rft) .ge. one ) then
  lDmg1 = 1
  Ef1t=2*G1t/(f1t)/charLength(k)
  dft(k)=Ef1t*(sqrt(E11**2) -
*          *sqrt( E01t**2))/(
*          (sqrt(E11**2)*
*          (Ef1t-sqrt(E01t**2)))
  if (dft(k).ge. one) then
    dft(k)=1
  end if
  if (dft(k).le. zero) then
    dft(k)= zero
  end if
end if

```

```

        else if ( E11 .lt. zero) then
*
*   -- Failure evaluation 2
        rfc = ((E11/E01c))**2
        if ( (rfc) .ge. one ) then
          lDmg2 = 1
          Ef1c=2*G1c/(f1c)/charLength(k)
          dfc(k)=Ef1c*(abs(E11)-E01c)/
          (abs(E11)*
           (Ef1c-E01c))
          if (dfc(k).ge. one) then
            dfc(k)=1
          end if

          else if (dfc(k).le. zero) then
            dfc(k)= zero
          end if
          end if

*
*   Failure evaluation 3
        if ( (E22) .ge. zero) then
*
*   -- Tensile Fiber Mode
        rmt =(E22/E02t)**2
        if ( (rmt) .ge. one ) then
          lDmg3 = 1
          Ef2t=2*G2t/(f2t)/charLength(k)
          dmt(k)=Ef2t*(sqrt(E22**2) -
          *          sqrt( E02t**2))/
          *          (sqrt(E22**2)*
           (Ef2t-sqrt(E02t**2)))
          if (dmt(k).ge. one) then
            dmt(k)=1
          end if
          if (dmt(k).le. zero) then
            dmt(k)= zero
          end if

        end if

        else if ( E22 .lt. zero ) then
*
*   -- Failure evaluation 4
        rmc = (E22/E02c)**2
        if ( (rmc) .ge. one ) then
          lDmg4 = 1
          Ef2c=2*G2c/(f2c)/charLength(k)
          dmc(k)=Ef2c*(sqrt(E22**2) -
          *          sqrt( E02c**2))/
          *          (sqrt(E22**2)*
           (Ef2c-sqrt(E02c**2)))
          if (dmc(k).ge. one) then
            dmc(k)=1
          end if
          if (dmc(k).le. zero) then
            dmc(k)= zero
          end if
        end if

```

```

    end if

dmgftnew(k)=MAX(dmgftold(k),dft(k))
dmgfcnew(k)=MAX(dmgfcold(k),dfc(k))
dmgmtnew(k)=MAX(dmgmtold(k),dmt(k))
dmgmcnew(k)=MAX(dmgmcold(k),dmc(k))

*
eigMax=max(eigen(k,i_v3d_X),eigen(k,i_v3d_Y),eigen(k,i_v3d_Z))
eigMin=min(eigen(k,i_v3d_X),eigen(k,i_v3d_Y),eigen(k,i_v3d_Z))
enomMax = eigMax - one
enomMin = eigMin - one

if ((dmgftnew(k).gt.fz.AND.(enomMax. gt. eMax)).or.
(*
(*
(*
(dmgfcnew(k).gt.fz.AND. enomMin. lt. eMin ).or.
(dmgmcnew(k).gt.fz.AND. enomMin .lt. eMinm).or.
(dmgmtnew(k).gt.fz.AND. enomMax .gt. eMaxm) ) then
    statusMp(k) = zero
else
    statusMp(k) = one
end if

C
*

```

Part 2

DYNAMIC FRICTION COEFFICIENTS FOR CRASHWORTHINESS APPLICATIONS

Dr. Pouria Bahrami Prof. Marcilio Alves

December 2023

Crashworthiness stands as a pivotal and formidable facet within the automotive design paradigm. Within finite element crash simulation, friction emerges as a critical parameter, wielding substantial sway over vehicle kinematics and occupant interactions alike. Throughout the crash event, friction undergoes dynamic shifts, necessitating its characterization across diverse slip rates and contact pressures. To address this exigency, a dedicated test rig was conceptualized, constructed, and operationalized. Its purpose was to facilitate the measurement of friction coefficients for both rigid and compliant material pairs.

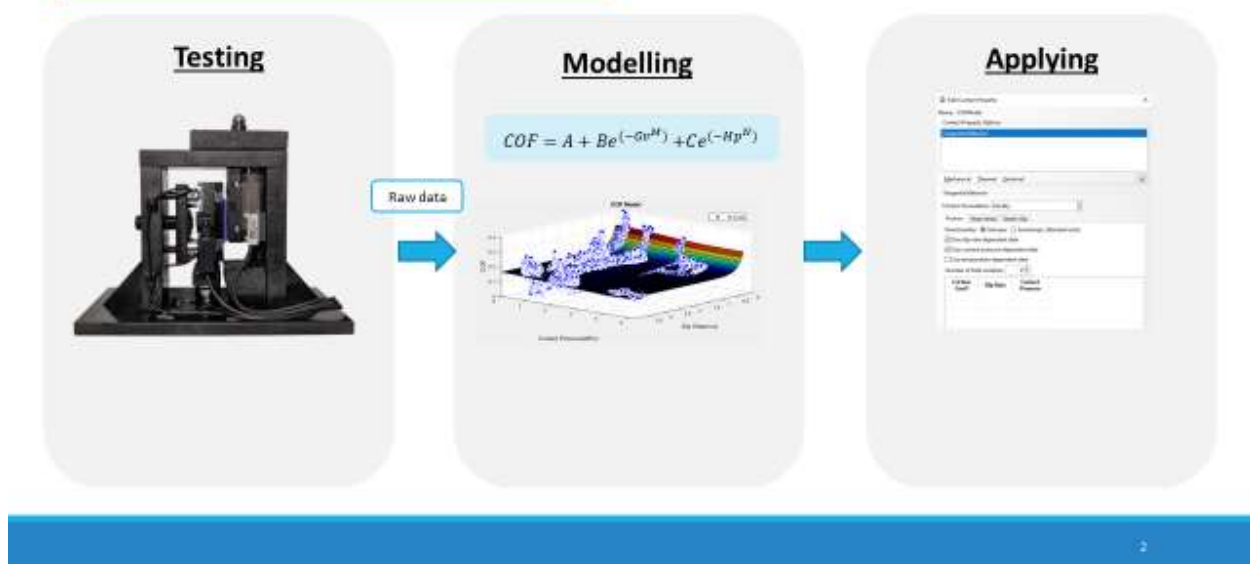


Quasi-static friction test (Qs tests were conducted for the first time)



Dynamic friction tests.

Methodology



The Friction Model

$$COF = A + Be^{(-Gv^M)} + Ce^{(-Hp^N)}$$

- **A** is the independent coefficient (controls minimum overall COF)
- **B** and **C** are coefficients associated to slip rate and contact pressure, respectively (controls decay amplitude)
- **G** and **H** are the exponential coefficients associated to slip rate and contact pressure, respectively (Controls decay rate)
- **M** and **N** are the variables exponents (controls decay shape)
- **v** is the slip rate variable
- **p** is the contact pressure variable

Friction Rig



Tests layout

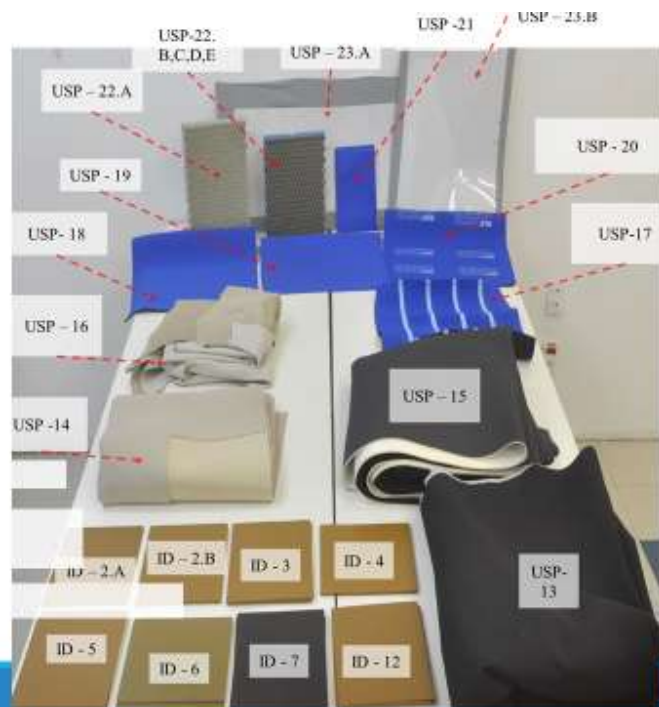
Internal parts:

USP-17, 20 and 21 seem to be combinations or variants of USP18 and USP19

USP-18 and USP-19 are considered master surfaces and tested against other parts

External parts:

USP23A vs. USP-22



Test scenarios

Slip rates:

Each test repeated twice

QS tests: 3 mm/min

Dynamic tests: ~1,5 m/s & ~ 2,5 m/s

Contact pressures

Dynamic tests: ~1 MPa, ~2 MPa and ~ 3,5 MPa

QS tests: ~0,5 MPa, ~2 MPa and ~ 4 MPa

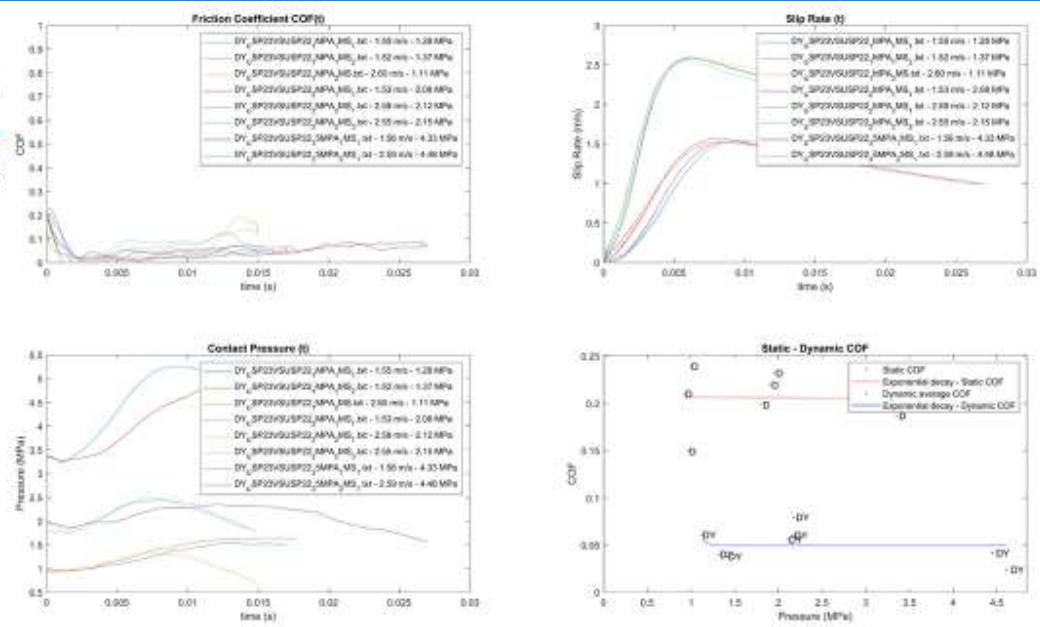
Results

Car exterior vs. Facesheet of honeycomb barrier



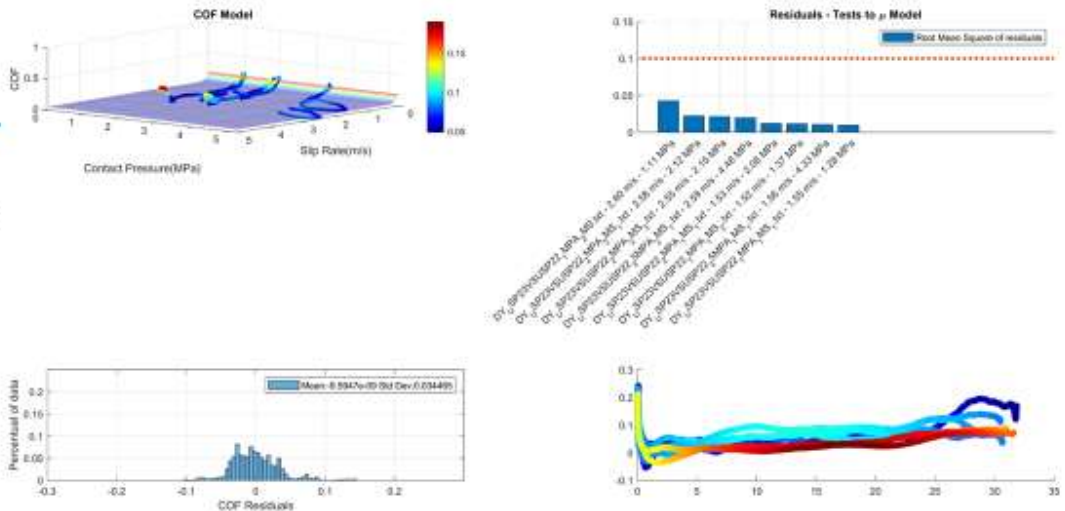
Results

Car exterior vs. Facesheet of honeycomb barrier



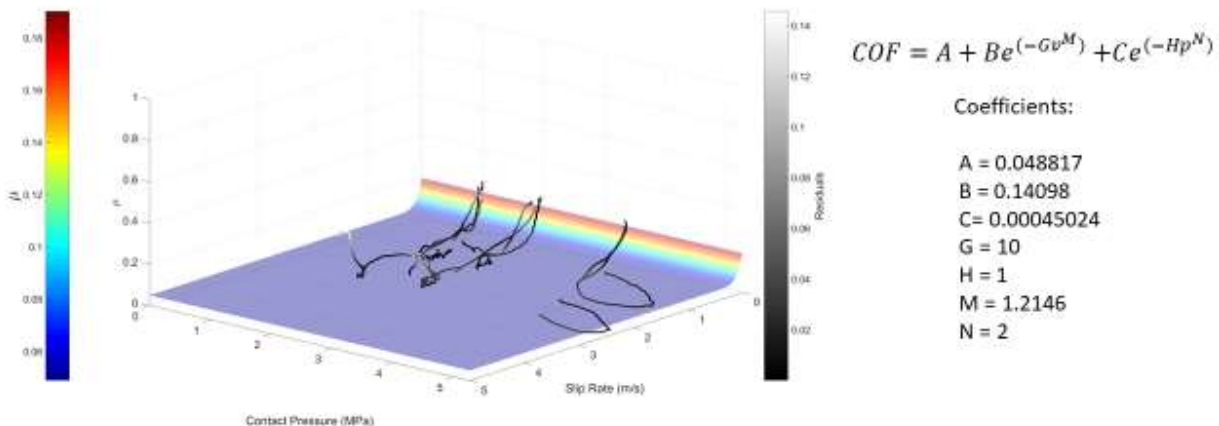
Results

**Car exterior
vs. Facesheet
of honeycomb
barrier**



Results

Car exterior vs. Facesheet of honeycomb barrier



Results

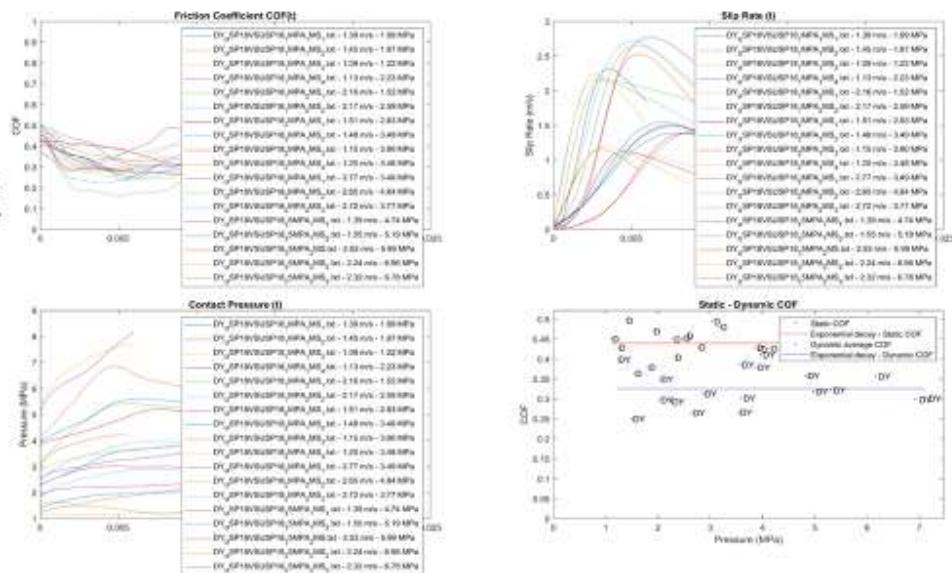
Blue Neouperen (USP-18) vs. Blue Neouperen (USP-18)



11

Results

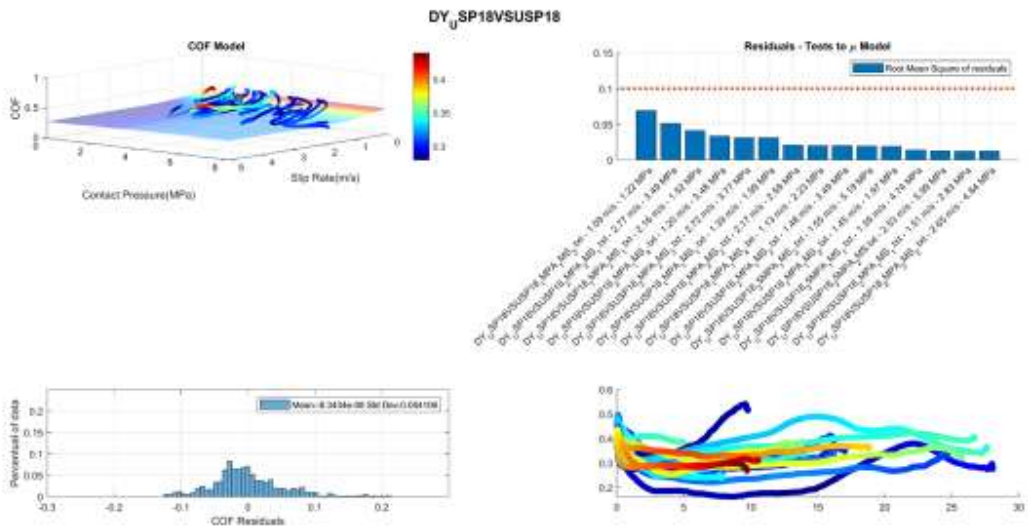
Blue Neouperen
(USP-18) vs. Blue
Neouperen (USP-18)



12

Results

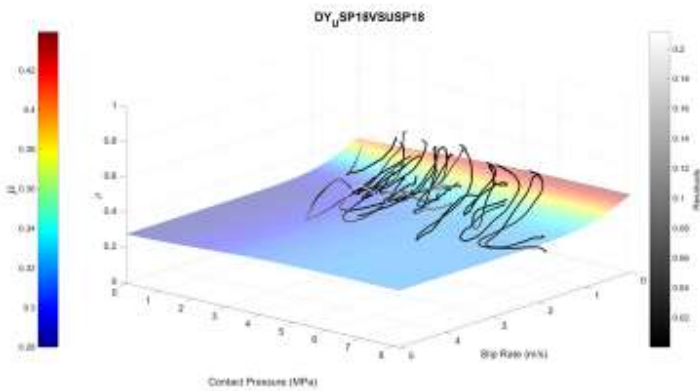
**Blue
Neouperen
(USP-18) vs.
Blue
Neouperen
(USP-18)**



13

Results

Blue Neouperen (USP-18) vs. Blue Neouperen (USP-18)



$$COF = A + Be^{(-Gv^M)} + Ce^{(-Hv^N)}$$

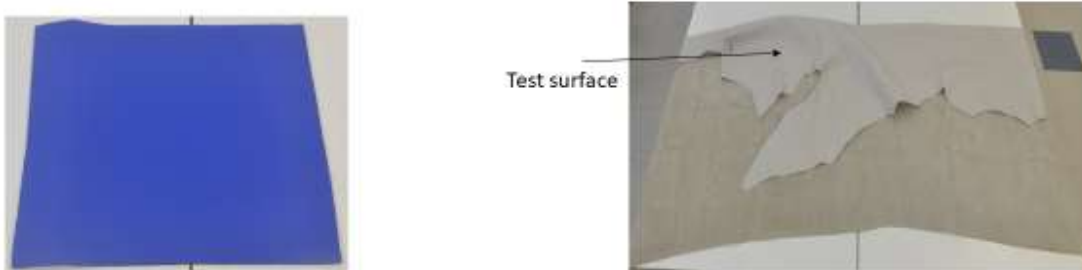
Coefficients:

$$\begin{aligned} A &= 0.32145 \\ B &= 0.11784 \\ C &= -0.041656 \\ G &= 1.502 \\ H &= 0.32549 \\ M &= 1.367 \\ N &= 2 \end{aligned}$$

14

Results

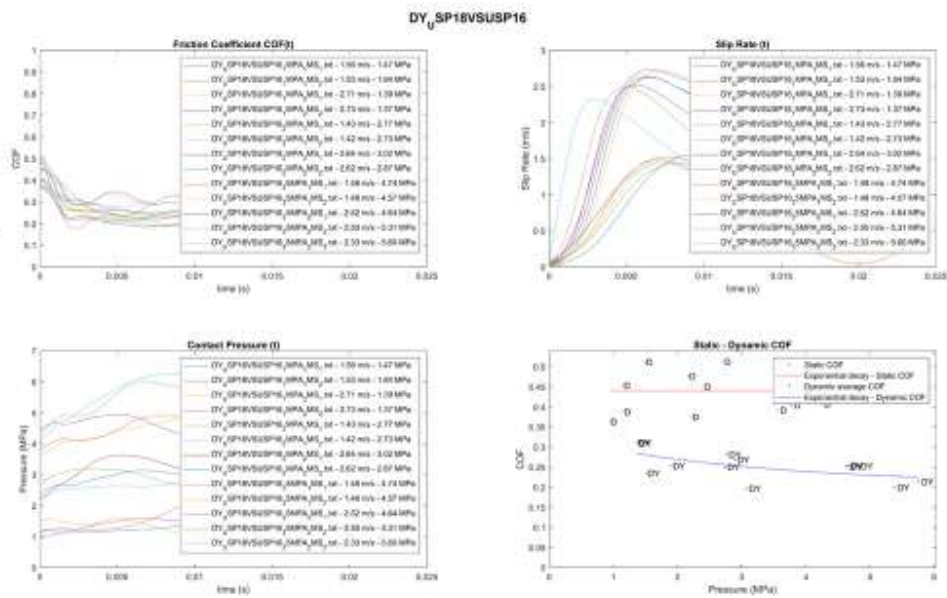
Blue Neouperen (USP-18) vs. seat textile/leather - Leder unkaschiert (USP-16)



15

Results

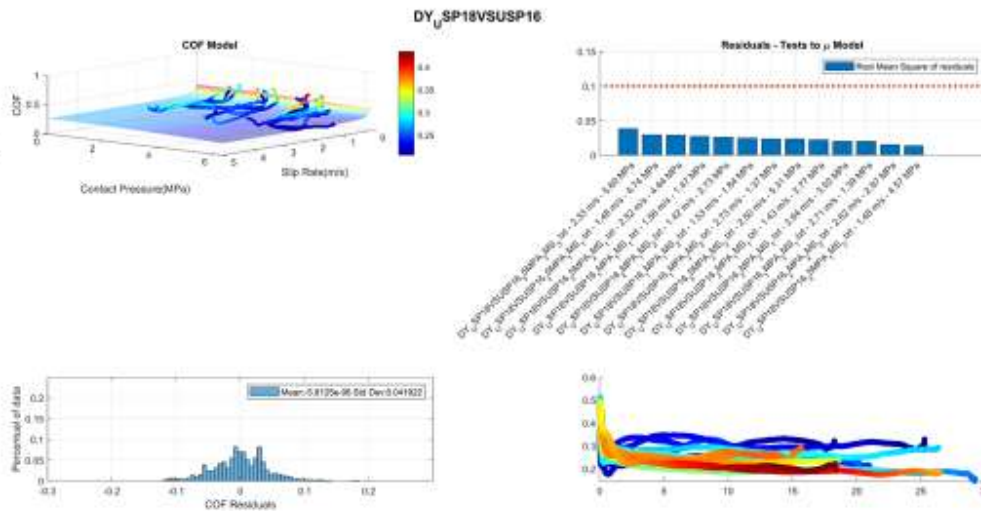
Blue Neouperen (USP-18) vs. seat textile/leather - Leder unkaschiert (USP-16)



16

Results

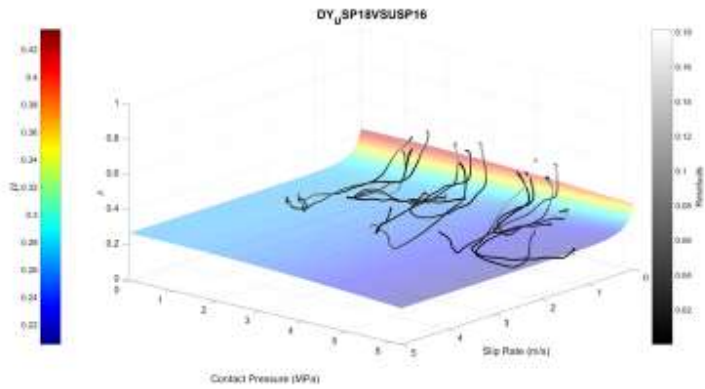
**Blue Neouperen
(USP-18) vs. seat
textile/leather -
Leder
unkaschiert
(USP-16)**



17

Results

Blue Neouperen (USP-18) vs. seat textile/leather - Leder unkaschiert (USP-16)



$$COF = A + Be^{(-Gv^M)} + Ce^{(-Hv^N)}$$

Coefficients:

$A = 1.3521e-05$
 $B = 0.16536$
 $C = 0.26915$
 $G = 5.9698$
 $H = 0.082676$
 $M = 0.78059$
 $N = 2$

18

Results

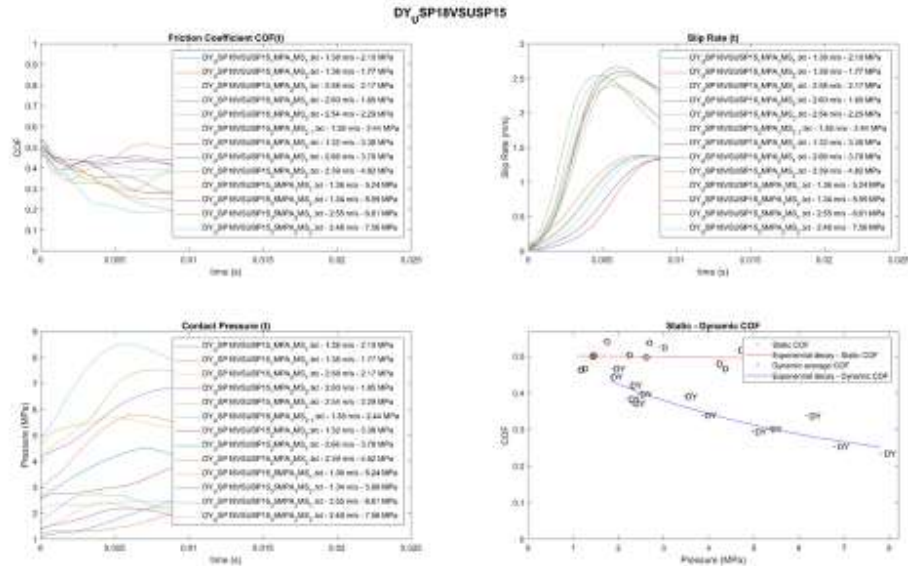
Blue Neouperen (USP-18) vs. seat textile/leather - Stoff-Schaum-Kaschier (USP-15)



19

Results

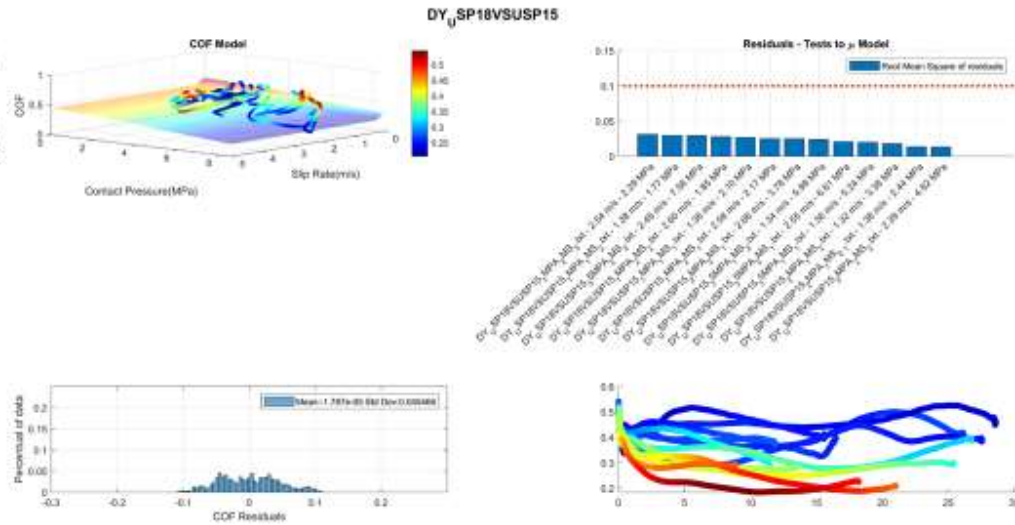
Blue
Neouperen
(USP-18) vs.
seat
textile/leather -
Stoff-Schaum-
Kaschier (USP-
15)



20

Results

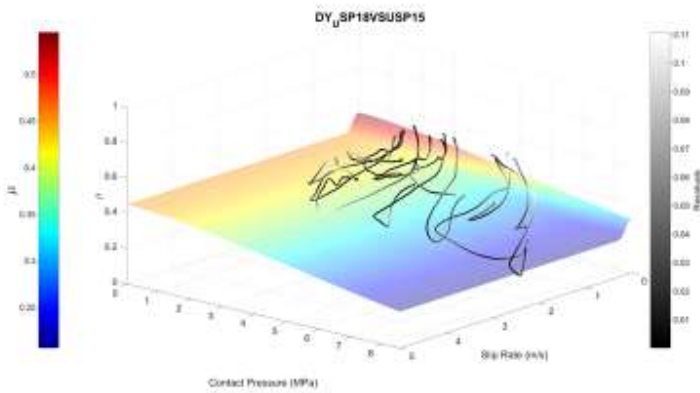
Blue Neouperen (USP-18) vs. seat textile/leather - Stoff-Schaum-Kaschier (USP-15)



21

Results

Blue Neouperen (USP-18) vs. seat textile/leather - Stoff-Schaum-Kaschier (USP-15)



$$COF = A + Be^{(-Gv^M)} + Ce^{(-Hv^N)}$$

Coefficients:

$A = 1.9086e-08$
 $B = 0.09399$
 $C = 0.4509$
 $G = 5.7726$
 $H = 0.10005$
 $M = 2.7046$
 $N = 1.5467$

22

Results

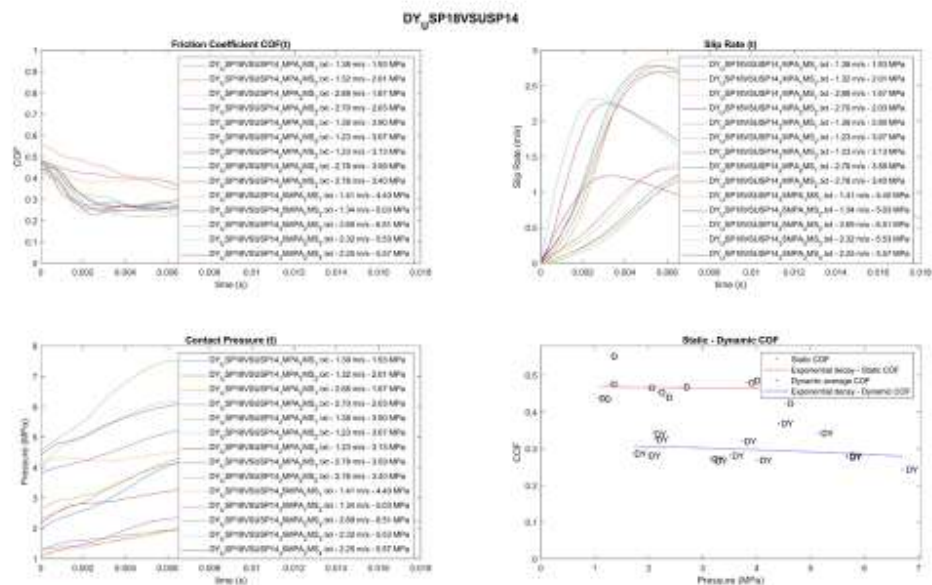
Blue Neouperen (USP-18) vs. seat textile/leather - Veganza mit Vlies (USP-14)



23

Results

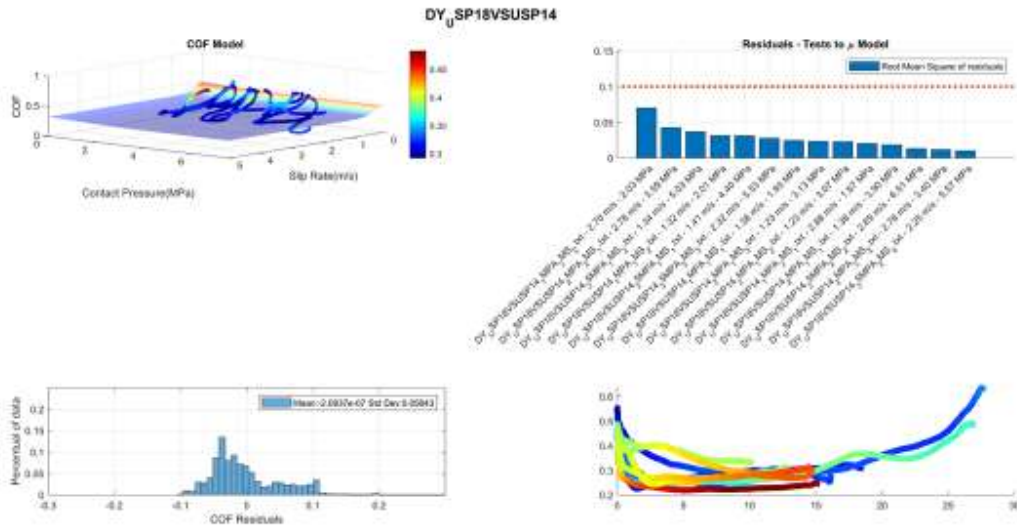
Blue Neouperen (USP-18) vs. seat textile/leather - Veganza mit Vlies (USP-14)



24

Results

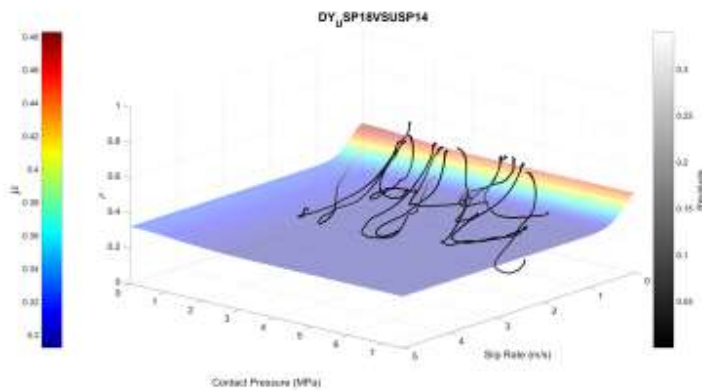
Blue Neouperen (USP-18) vs. seat textile/leather - Veganza mit Vlies (USP-14)



25

Results

Blue Neouperen (USP-18) vs. seat textile/leather - Veganza mit Vlies (USP-14)



$$COF = A + Be^{(-Gv^M)} + Ce^{(-Hv^N)}$$

Coefficients:

$A = 0.29218$
 $B = 0.1583$
 $C = 0.032272$
 $G = 2.6111$
 $H = 0.60441$
 $M = 1.7134$
 $N = 2$

26

Results

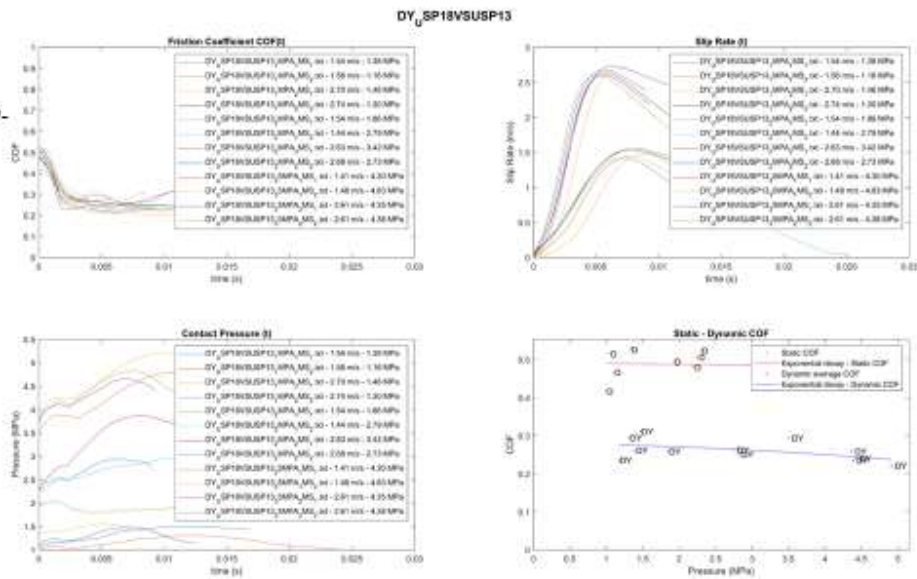
Blue Neouperen (USP-18) vs. seat textile/leather – Alcantara (USP-13)



27

Results

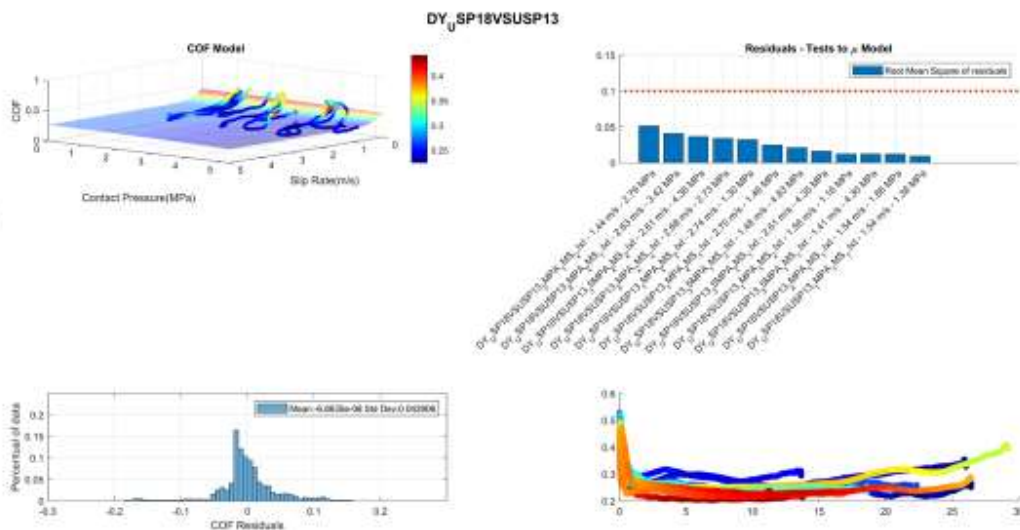
Blue Neouperen (USP-18) vs. seat textile/leather – Alcantara (USP-13)



28

Results

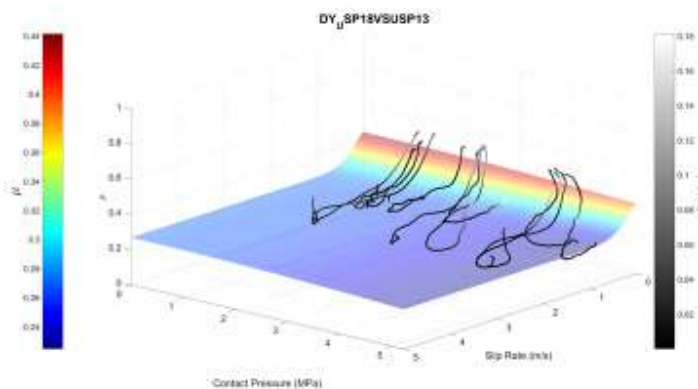
Blue Neouperen (USP-18) vs. seat textile/leather – Alcantara (USP-13)



29

Results

Blue Neouperen (USP-18) vs. seat textile/leather – Alcantara (USP-13)



$$COF = A + Be^{(-Gv^M)} + Ce^{(-Hv^N)}$$

Coefficients:

$A = 5.3668e-06$
 $B = 0.17243$
 $C = 0.26916$
 $G = 2.9006$
 $H = 0.081242$
 $M = 1.404$
 $N = 2$

30

Results

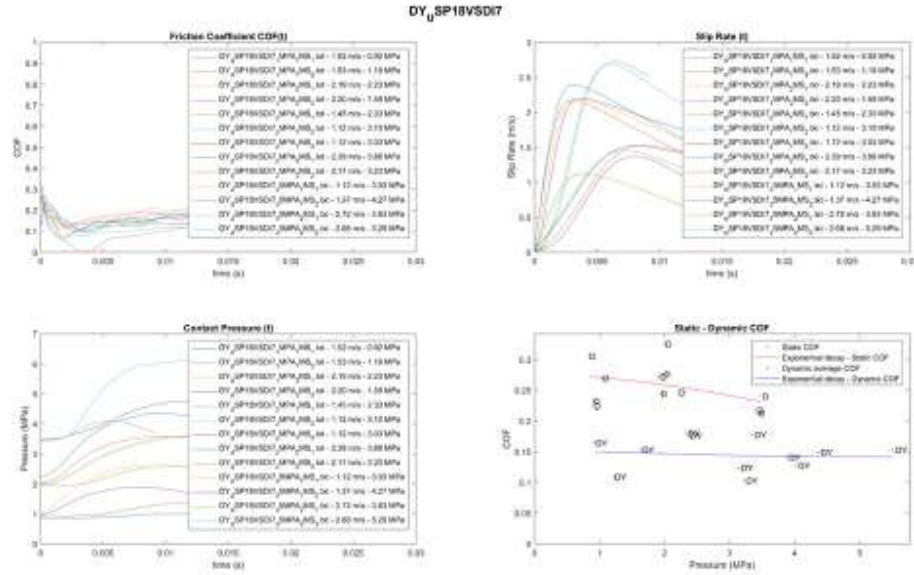
Blue Neouperen (USP-18) vs. dummy flesh (ID7)



31

Results

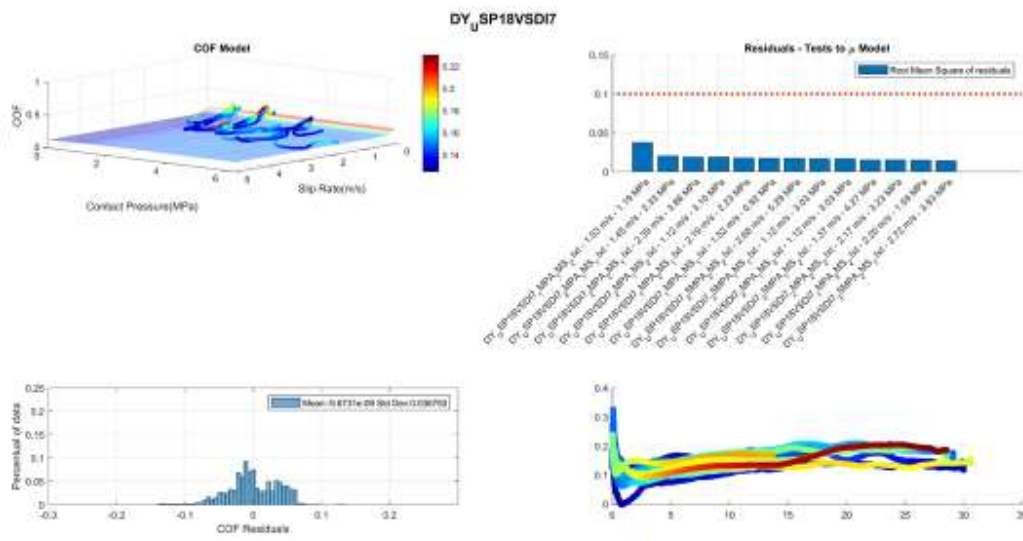
Blue
Neouperen
(USP-18)
vs.
dummy flesh
(ID7)



32

Results

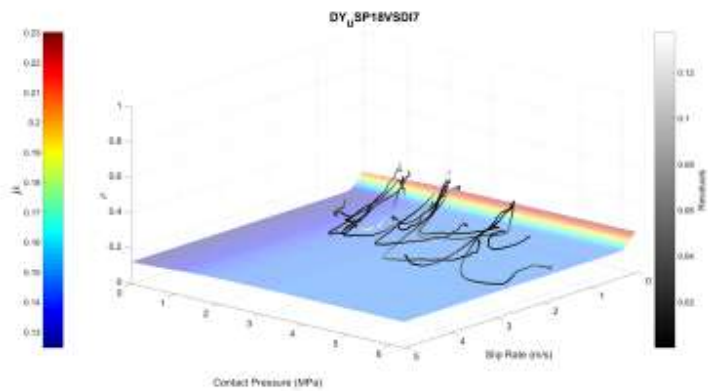
Blue Neouperen (USP-18) vs. dummy flesh (ID7)



33

Results

Blue Neouperen (USP-18) vs. dummy flesh (ID7)



$$COF = A + Be^{(-Gv^M)} + Ce^{(-Hv^N)}$$

Coefficients:

$A = 0.14785$
 $B = 0.082391$
 $C = -0.023154$
 $G = 5.6796$
 $H = 0.79131$
 $M = 1.891$
 $N = 2$

34

Results

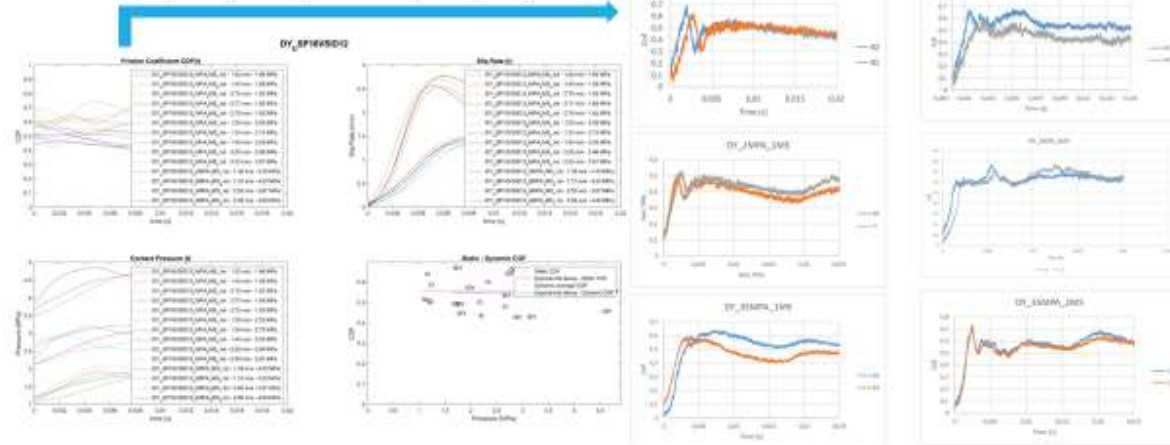
Blue Neouperen (USP-18) vs. dummy flesh (ID12)



35

Results

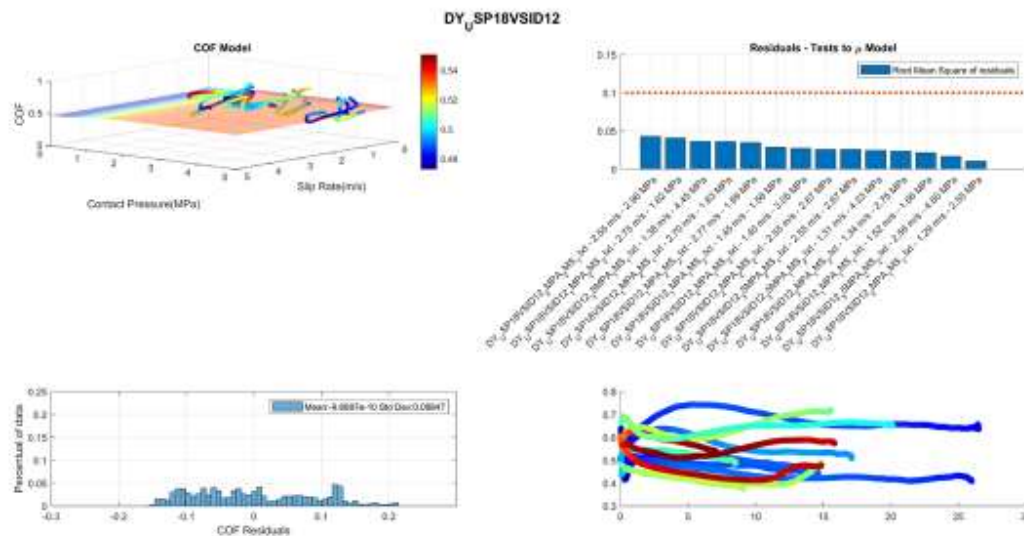
Blue Neouperen (USP-18) vs. dummy flesh (ID12)



36

Results

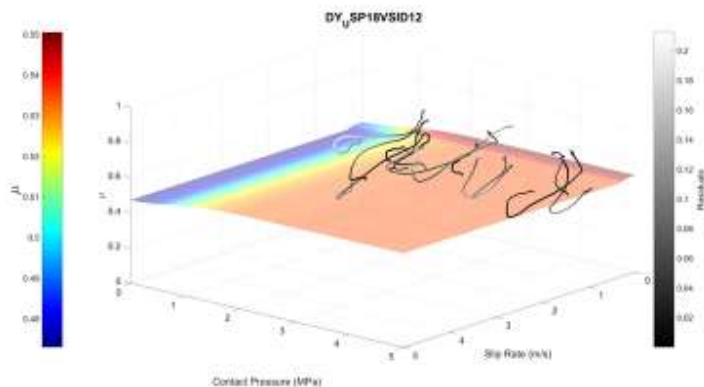
Blue Neouperen (USP-18) vs. dummy flesh (ID12)



37

Results

Blue Neouperen (USP-18) vs. dummy flesh (ID12)



$$COF = A + Be^{(-Gv^M)} + Ce^{(-Hv^N)}$$

Coefficients:

$$\begin{aligned} A &= 0.53365 \\ B &= 0.016896 \\ C &= -0.060662 \\ G &= 3.5805 \\ H &= 1 \\ M &= 4.9999 \\ N &= 2 \end{aligned}$$

38

Results

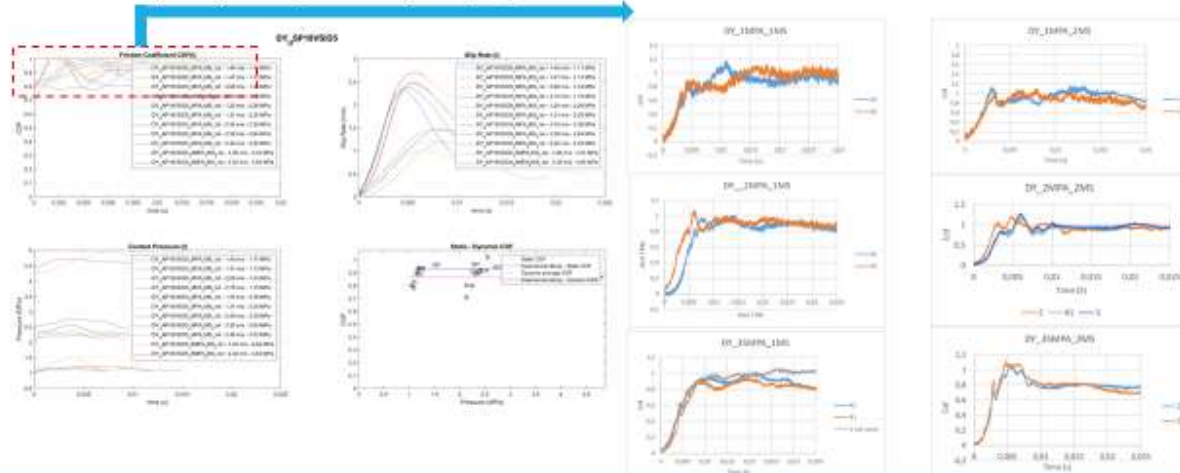
Blue Neouperen (USP-18) vs. dummy flesh (ID5)



39

Results

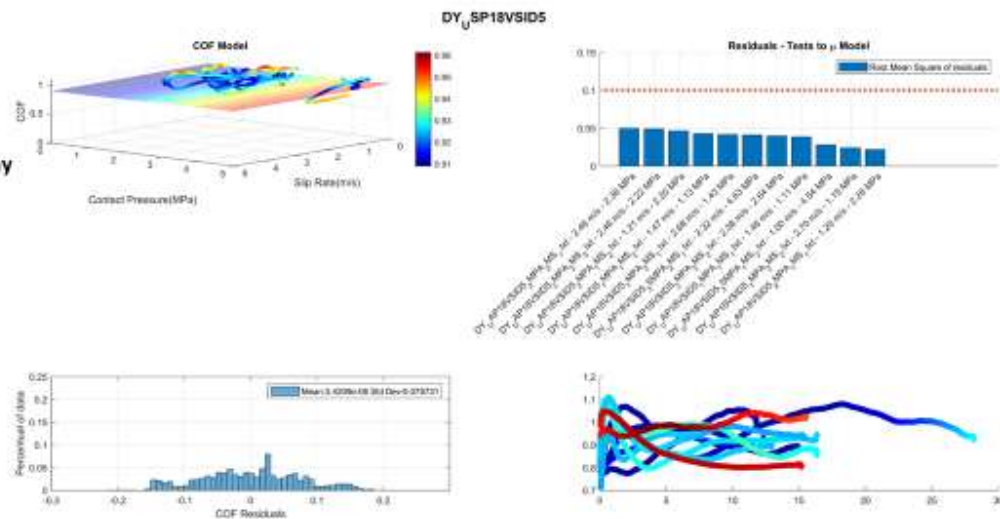
Blue Neouperen (USP-18) vs. dummy flesh (ID5)



40

Results

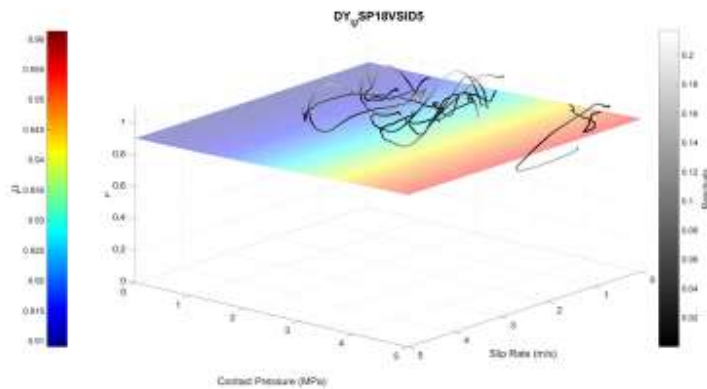
Blue Neouperen
(USP-18) vs. dummy
flesh (ID5)



41

Results

Blue Neouperen (USP-18) vs. dummy flesh (ID5)



$$COF = A + Be^{(-Gv^M)} + Ce^{(-Hv^N)}$$

Coefficients:

$$\begin{aligned} A &= 0.96795 \\ B &= 0.01 \\ C &= -0.062894 \\ G &= 0.050067 \\ H &= 0.2307 \\ M &= 0.05 \\ N &= 2 \end{aligned}$$

42

Results

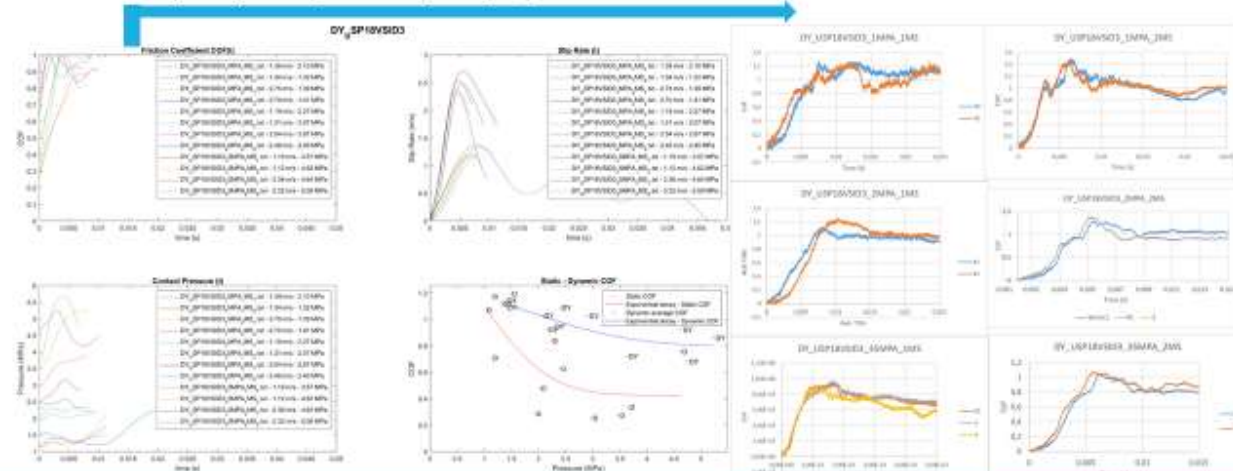
Blue Neouperen (USP-18) vs. dummy flesh (ID3)



43

Results

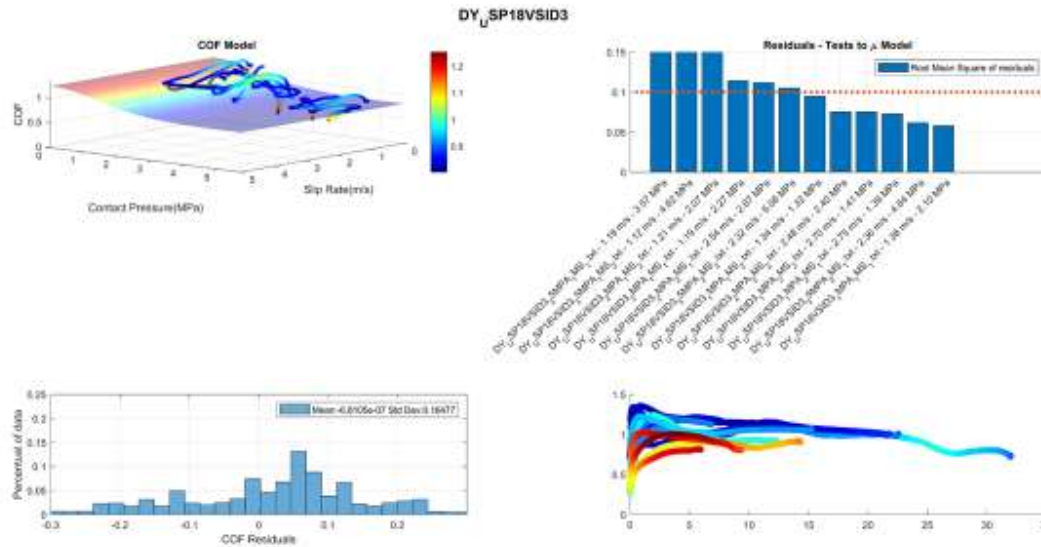
Blue Neouperen (USP-18) vs. dummy flesh (ID3)



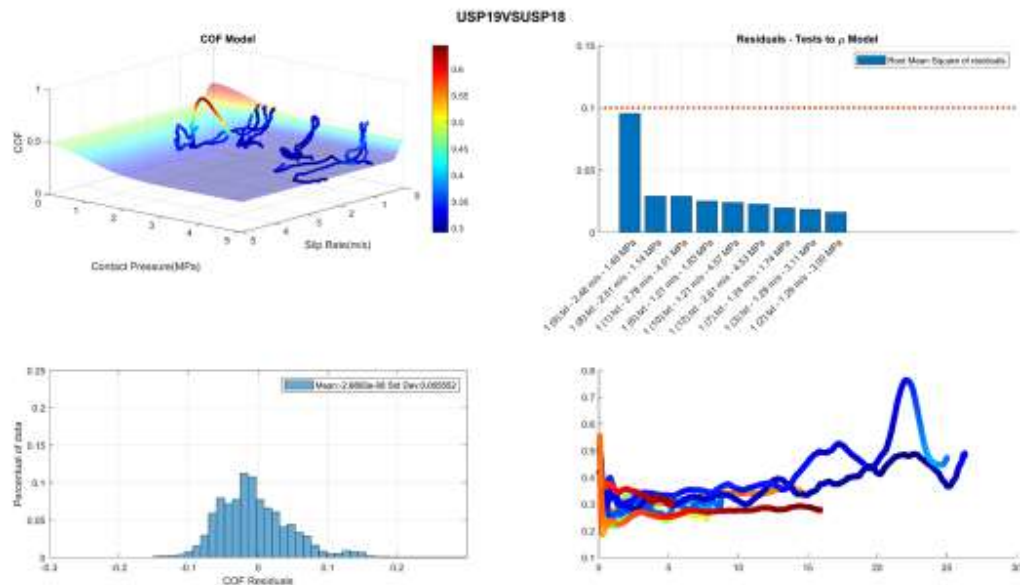
44

Results

Blue Neouperen (USP-18) vs. dummy flesh (ID3)

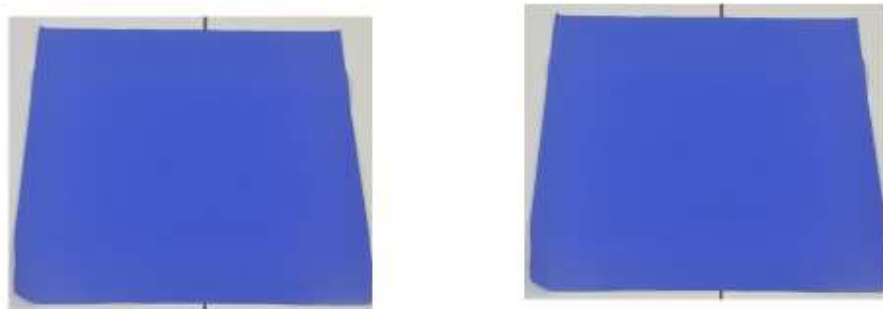


45



Results

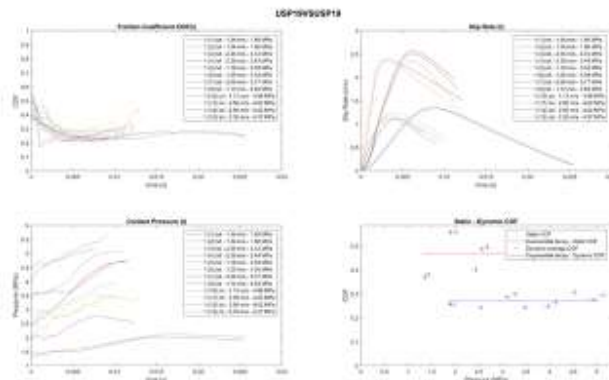
Blue Gordura (USP-19) vs. Blue Neouperen(USP-19)



47

Results

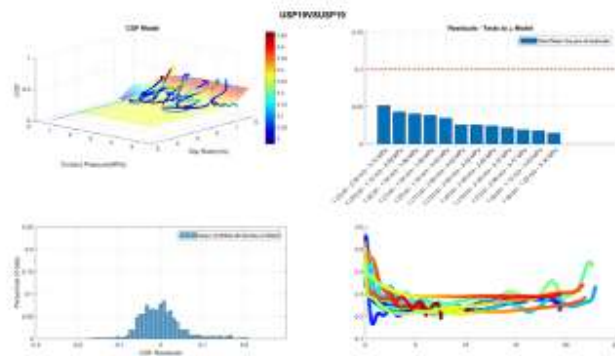
Blue Gordura (USP-19) vs. Blue Gordura (USP-19)



48

Results

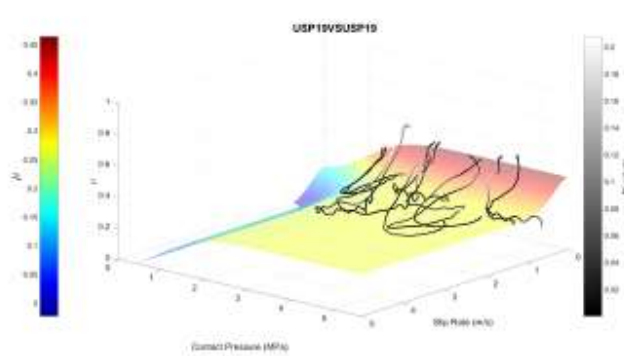
Blue Gordura (USP-19) vs. Blue Gordura (USP-19)



49

Results

Blue Gordura (USP-19) vs. Blue Gordura (USP-19)



$$COF = A + Be^{(-Gv^M)} + Ce^{(-Hv^N)}$$

COEFFICIENTS:

$$A = 0.26949$$

$$B = 0.19468$$

$$C = -0.29242$$

$$G = 2.0056$$

$$H = 0.76884$$

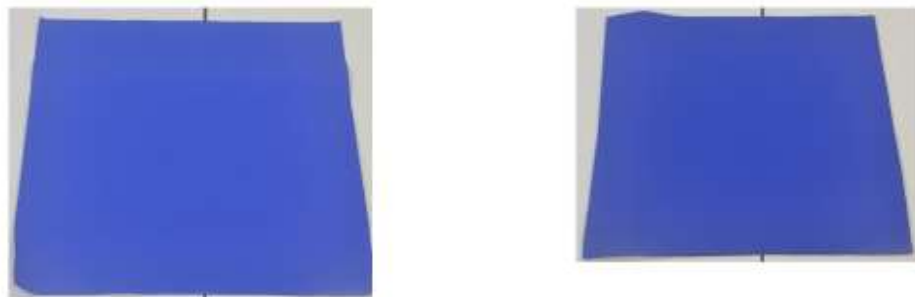
$$M = 1.7457$$

$$N = 2$$

50

Results

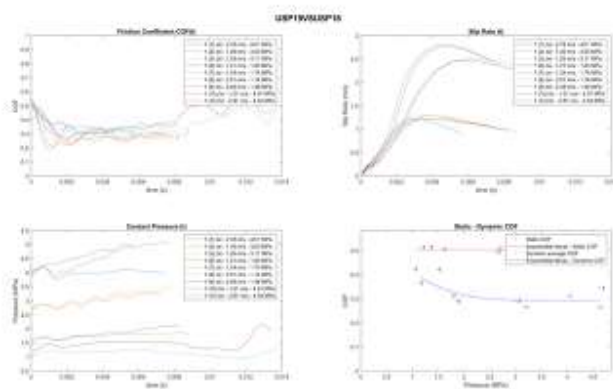
Blue Gordura (USP-19) vs. Blue Neouperen(USP-18)



31

Results

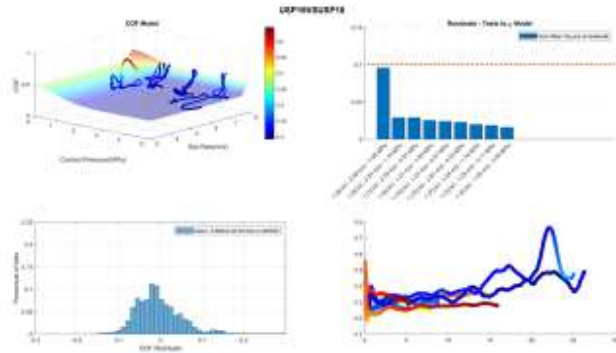
Blue Gordura (USP-19) vs. Blue Neouperen (USP-18)



32

Results

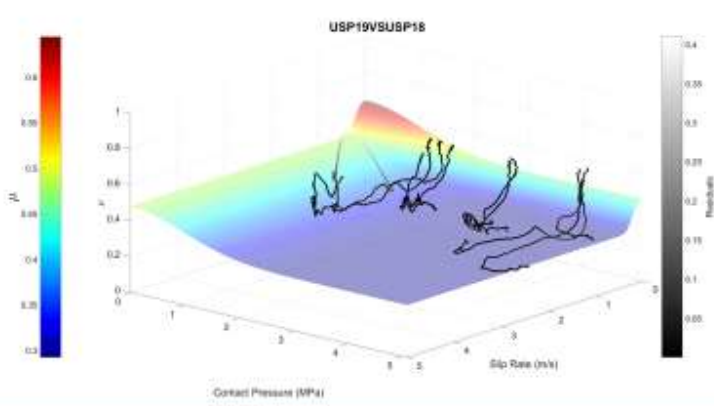
Blue Gordura (USP-19) vs. Blue Neouperen (USP-18)



53

Results

Blue Gordura (USP-19) vs. Blue Neouperen (USP-18)



$$COF = A + Be^{(-Gv^M)} + Ce^{(-Hv^N)}$$

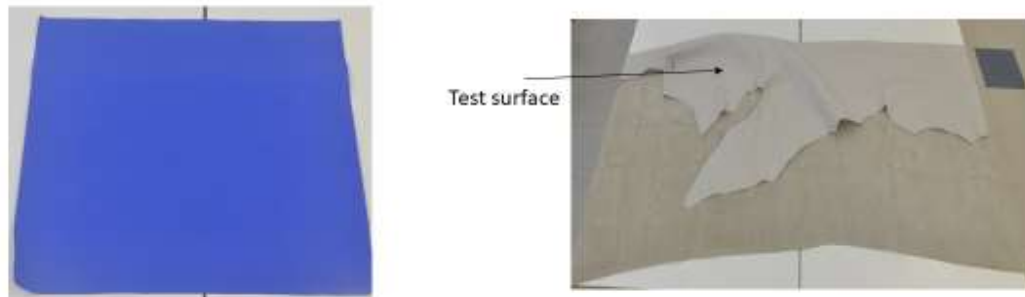
Coefficients:

A = 0.29226
B = 0.16387
C = 0.18844
G = 3.733
H = 0.72241
M = 2.8841
N = 2

54

Results

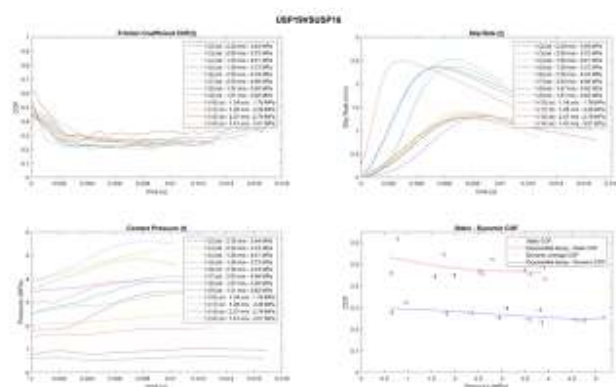
Blue Gordura (USP-19) vs. seat textile/leather - Leder unkaschiert (USP-16)



55

Results

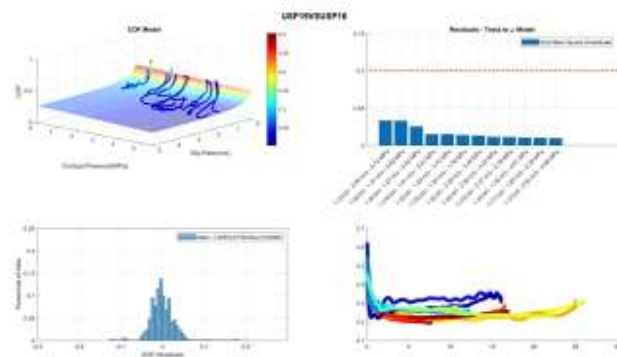
Blue Gordura (USP-19) vs. seat textile/leather - Leder unkaschiert (USP-16)



56

Results

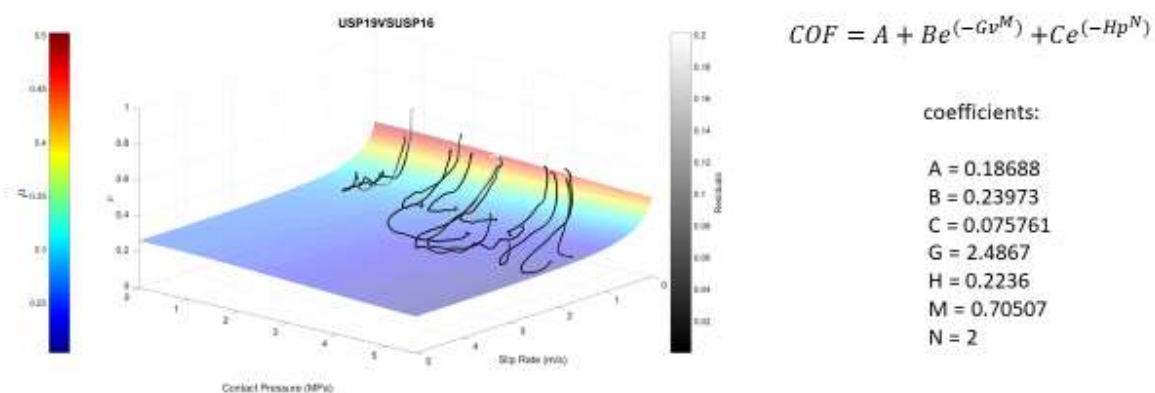
Blue Gordura (USP-19) vs. seat textile/leather - Leder unkaschiert (USP-16)



37

Results

Blue Gordura (USP-19) vs. seat textile/leather - Leder unkaschiert (USP-16)



38

Results

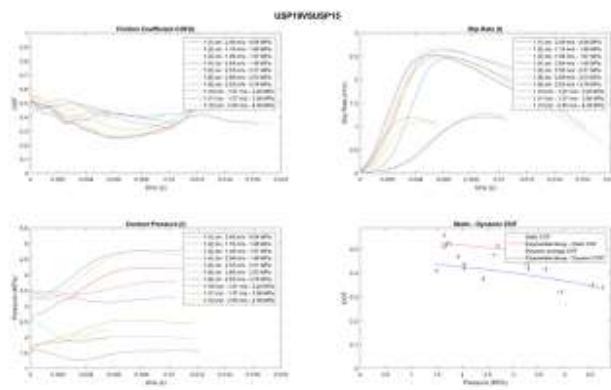
Blue Gordura(USP-19) vs. seat textile/leather - Stoff-Schaum-Kaschier (USP-15)



38

Results

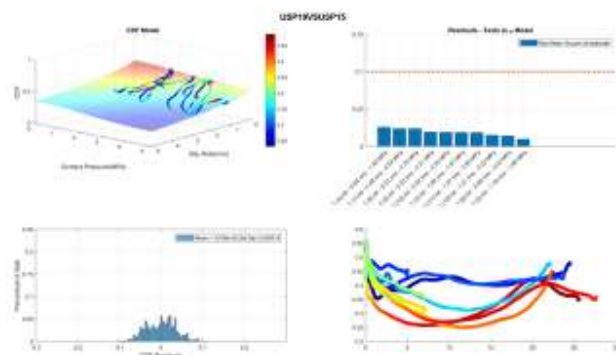
Blue Gordura (USP-19) vs. seat textile/leather - Stoff-Schaum-Kaschier (USP-15)



60

Results

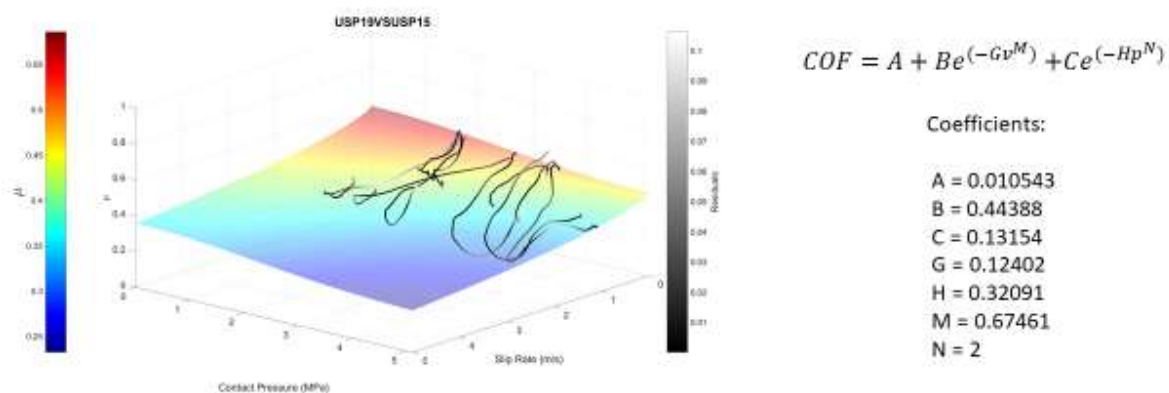
Blue Gordura (USP-19) vs. seat textile/leather - Stoff-Schaum-Kaschier (USP-15)



61

Results

Blue Gordura (USP-19) vs. seat textile/leather - Stoff-Schaum-Kaschier (USP-15)



62

Results

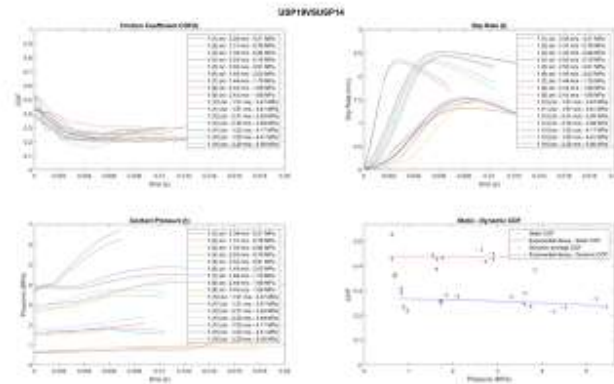
Blue Gordura (USP-19) vs. seat textile/leather - Veganza mit Vlies (USP-14)



63

Results

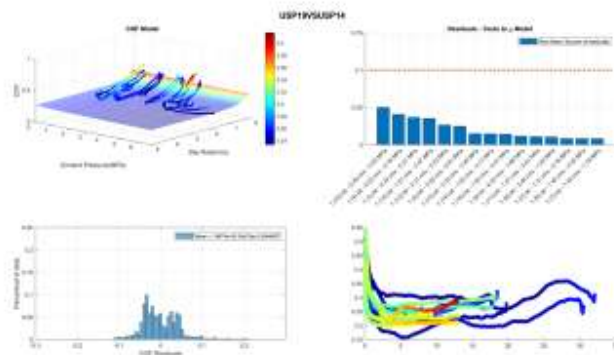
Blue Gordura (USP-19) vs. seat textile/leather - Veganza mit Vlies (USP-14)



64

Results

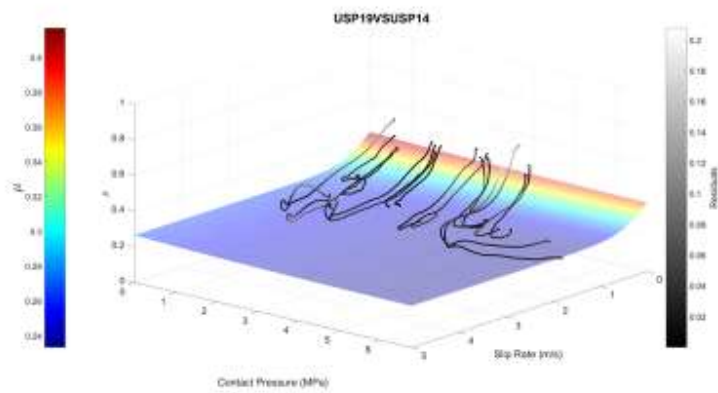
Blue Gordura (USP-19) vs. seat textile/leather - Veganza mit Vlies (USP-14)



65

Results

Blue Gordura (USP-19) vs. seat textile/leather - Veganza mit Vlies (USP-14)



$$COF = A + Be^{(-Gv^M)} + Ce^{(-Hv^N)}$$

Coefficients:

A = 0.227
B = 0.15076
C = 0.039208
G = 2.2086
H = 0.26889
M = 1.2283
N = 1

66

Results

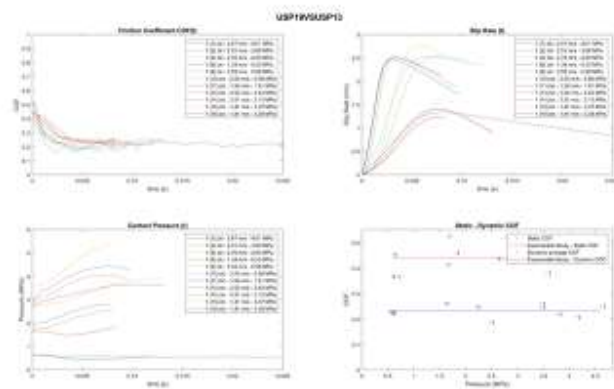
Blue Gordura (USP-19) vs. seat textile/leather – Alcantara (USP-13)



67

Results

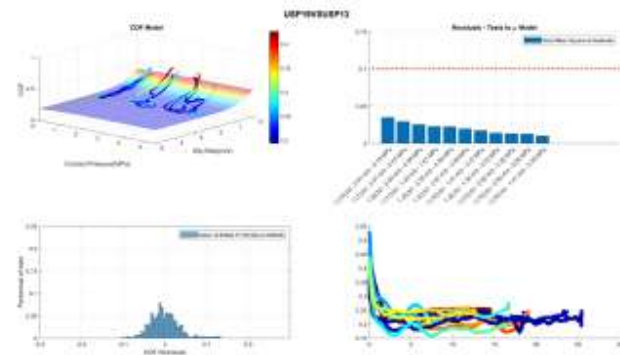
Blue Gordura (USP-19) vs. seat textile/leather – Alcantara (USP-13)



68

Results

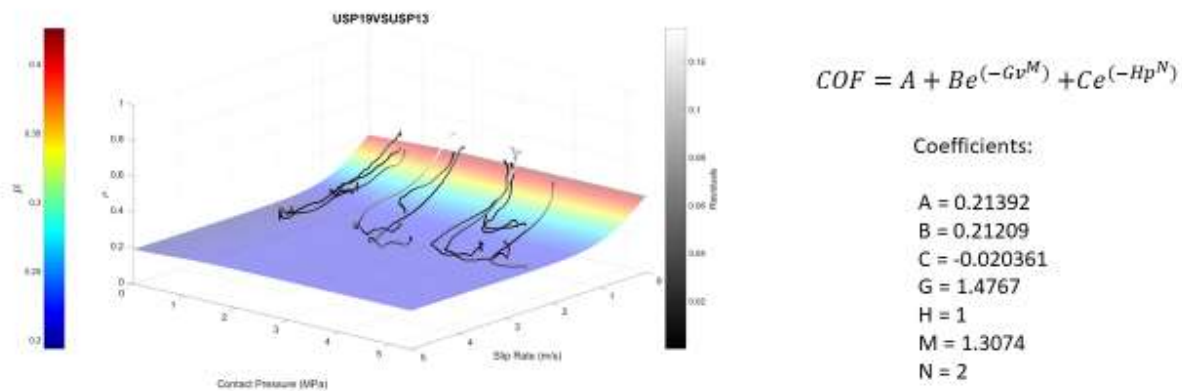
Blue Gordura (USP-19) vs. seat textile/leather – Alcantara (USP-13)



68

Results

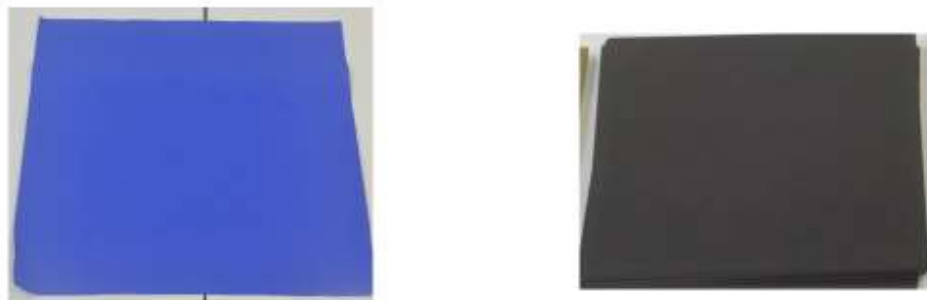
Blue Gordura (USP-19) vs. seat textile/leather – Alcantara (USP-13)



70

Results

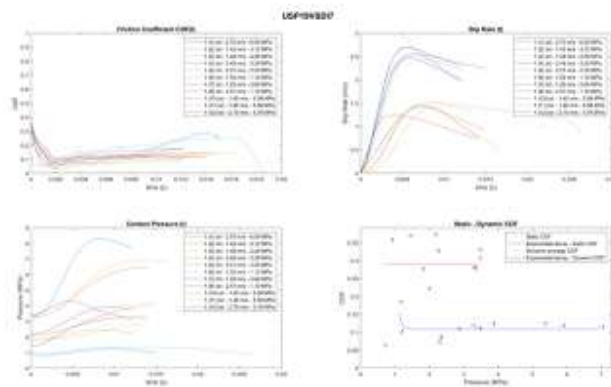
Blue Gordura (USP-19) vs. dummy flesh (ID7)



71

Results

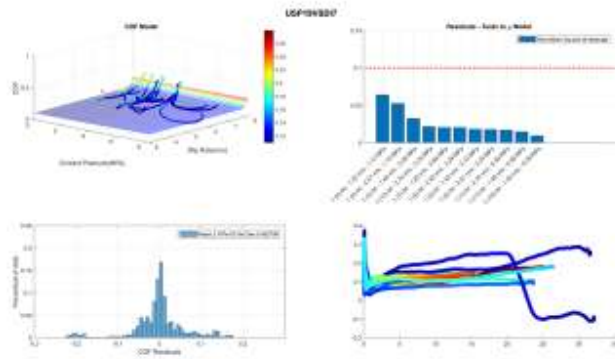
Blue Gordura (USP-19) vs. dummy flesh (ID7)



72

Results

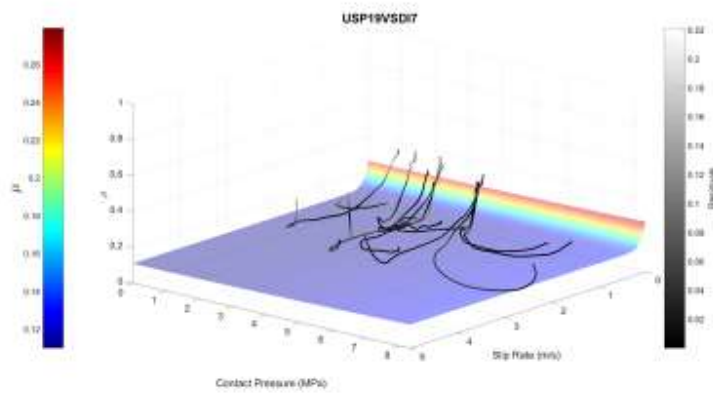
Blue Gordura (USP-19) vs. dummy flesh (ID7)



73

Results

Blue Gordura (USP-19) vs. dummy flesh (ID7)



$$COF = A + Be^{(-Gv^M)} + Ce^{(-Hv^N)}$$

Coefficients:

$A = 0.1953$
 $B = 0.14701$
 $C = -0.085356$
 $G = 9.576$
 $H = 0.066398$
 $M = 1.1406$
 $N = 1.9997$

74

Results

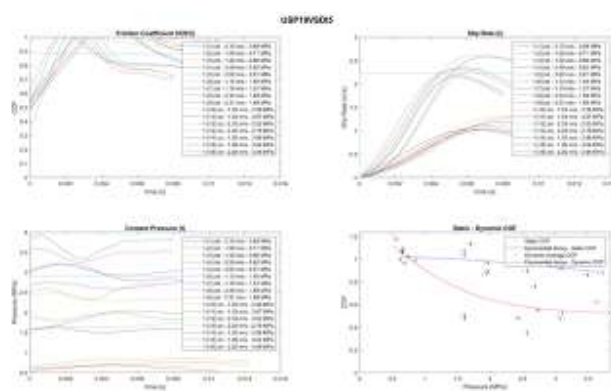
Blue Gordura (USP-19) vs. dummy flesh (ID5)



25

Results

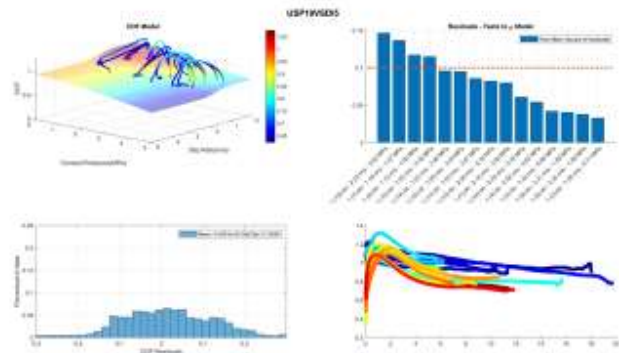
Blue Gordura (USP-19) vs. dummy flesh (ID5)



26

Results

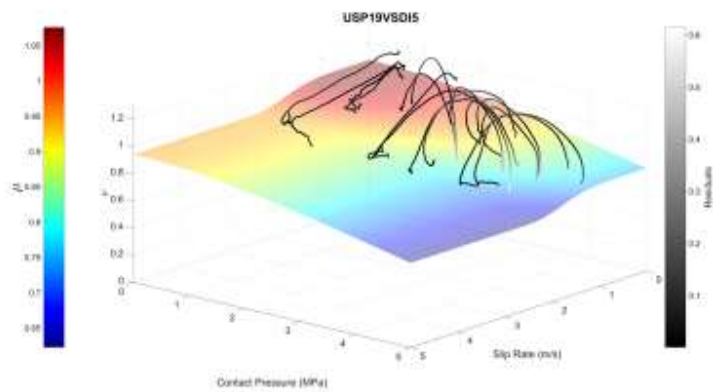
Blue Gordura (USP-19) vs. dummy flesh (ID5)



77

Results

Blue Gordura (USP-19) vs. dummy flesh (ID5)



$$COF = A + Be^{(-Gv^M)} + Ce^{(-Hv^N)}$$

Coefficients:

$$\begin{aligned} A &= 0.034623 \\ B &= 0.13319 \\ C &= 0.90797 \\ G &= 0.53613 \\ H &= 0.12441 \\ M &= 5 \\ N &= 1.7539 \end{aligned}$$

78

Results

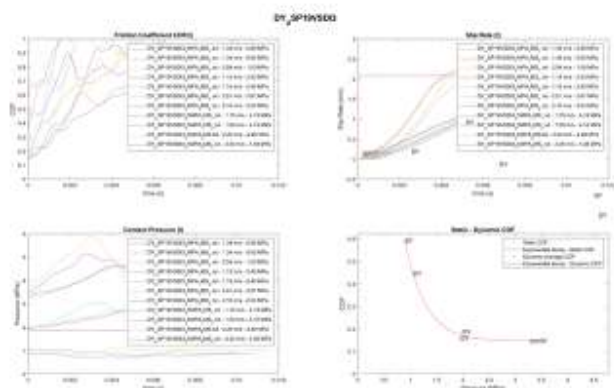
Blue Gordura (USP-19) vs. dummy flesh (ID3)



79

Results

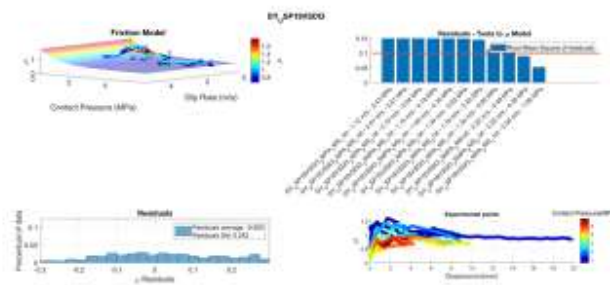
Blue Gordura (USP-19) vs. dummy flesh (ID3)



80

Results

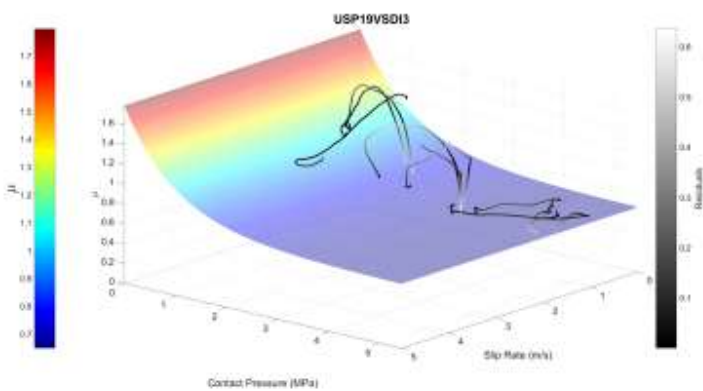
Blue Gordura (USP-19) vs. dummy flesh (ID3)



81

Results

Blue Gordura (USP-19) vs. dummy flesh (ID3)



$$COF = A + Be^{(-Gv^M)} + Ce^{(-Hv^N)}$$

Coefficients:

$$A = 0.64006$$

$$B = 0.01$$

$$C = 1.1467$$

$$G = 0.05$$

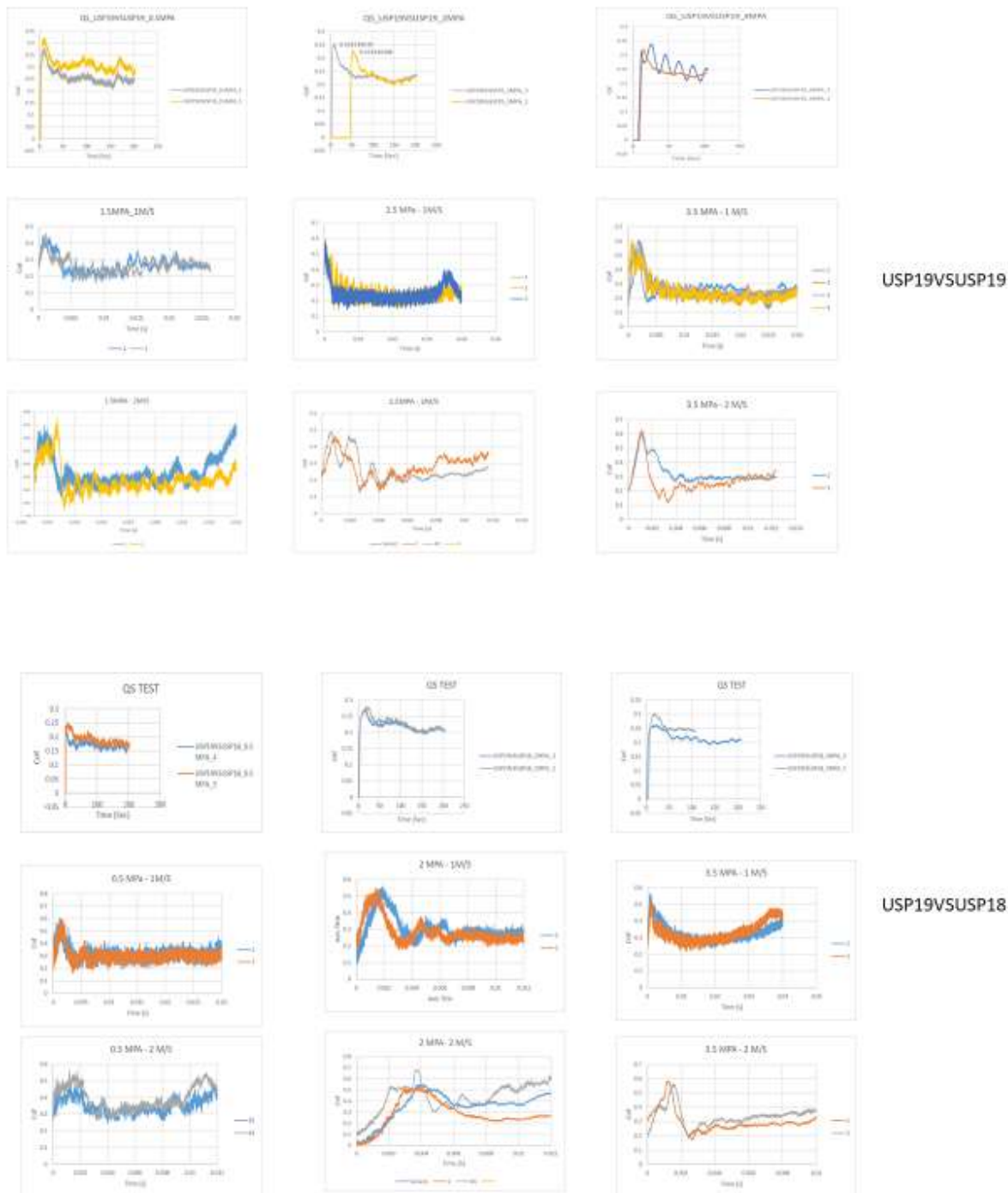
$$H = 1$$

$$M = 0.05$$

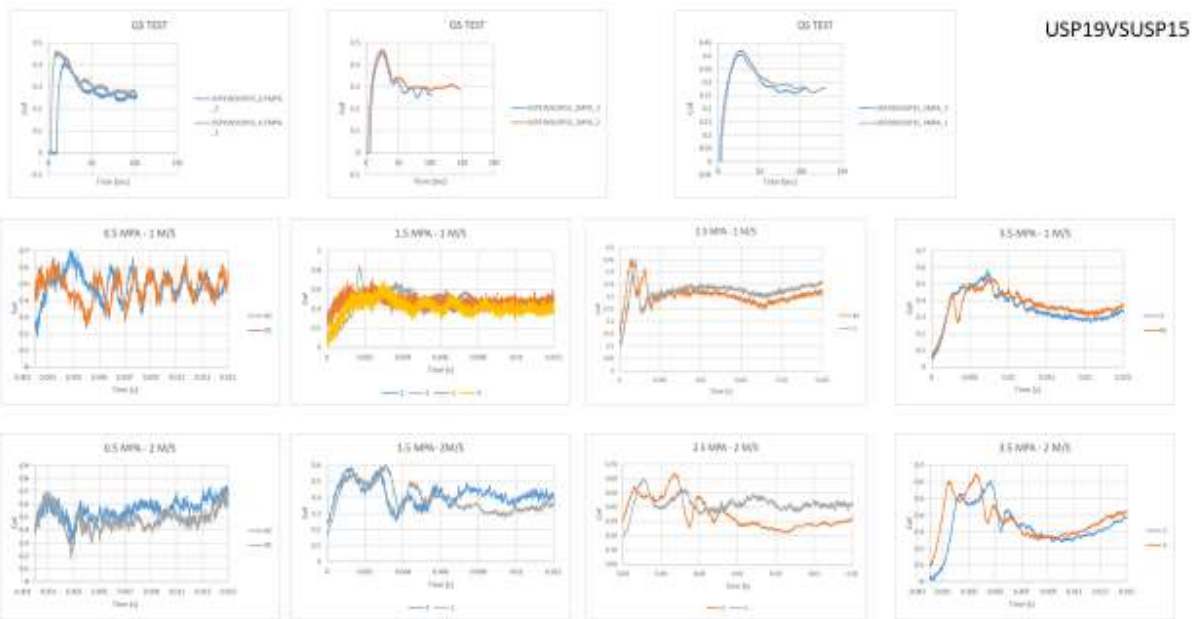
$$N = 1$$

82

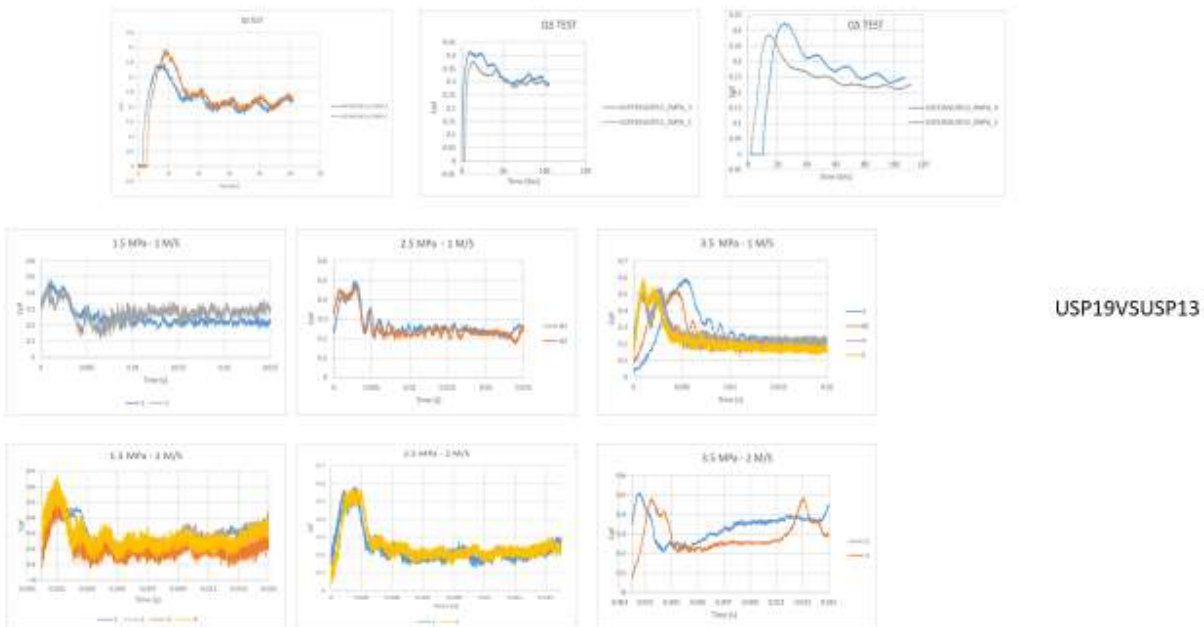
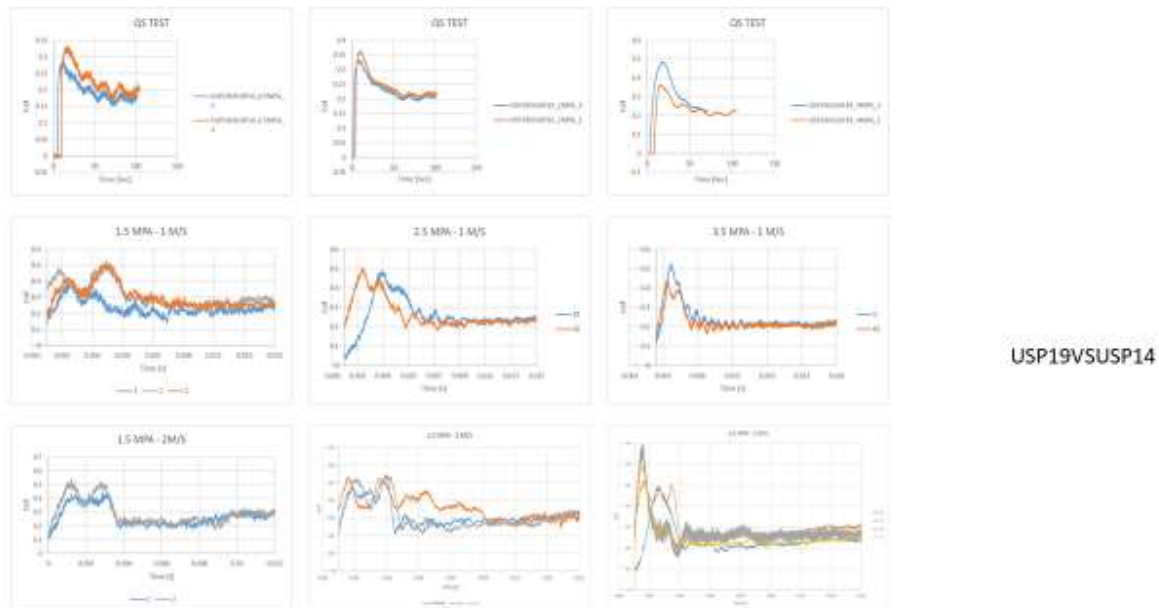
Raw data (friction tests, quasi-static and dynamic at different contact pressures)



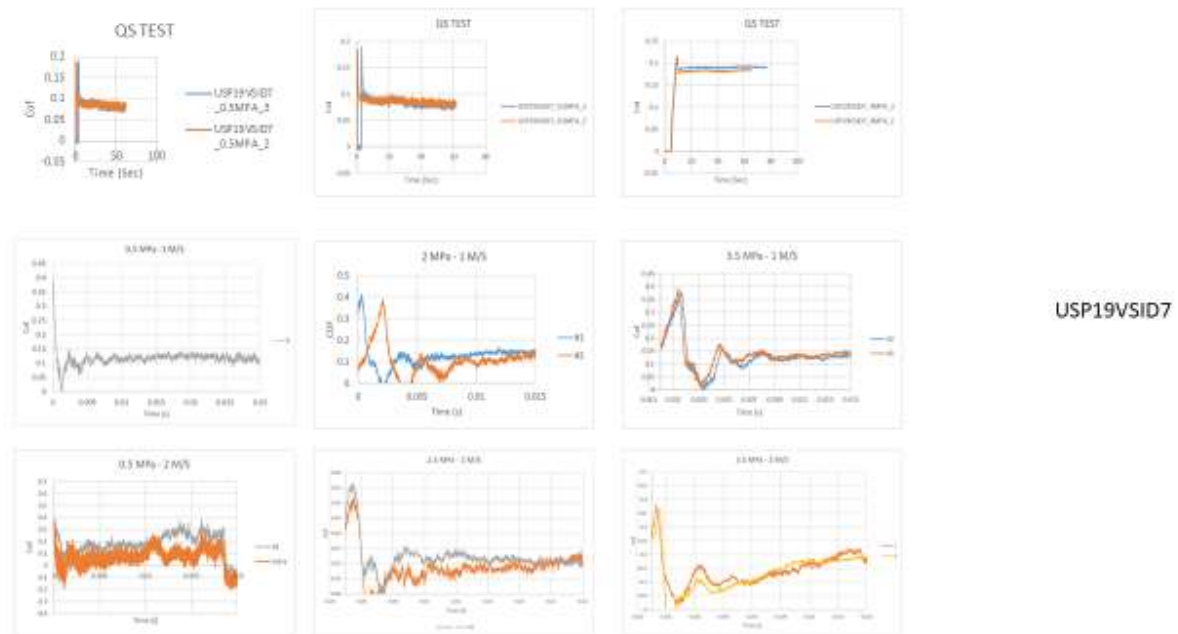
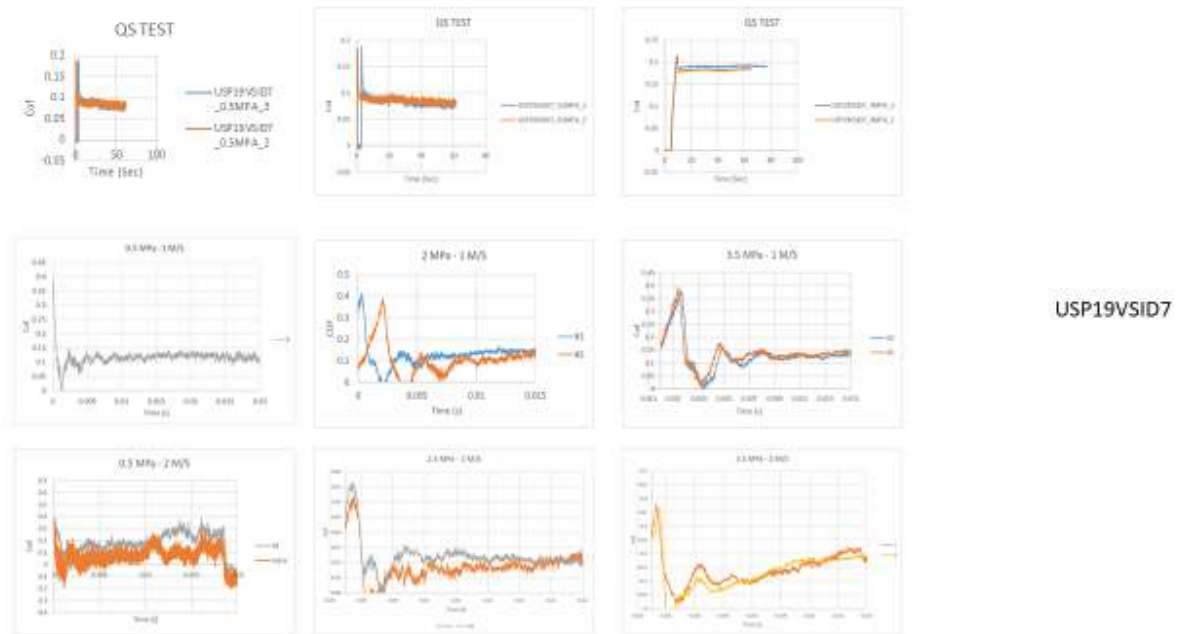
Raw data (friction tests, quasi-static and dynamic at different contact pressures)



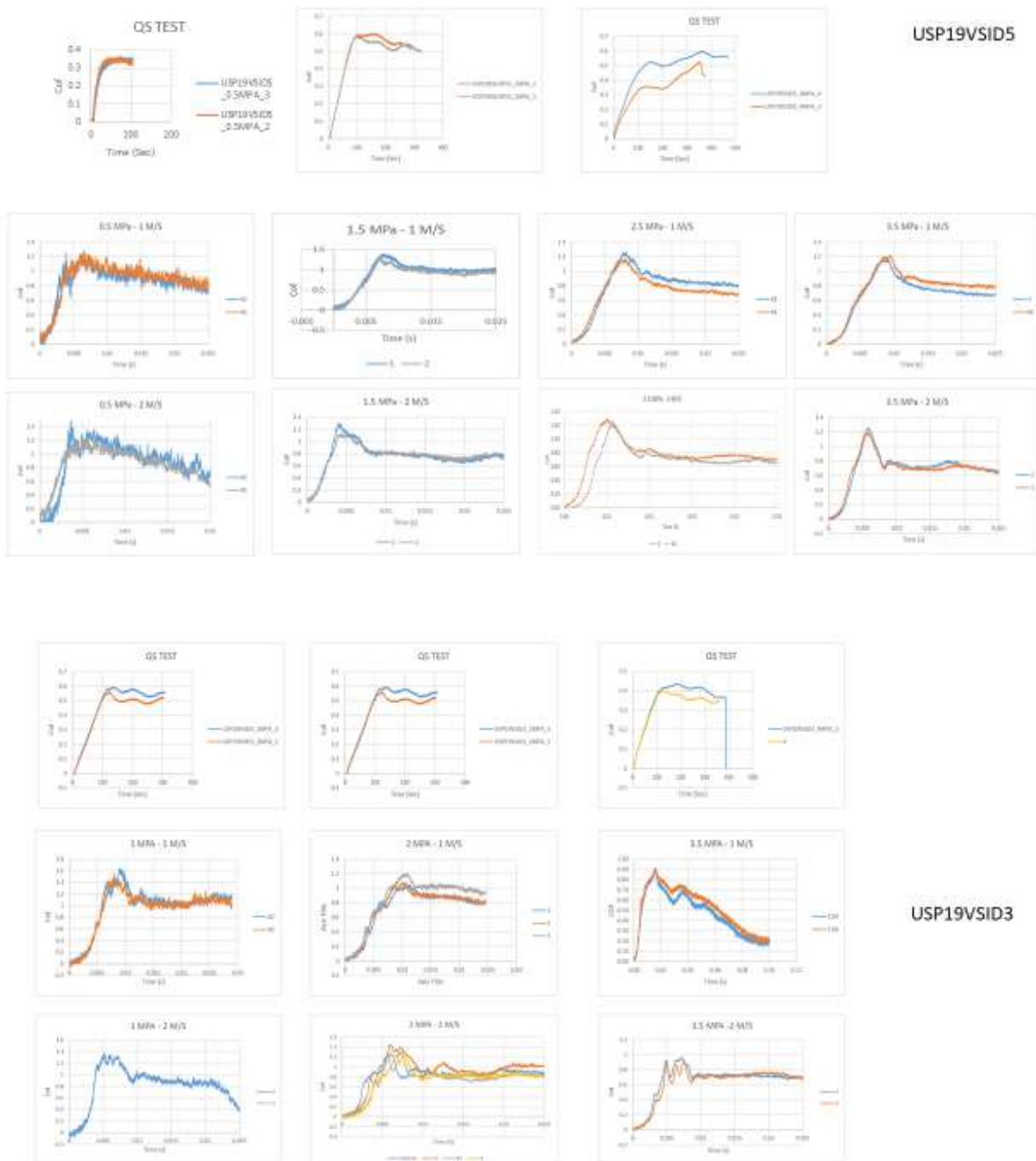
Raw data (friction tests, quasi-static and dynamic at different contact pressures)



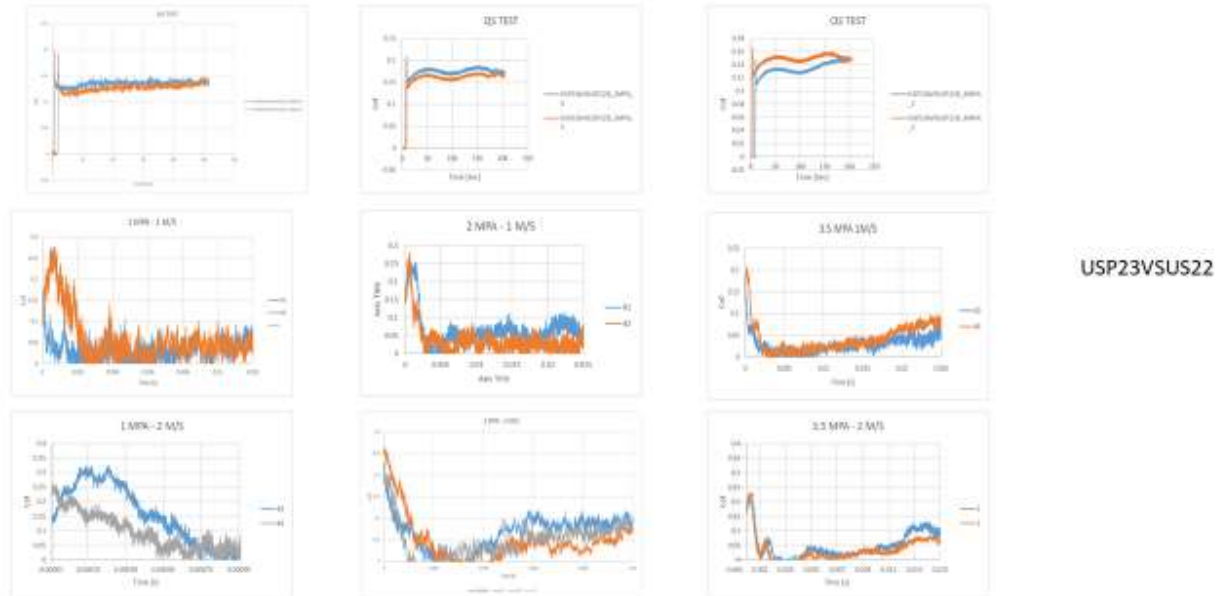
Raw data (friction tests, quasi-static and dynamic at different contact pressures)



Raw data (friction tests, quasi-static and dynamic at different contact pressures)



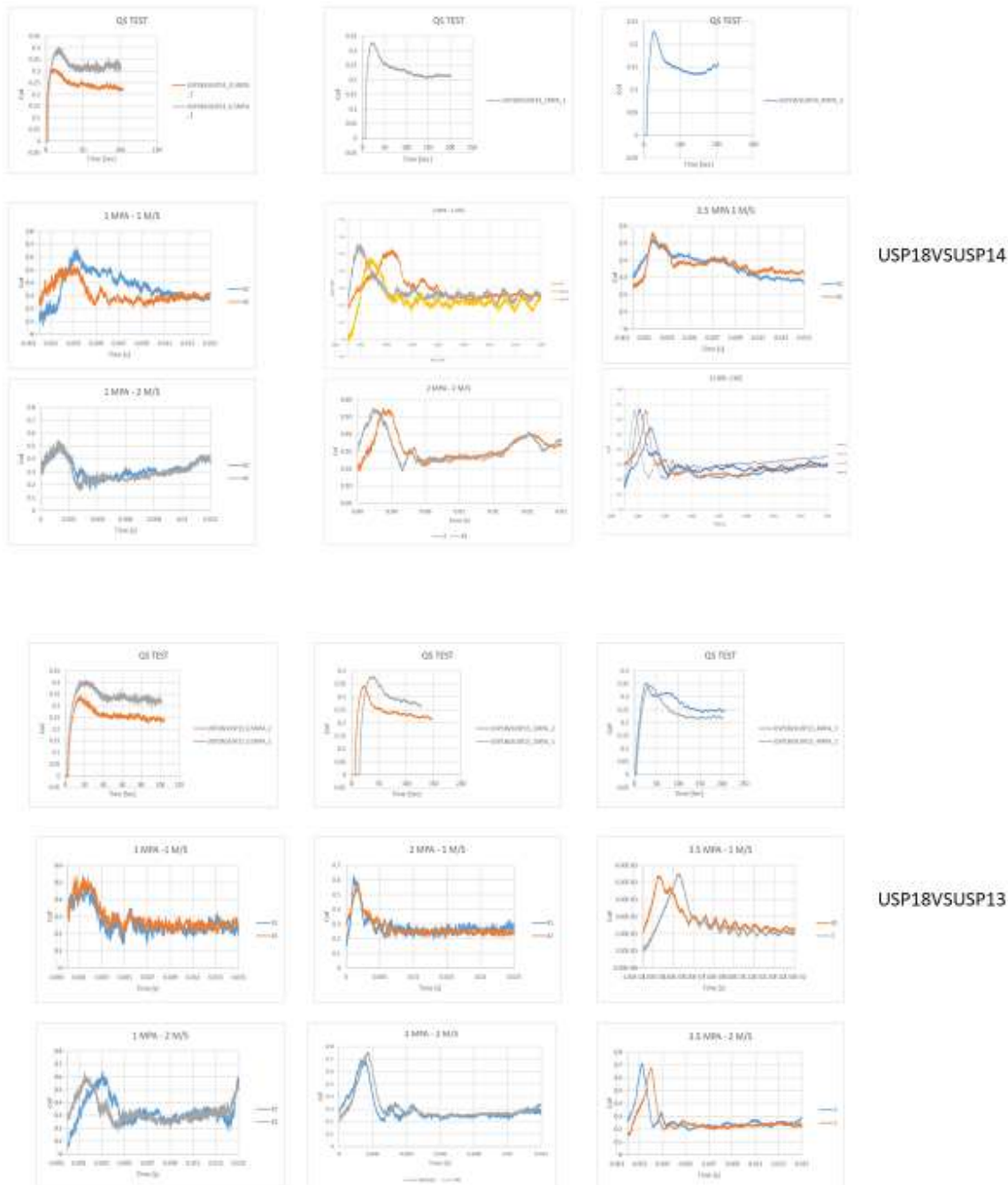
Raw data (friction tests, quasi-static and dynamic at different contact pressures)



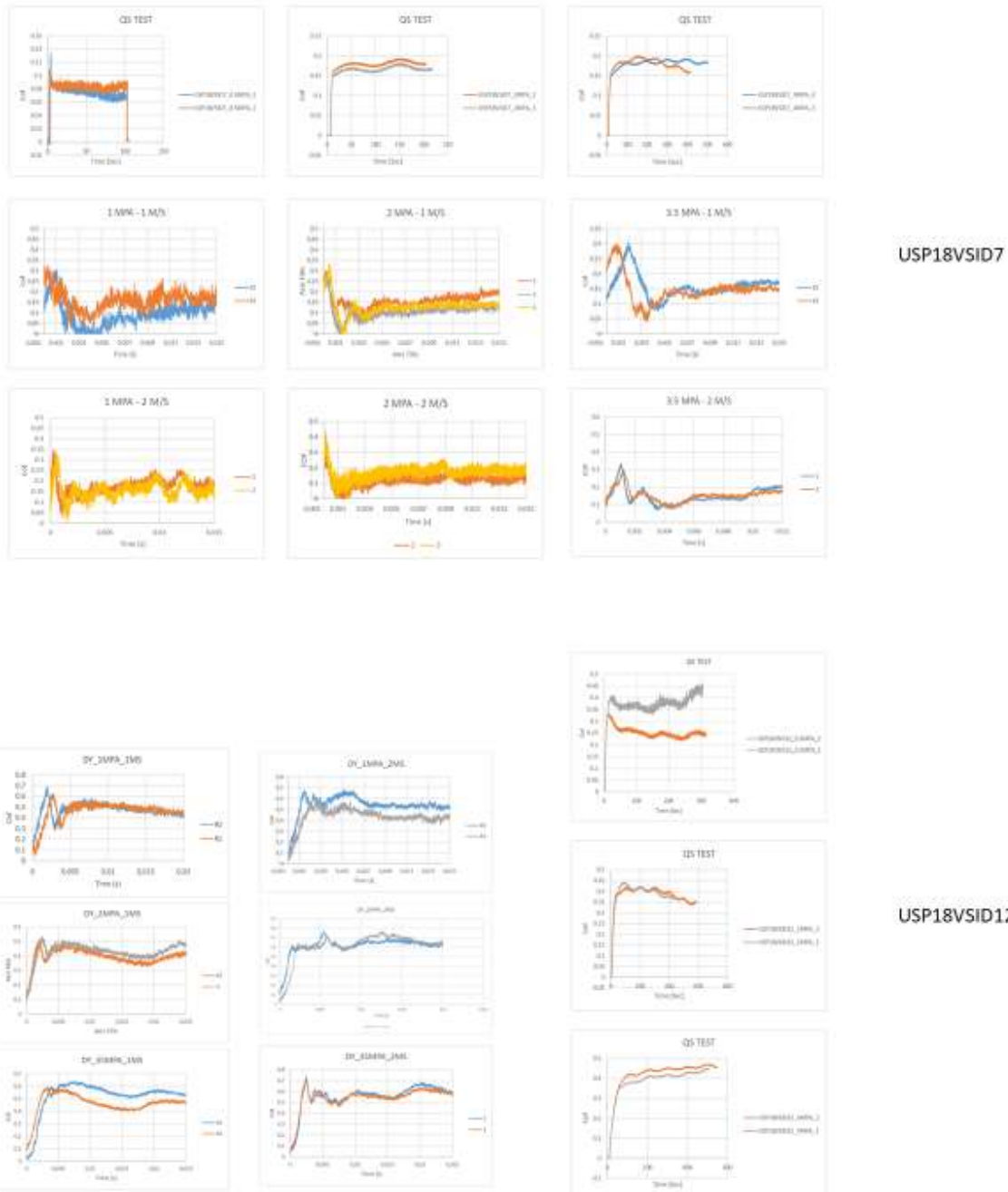
Raw data (friction tests, quasi-static and dynamic at different contact pressures)



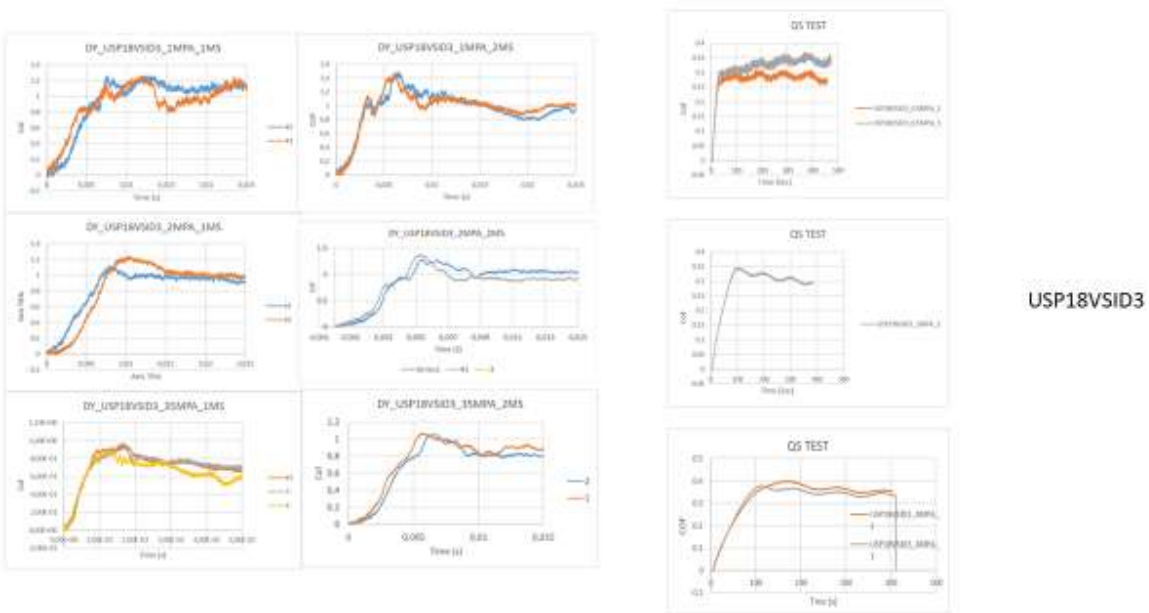
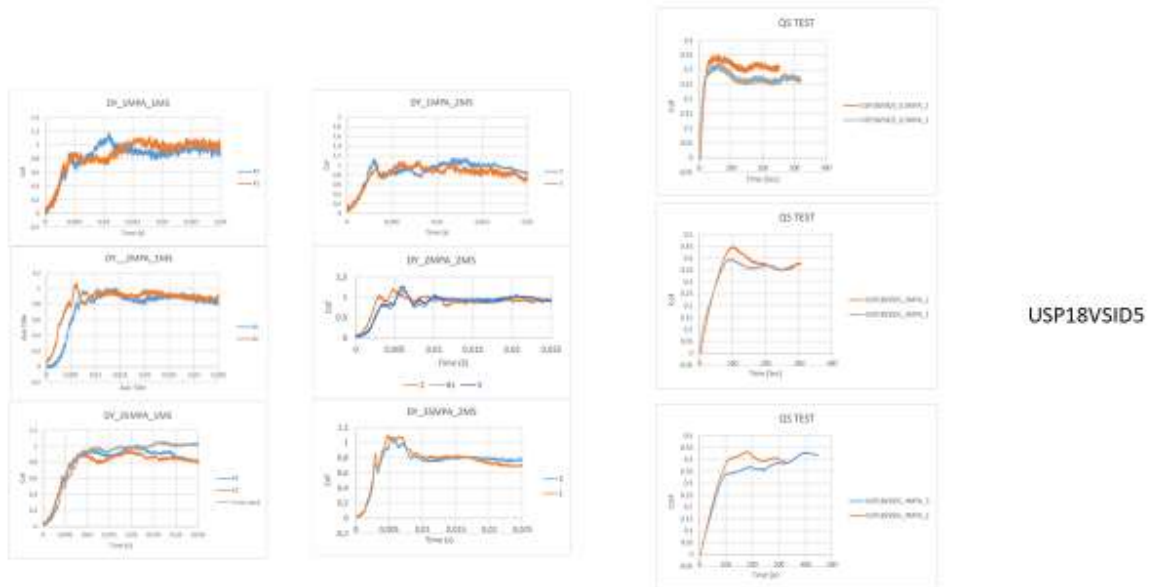
Raw data (friction tests, quasi-static and dynamic at different contact pressures)



Raw data (friction tests, quasi-static and dynamic at different contact pressures)



Raw data (friction tests, quasi-static and dynamic at different contact pressures)



Part 3

Material characterization and axial crushing tests on steel tubes

Conducted by

Matheus Oliveira, Pouria. B. Ataabadi

Supervised by

Prof. Dr. Marcilio Alves

Feb. 2024

Contents

Abstract.....	116
1. Johnson-Cook (JC) plasticity model	116
1.1 Finding parameters A , B , and n	117
1.2 Finding strain rate hardening parameter (C)	117
2. Experimental tests and specimens.....	117
2.1 Experimental tests: Tensile tests at quasi-static strain rate region	118
2.2 Experimental tests: Tensile tests at the higher strain rates.....	121
2.2.1 Experimental tests: Tensile tests at intermediate strain rate region	121
2.2.2 Experimental tests: Tensile tests at high strain rate region (SHTB tests)	123
2.2.3 Evaluating strain rate sensitivity parameter, C	126
2.3 Axial impact on tubular steel components	127
3. Summary	132
References.....	132

Abstract

The document herein presents the material characterization conducted at the GMSIE-USP laboratory on steel tubes provided by IPT. Quasi-static tensile tests and high strain rate tensile tests utilizing the Split Hopkinson Tension Bar (SHTB) apparatus were conducted to determine the parameters of the Johnson-Cook plasticity model. In addition to the material characterization, axial impact tests were performed on tubular components using a drop hammer rig. The findings from these impact tests could be employed to verify the crashworthiness parameters of the material and calibrate finite element (FE) models.

1. Johnson-Cook (JC) plasticity model

The Johnson-Cook (JC) plasticity model is a widely used constitutive model in material science and engineering, particularly in the field of computational mechanics. It describes the mechanical behavior of materials, particularly metals, under high strain rates, elevated temperatures, and large plastic deformations. The JC plasticity model represents flow stress as a function of strain hardening, rate dependency, and temperature dependency as expressed by Eq. 1. In Eq.1 the effective stress, σ_0 , is expressed as a function of effective plastic strain, $\bar{\varepsilon}^{pl}$, nondimensional plastic strain rate $\dot{\bar{\varepsilon}}^* = (\frac{\dot{\varepsilon}^{pl}}{\dot{\varepsilon}_0})$, and a nondimensional temperature, $\hat{\theta}$ by using material parameters, A, B, n, C, and m (Dassault Systèmes Simulia, 2014).

$$\sigma_0 = (A + B(\bar{\varepsilon}^{pl})^n(1 + C\ln(\dot{\bar{\varepsilon}}^*)(1 - \hat{\theta}^m)) \quad (\text{Eq.1})$$

Parameter A represents the initial yield strength of the material at the quasi-static strain rate. Parameters B and n denote the flow stress on strain hardening behavior at the quasi-static strain rate. Parameter C signifies the strain rate hardening effect. The thermal softening effect, represented by parameter m, is disregarded in this context, hence m is set to zero. Consequently, after eliminating the thermal softening effect, the third term is removed, and Eq. 1 is expressed as follows.

$$\sigma_0 = (A + B(\bar{\varepsilon}^{pl})^n(1 + C \ln(\dot{\bar{\varepsilon}}^*)) \quad (\text{Eq.2})$$

1.1 Finding parameters A, B, and n

The initial yield strength (A) can be determined from quasi-static tensile tests using a suitable method such as the 0.2% offset method. Hardening parameters (B, n) can be obtained through curve fitting methods, taking into account tests conducted at a reference strain rate (quasi-static). Simplifying Eq. 2 by considering tests at the reference strain rate yields the following expression.

$$\sigma_0 - A = B\bar{\varepsilon}^{pl^n} \quad (\text{Eq.3})$$

By using a suitable curve fitting method, strain hardening parameters can be calibrated from quasi-static tensile test results. Parameters B and n can be calculated from the slope of log (Plastic Stress) Vs log (Plastic Strain) from the quasi-static test data (see Eq.4).

$$\ln(\sigma_0 - A) = \ln B + n \ln \bar{\varepsilon}^{pl} \quad (\text{Eq.4})$$

1.2 Finding strain rate hardening parameter (C)

The strain rate sensitivity constant, C, can be estimated by analyzing a group of parallel straight lines for different strains, using the slope of Eq. 5. To approximate the value of C, tensile tests at higher strain rates than those of quasi-static tests need to be conducted. In this report, several tensile tests at three different strain rate regions (quasi-static, intermediate, and high strain rates) were considered for the evaluation of the C parameter.

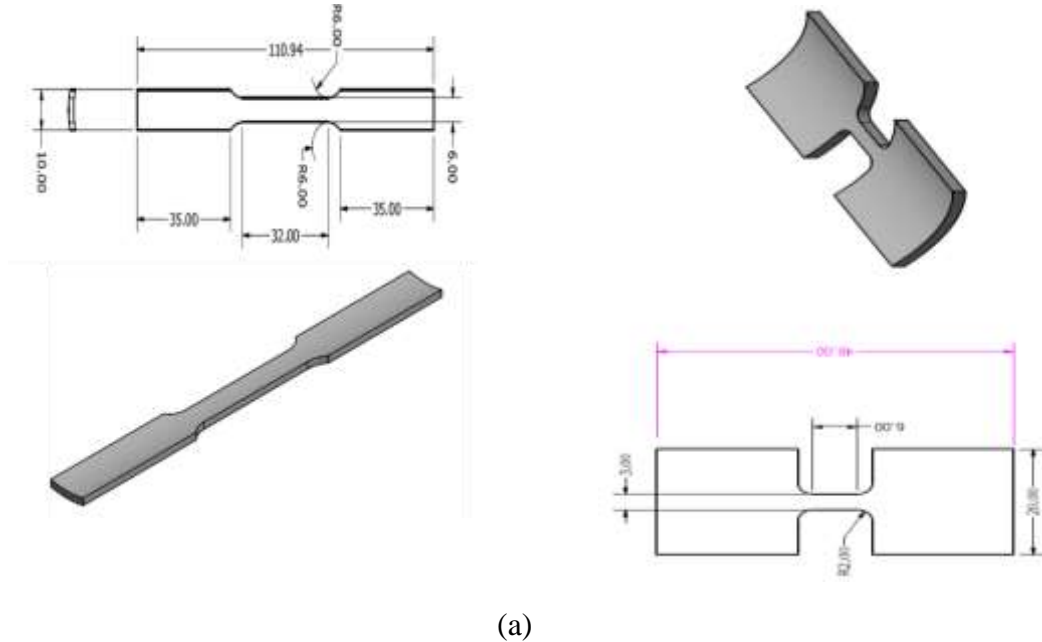
$$\frac{\sigma}{A + B\bar{\varepsilon}^{pl^n}} = 1 + C \ln(\dot{\bar{\varepsilon}}^*) \quad (\text{Eq.5})$$

2. Experimental tests and specimens

2.1 Experimental tests: Tensile tests at quasi-static strain rate region

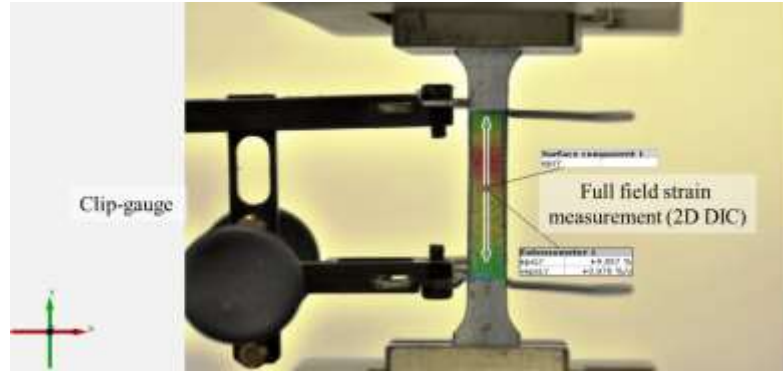
Quasi-static tensile tests were conducted utilizing the Instron 3369 universal testing machine equipped with a 50 kN load cell. The crosshead velocity was set at 1 mm/min for all quasi-static tests. The axial tensile strain was measured using a clip-gauge with a 25 mm initial gauge length, complemented by a 2D digital image correlation (DIC) measurement system³. For the quasi-static tensile test, the nominal strain rate is ~ 0.0007 1/s.

Quasi-static tensile samples were prepared by cutting them from tubular components following the guidelines outlined in ASTM E8 recommendations. Additionally, a subset of tests was conducted using nonstandard smaller samples with reduced thickness. It is important to note that the results obtained from the small sample tests were not utilized for material characterization; however, they have been included in the complementary Excel file for reference. Figure 1 provides an overview of various aspects of the quasi-static tests, including the configuration of the tensile sample and the strain measurement system.



(a)

³ Three dimensional DIC system was utilized for two extra tensile tests (see complementary Excel file Results.xlsx).



(b)

Fig. 1. Quasi-static tensile tests; (a) Tensile samples and (b) Strain measurement methods (Unit: mm).

Figure 2 presents true stress-strain curves for the three primary quasi-static tests. Table 1 provides details regarding the elastic modulus, yield strength, ultimate tensile strength, and fracture strain.

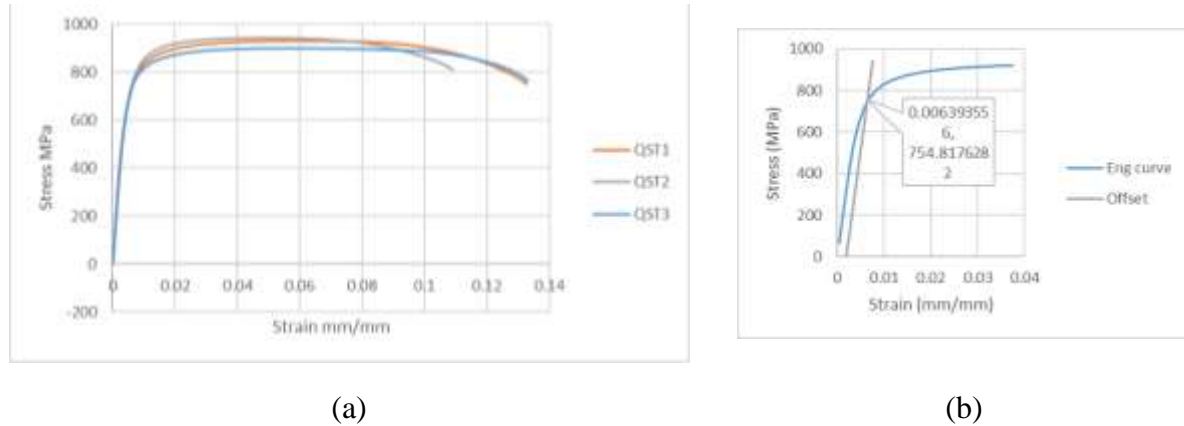


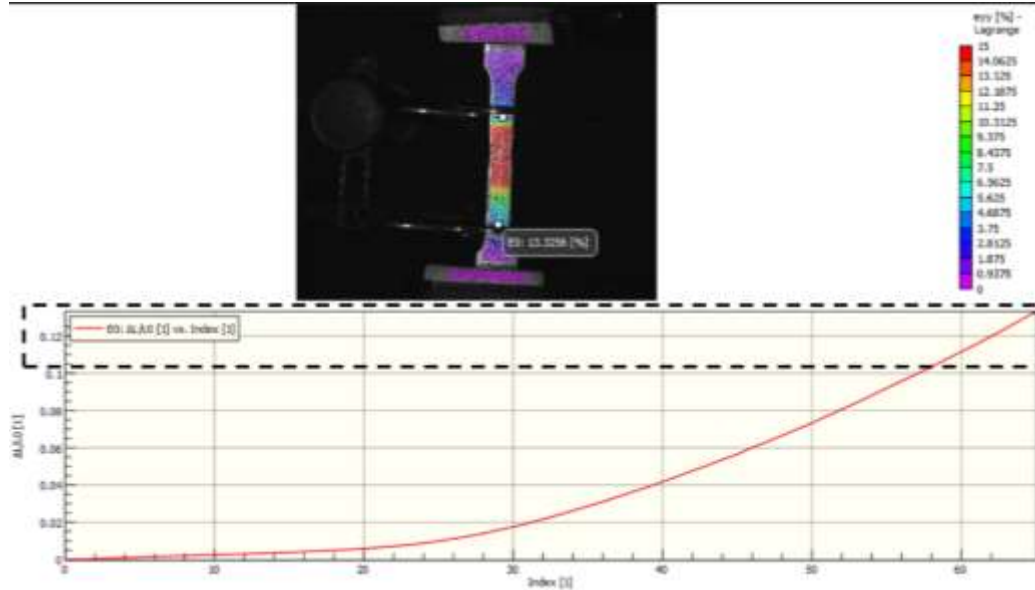
Fig. 2. Results of QS tensile tests; (a) True stress-strain curves for three quasi-static tensile tests and (b) Estimating yield strength using offset method (QST1).

Table 1. Quasi-static test results.

Test ID	Elastic modulus (GPa)	Yield stress (MPa)	UTS (MPa)	Fracture strain (mm/mm)
QST1	171.80	751.81	1002	0.1246
QST2	186.11	759.72	999	0.103*
QST3	188.00	733.00	974	0.124

Average	181.97	748.17	991	0.1243
---------	--------	--------	-----	--------

* Additional tests proved that the fracture strain of QST2 is unrealistically smaller than the other samples (see the 3D DIC strain measured for an additional test).



The strain-hardening parameters (B , n) of the Johnson-Cook model are depicted in Fig. 3 and summarized in Table 2. The curve-fitting results used to determine these parameters are available in the complementary Excel file.

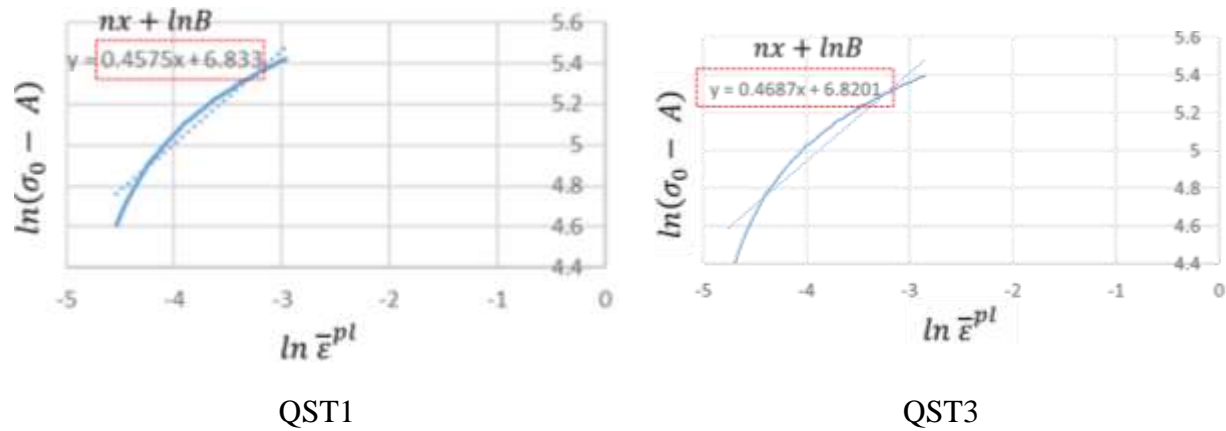


Fig. 3. Calibration of strain hardening parameters, (B and n) for QST1 and QST3.

Table 2. Strain hardening parameters form quasi-static tensile tests.

Test ID	B (MPa)	n
---------	---------	---

QST1	927.97	0.4575
QST2	1035.87	0.4503
QST3	916.07	0.4687
Average	960	0.4589

The plastic stress-strain curves predicted by the JC model ($\sigma_0 = (A + B(\bar{\varepsilon}^{pl})^n)$) are compared to the quasi-static tensile tests in Fig. 4.

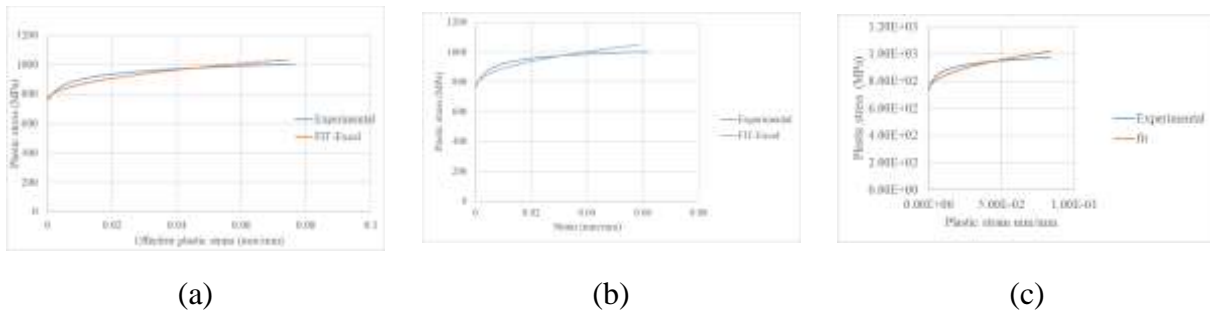


Fig. 4. Prediction of plastic stress-strain at the reference strain rate using the Johnson-Cook (JC) model: (a) QST1, (b) QST2, and (c) QST3.

2.2 Experimental tests: Tensile tests at the higher strain rates

In this section, a description and partial results of tensile tests conducted at higher strain rates are presented. These results were utilized to assess the rate sensitivity of the material, specifically in calculating the C parameter of the Johnson-Cook (JC) model.

2.2.1 Experimental tests: Tensile tests at intermediate strain rate region

For the intermediate strain rate, the sample presented in Fig. 5 underwent tensile loading with a constant cross-head velocity of 8.5 mm/s. Due to the high testing velocity, the deformation of the sample was captured using a Photron high-speed camera (AS5) with a frame rate of 30 kfps, enabling the extraction of tensile strain using GOM software. The dynamic tensile force was

measured using the 9341B Kistler force link at a sampling rate of 30 kHz. For the intermediate tensile test, the nominal strain rate is $\sim 1.2 \text{ 1/s}^4$.

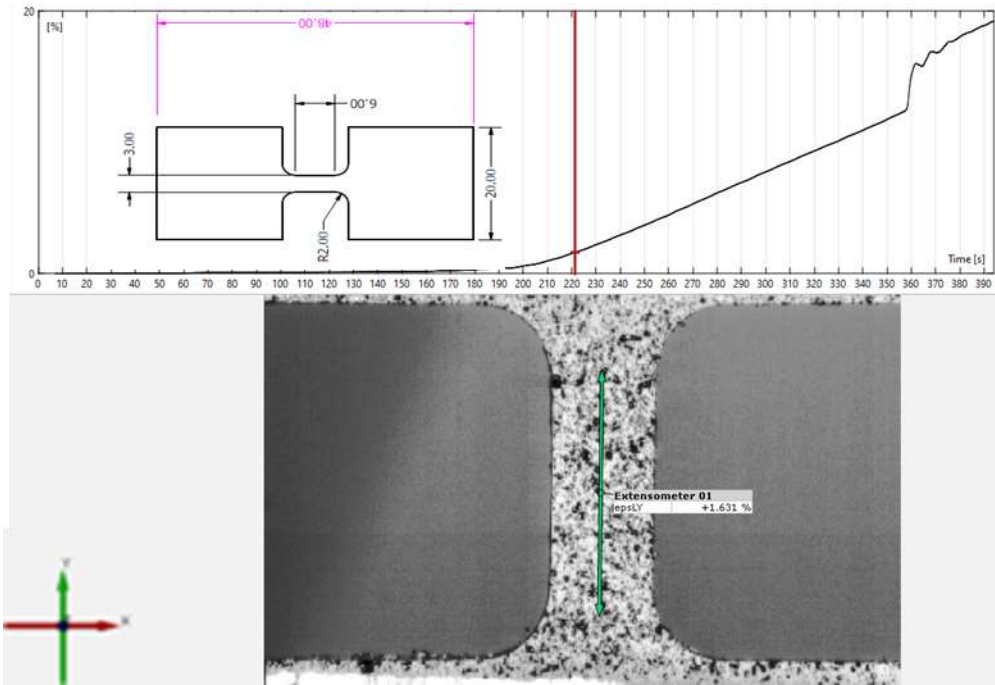


Fig. 5. Intermediate strain rate tensile test (Unit: mm).

True stress-strain curves for the intermediate tensile tests are depicted in Fig. 6 for three specimens. Moreover, Table 3 provides a comprehensive listing of the results obtained from the intermediate tensile tests.

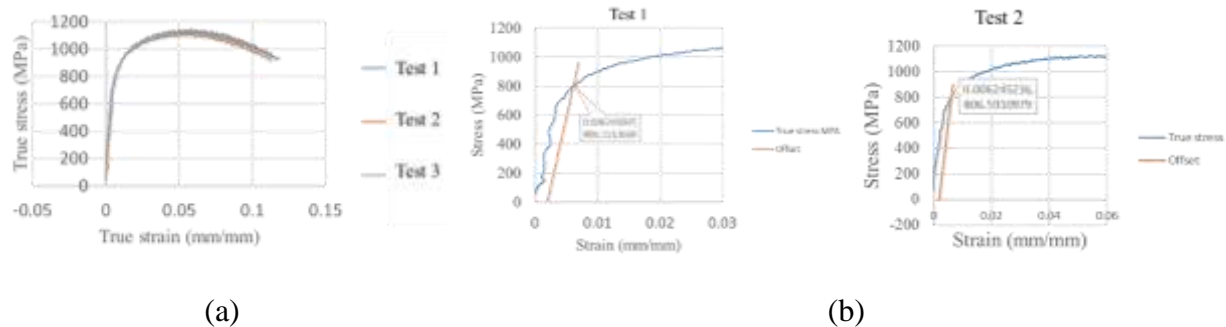


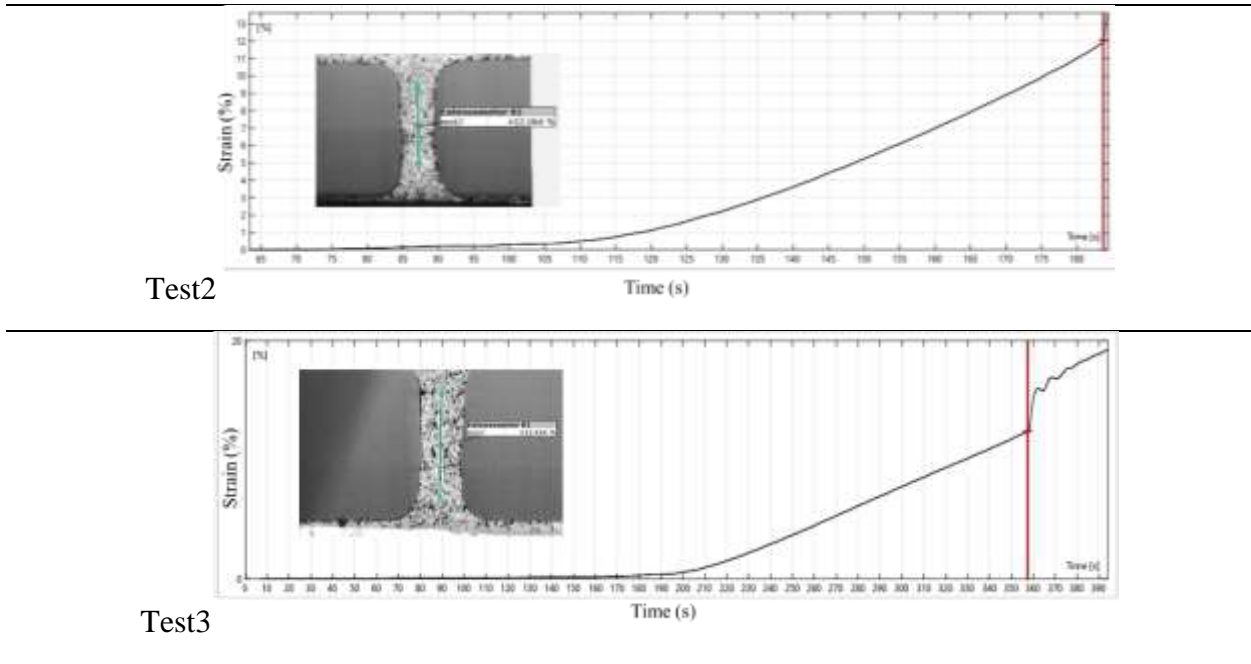
Fig. 6. Examples of intermediate strain rate tensile tests.

⁴ In this report, in all cases, the nominal strain rate can be calculated as the ratio of the cross-head velocity to the gauge length.

Table 3. Intermediate strain rate tensile test results.

Test ID	Yield stress (MPa)	UTS (MPa)	Fracture strain (mm/mm)
Test1	806.56	1109	0.1200
Test2	806.60	1124	0.1206
Test3	769.60	1142	0.1241
Average	794	1125	0.1215

Strain measurement using high-speed images and 2D DIC.



2.2.2 Experimental tests: Tensile tests at high strain rate region (SHTB tests)

The Split Hopkinson bar (SHB) method is a widely utilized experimental technique in the field of mechanical engineering and materials science for characterizing the dynamic mechanical behavior of materials, particularly under high strain rates. This method is particularly useful for studying the response of materials to impact, such as in ballistic testing, crashworthiness analysis, and understanding material behavior during high-speed machining processes.

The SHB apparatus typically consists of three main components: two long bars (referred to as the incident and transmission bars) and a specimen holder located between them. The incident

bar is typically connected to a gas gun or other device capable of imparting high-velocity impact, while the transmission bar is connected to a force transducer.

During an experiment using the SHB method, the incident bar is accelerated rapidly, causing it to impact one end of the specimen holder. This generates a high-speed stress wave that travels through the specimen. As the stress wave travels through the specimen, it experiences reflection and transmission at the interfaces between the specimen and the bars. These interactions are governed by the mechanical properties of the specimen, including its Young's modulus, Poisson's ratio, and yield strength. Figure 7 depicts the schematic presentation of a SHTB apparatus.

Split Hopkinson Tension Bar (SHTB) was utilized to perform tensile tests at high strain rates. The SHTB samples have the same design as presented in Fig. 5. However, the thickness of samples at the gauge area is reduced from 1.9 mm to approximately 1 mm. Strain waves on the input (incident) and output (transmitted) bars were acquired using the NI Daq board with a sampling rate of 1.25 Msamples/s.

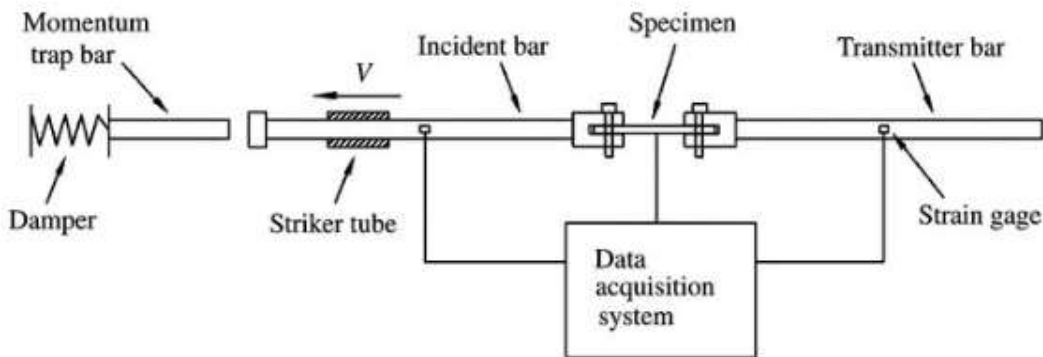


Fig. 7. Schematic presentation of SHTB.

The SHTB tests were performed under two distinct propellant pressures; (I) two bar pressure and three bar pressure. Subsequently, the samples underwent tensile loading at nominal strain rates of ~ 1500 1/s and ~ 2000 1/s. The incident, reflected, and transmitted strain signals are provided in the complementary Excel file.

Figure 8 illustrates the true stress-strain curves of the SHTB tests. Figure 9 shows one example of high-speed image processing that led to the calculation of fracture strain for different SHTB tests.

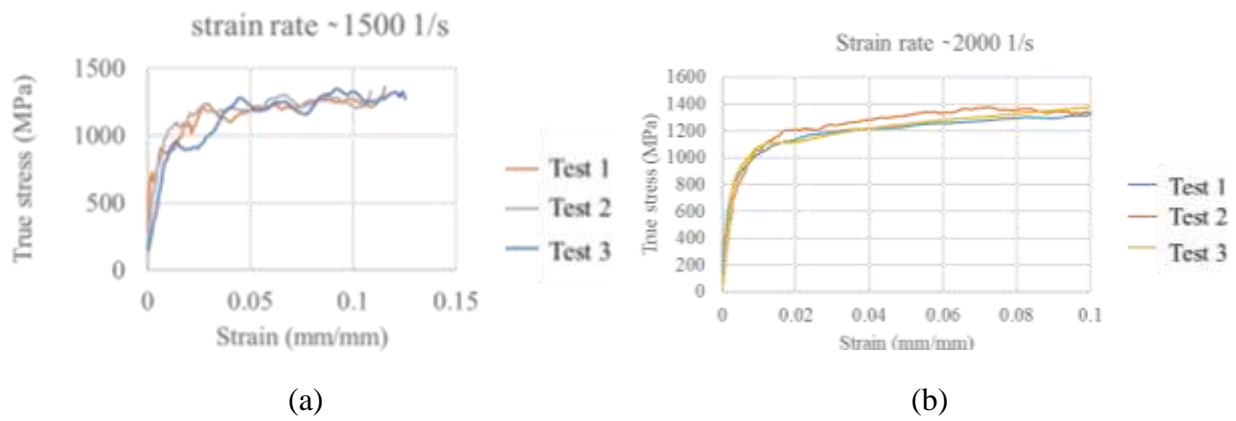


Fig. 8. SHTB test results; (a) Nominal strain rate 1500 1/s and (b) Nominal strain rate 2000 1/s.

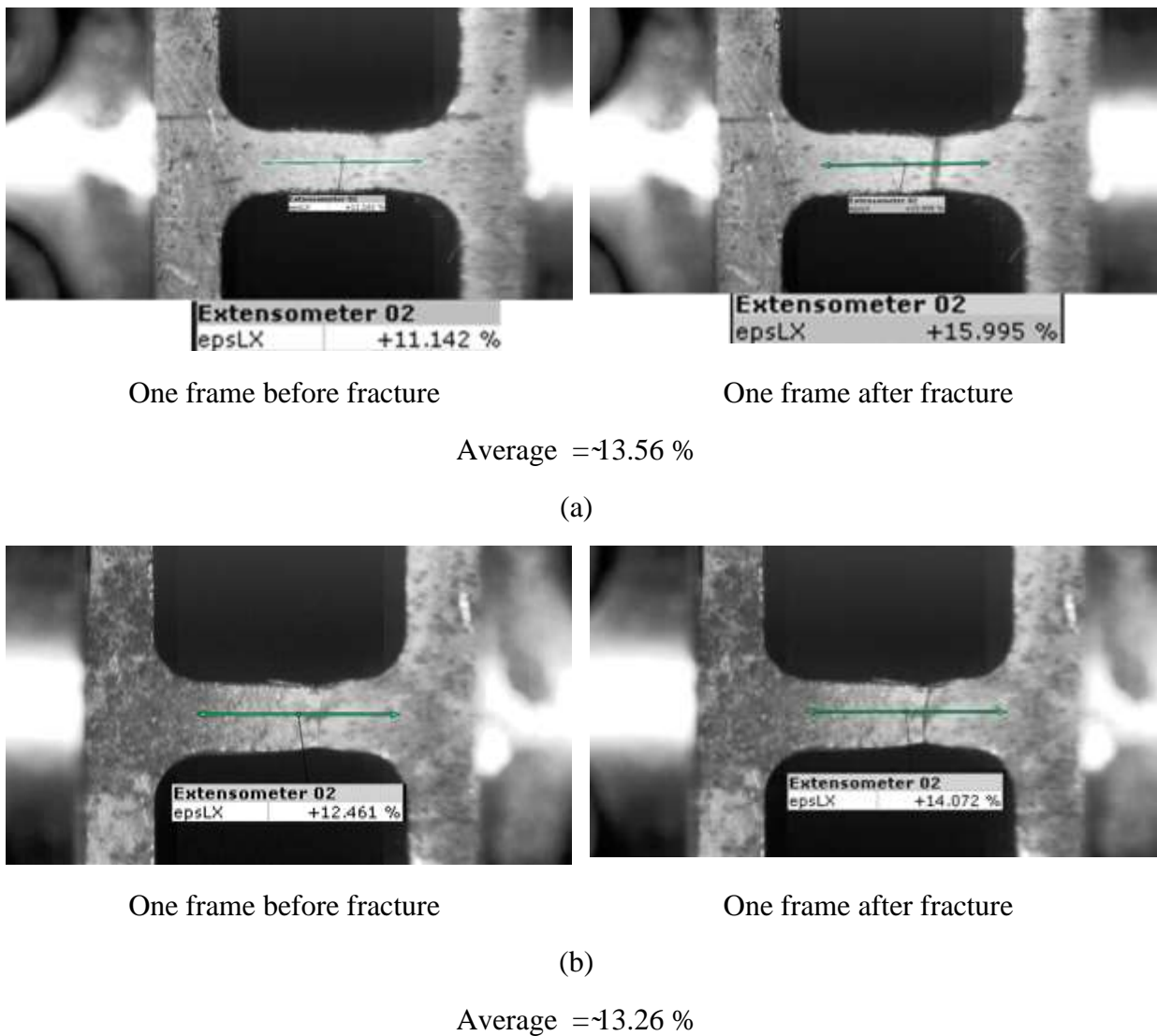


Fig. 9. Fracture strain in SHTB tests using high-speed images and virtual strain gauge; (a) Strain rate 2000 1/s and (b) strain rate 1500 1/s.

Note: The average fracture strain presented may be larger than the actual values due to the high-speed camera operating at 50 kfps.

2.2.3 Evaluating strain rate sensitivity parameter, C

For each strain rate, Fig. 8 displays three repetitions of the SHTB test to ensure testing reliability. However, for the evaluation of the C parameter, only one test of each loading rate was utilized. Figure 10 illustrates the estimation of the C parameter. The value for the C parameter was determined to be 0.0176, as indicated by Fig. 10.

Table 4 presents a summary of the values for the four parameters of the Johnson-Cook plasticity model.

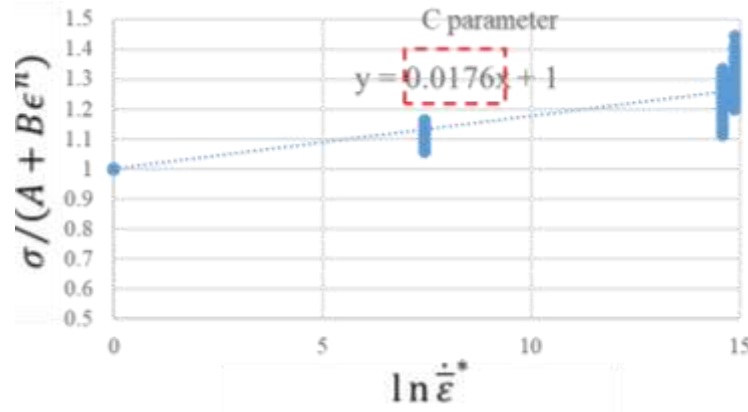


Fig. 10. Strain rate sensitivity parameter (c).

Table 4. Parameters of JC plasticity model.

A (MPa)	B (MPa)	n	C
748	960	0.4589	0.0176

The plastic stress-strain behavior of the tensile samples at higher strain rates is predicted by the Johnson-Cook (JC) model using the values presented in Table 4. These predictions are then compared to the experimental tests in Fig 11.

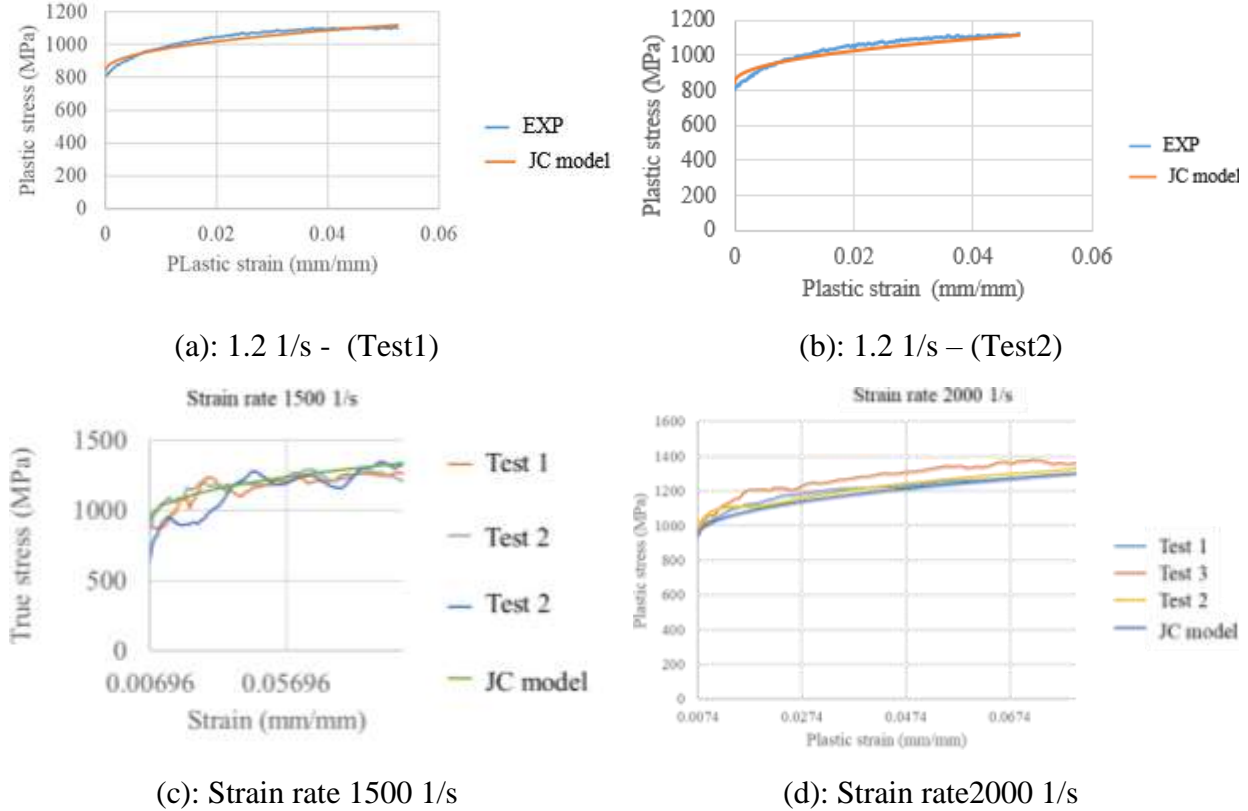


Fig. 11. Plastic stress-strain rate predicted by JC model and experimental tests.

2.3 Axial impact on tuvular steel componentns

A drop hammer rig was utilized to crush tubular specimens under various impact conditions. Three distinct impact scenarios were investigated, as outlined in Table 5. These scenarios were selected to subject the tubes to varying impact velocities and striker masses. It is noteworthy that Scenario II and III were engineered to produce identical impact energies, albeit with different striking velocities and inertia. Due to the absence of a trigger mechanism proposed for the axial impact tests, thickness reduction was considered for impact scenarios II and III to

mitigate damage to the impactor and anvil⁵. Considering tubes with both original thickness and those with reduced thickness will aid in a better calibration procedure of the finite element (FE) model in the future.

Table 5. Axial impact scenarios on tubes.

Parameter	Impact scenario		
	I	II	III
Impactor mass (kg)	120	55	120
Initial impact velocity (m/s)	10	9	6.5
Impact energy (kJ)	6.00	2.23	2.50
Tube initial length (mm)	140	120	120
Tube thickness (mm)	1.9*	1	1

Note: All values are nominal.

Note: Each testing condition is repeated at least three times to ensure test reliability.

* Tubes' original thickness

Figure 12 illustrates the setup of the drop hammer rig and the process of velocity measurement using image processing techniques. Impact events were recorded by a high-speed camera operating at either 40 kfps or 70 kfps. Calibrated images were then utilized to ascertain the velocity of the striker. Subsequently, acceleration and crushed distance were derived through post-processing steps utilizing the measured velocity data.

⁵ Even with thickness reduction, several impactors and anvil surfaces were damaged.

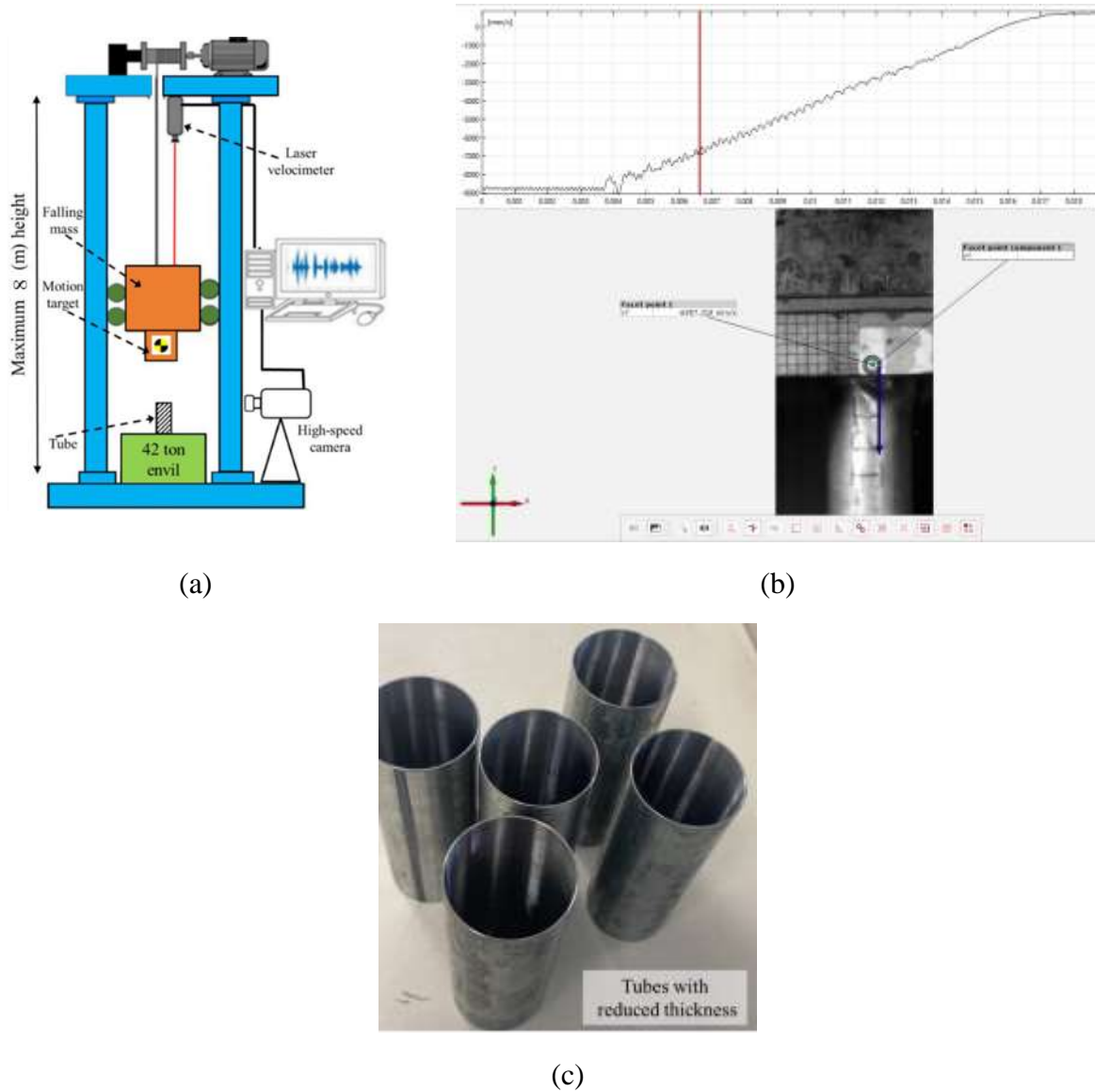


Fig. 12. Axial impact on the tube; (a) Schematic presentation of drop hammer rig, (b) Velocity extraction of the striker using high-speed image processing, and (c) Tubes with reduced thickness.

Figure 13 displays the force-displacement curves, which serve as the primary crashworthiness assessment tool, for all specimens. Additionally, Table 6 provides details regarding the peak force, average force, and maximum crush distance. The velocity and acceleration data for each test are included in the complementary Excel file.

The non-symmetric folding (diamond) mode was observed in all impact scenarios, as depicted in Fig. 14. However, the tube subjected to impact scenario I exhibited significant ruptures, as shown in Fig. 14(a).

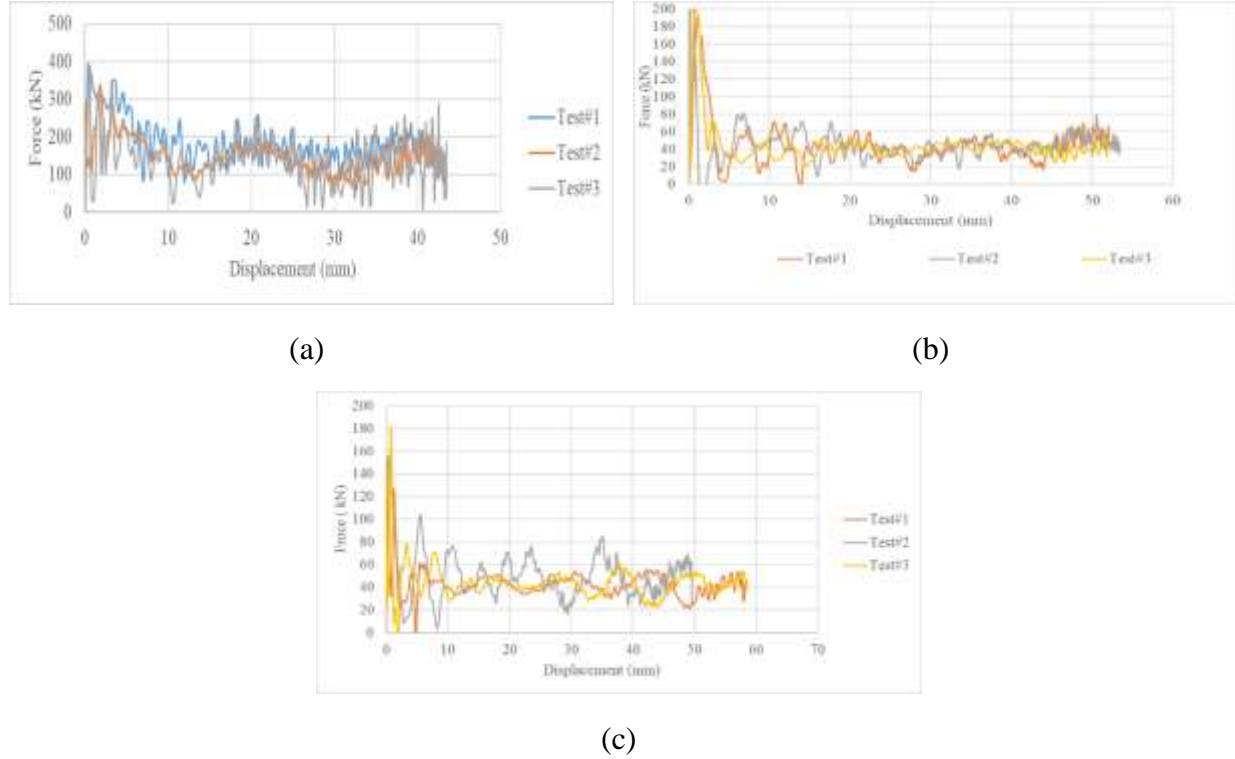


Fig. 13. Force-displacement curve of axial impact tests; (a) Impact scenario I,(b) Impact scenario II, and (c) Impact scenario III.

Table 6. Peak and average forces, crushed distance of axial impact tests on the tubes.

Impact scenario	Peak force (kN)	Mean force (kN)	Crushed length (mm)		Absorbed energy* (kJ)
			D1	D2	
I	Test 1	389.13	139.40	43.07	43
	Test 2	337.19	141.11	42.52	43 ~6.00
	Test 3	389.98	138.12	43.44	44
II	Test 1	192.46	42.97	51.98	52 ~2.23

Test 2	197.57	43.84	50.86	51	
Test 3	199.75	43.05	51.79	49	
Test 1	141.17	42.91	58.26	58	
II Test 2**	155.91	50.52	49.48	50	~2.50
Test 3	181.31	42.74	58.48	58	

* It is assumed that all input energy is absorbed by the tube since the impactor rebounding was negligible.

** Initial tube length was equal to 100 mm.

D1 = displacement calculated from the measured velocity

D2 = Post-impact physical displacement measured (± 1.5 mm)



(a)





(c)

Fig. 14. Non-symmetric (diamond) folding of all tubular components subjected to axial impact load; (a) Impact scenario I, (b) Impact scenario II, and (c) Impact scenario III.

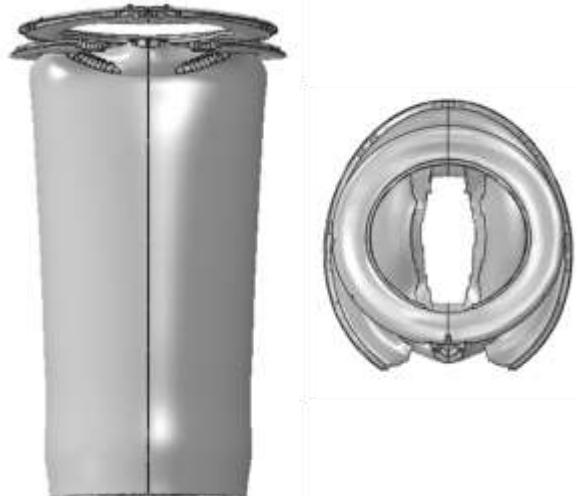
3. Summary

The Johnson-Cook plasticity parameters (A, B, n, and C) are determined through the characterization of specimens cut from tubular components. Parameters B, n, and C can be calibrated for a numerical model (FE model) by utilizing the results of both tensile tests and axial crushing tests conducted on the tubes.

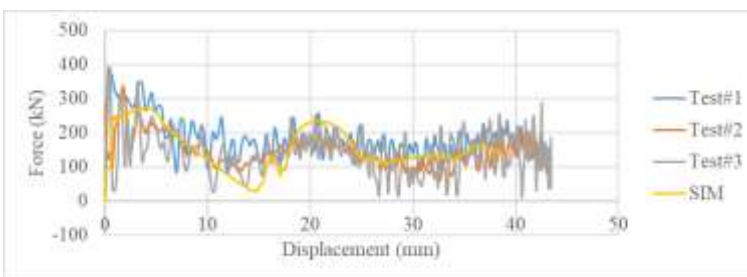
References

Dassault Systèmes Simulia. (2014). *Abaqus 6.14. Analysis User's Guide*.
<https://doi.org/10.1017/CBO9781107415324.004>

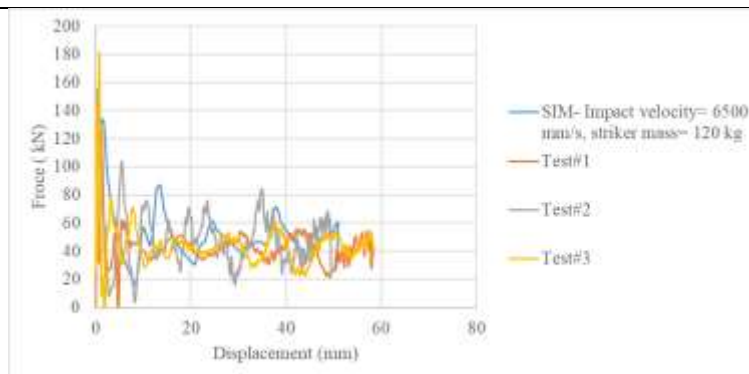
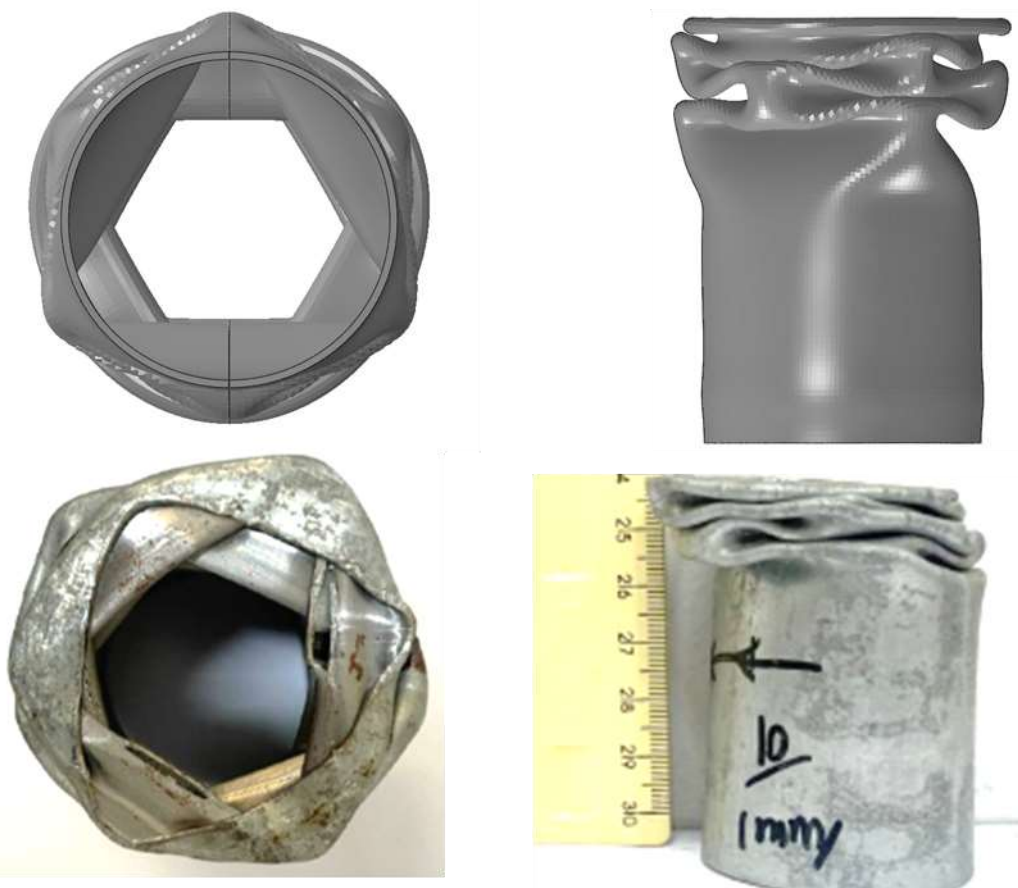
FE model of axial impact on tubes and Split Hopkinson tensile bar were developed in Abaqus. Here are a few comparisons between numerical and experimental results.



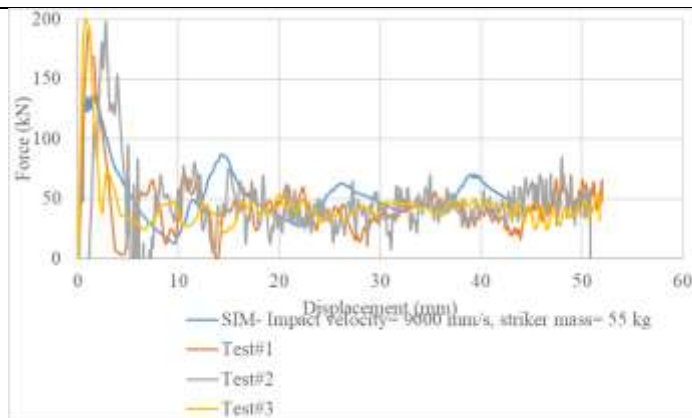
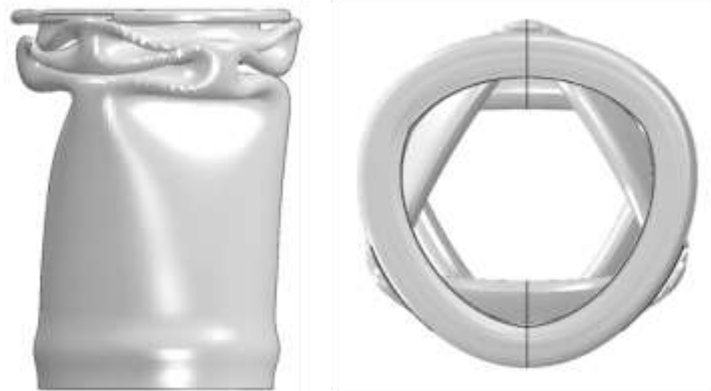
Numerical simulation



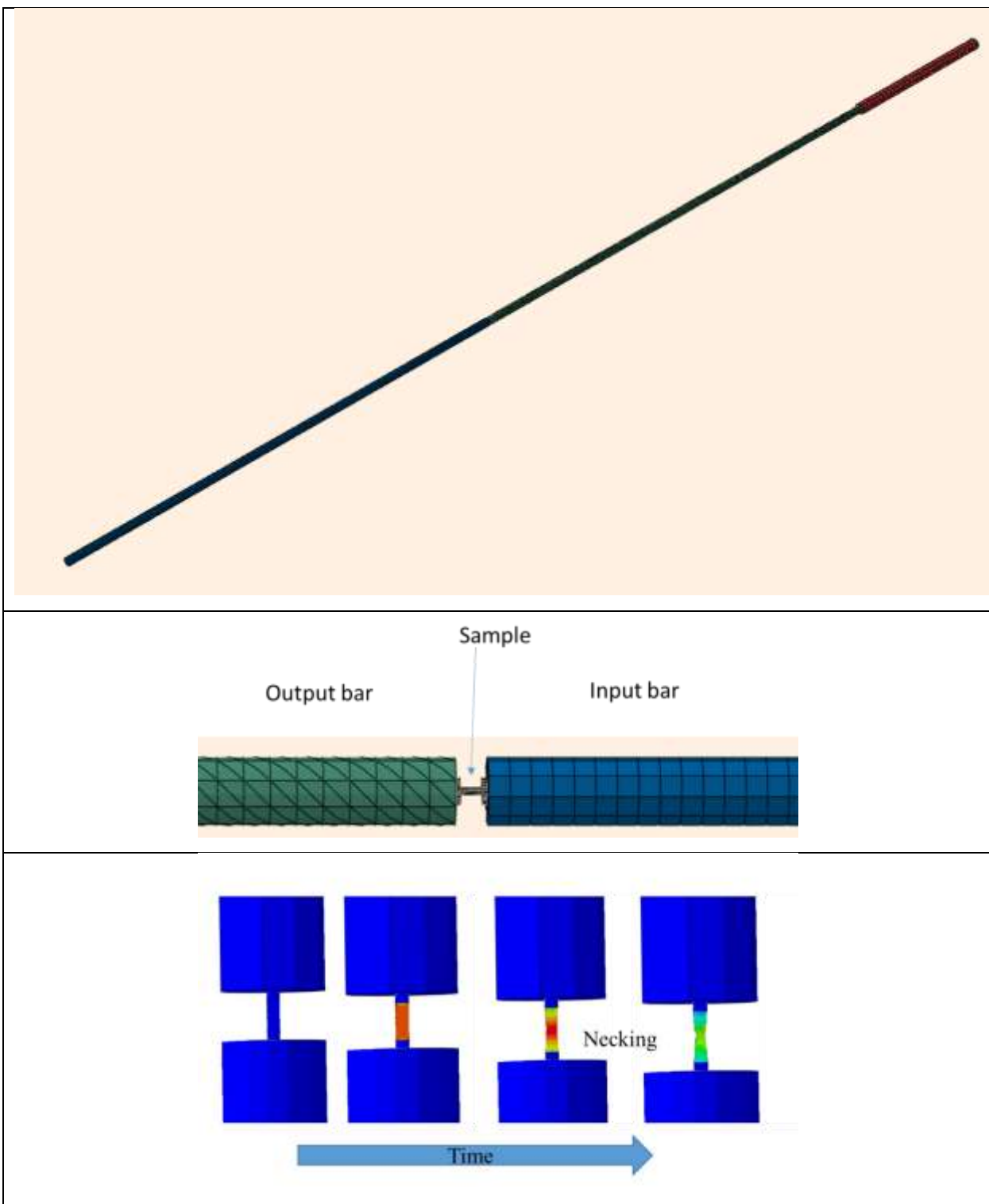
Axial impact on tube 9.5 m/s impact velocity.

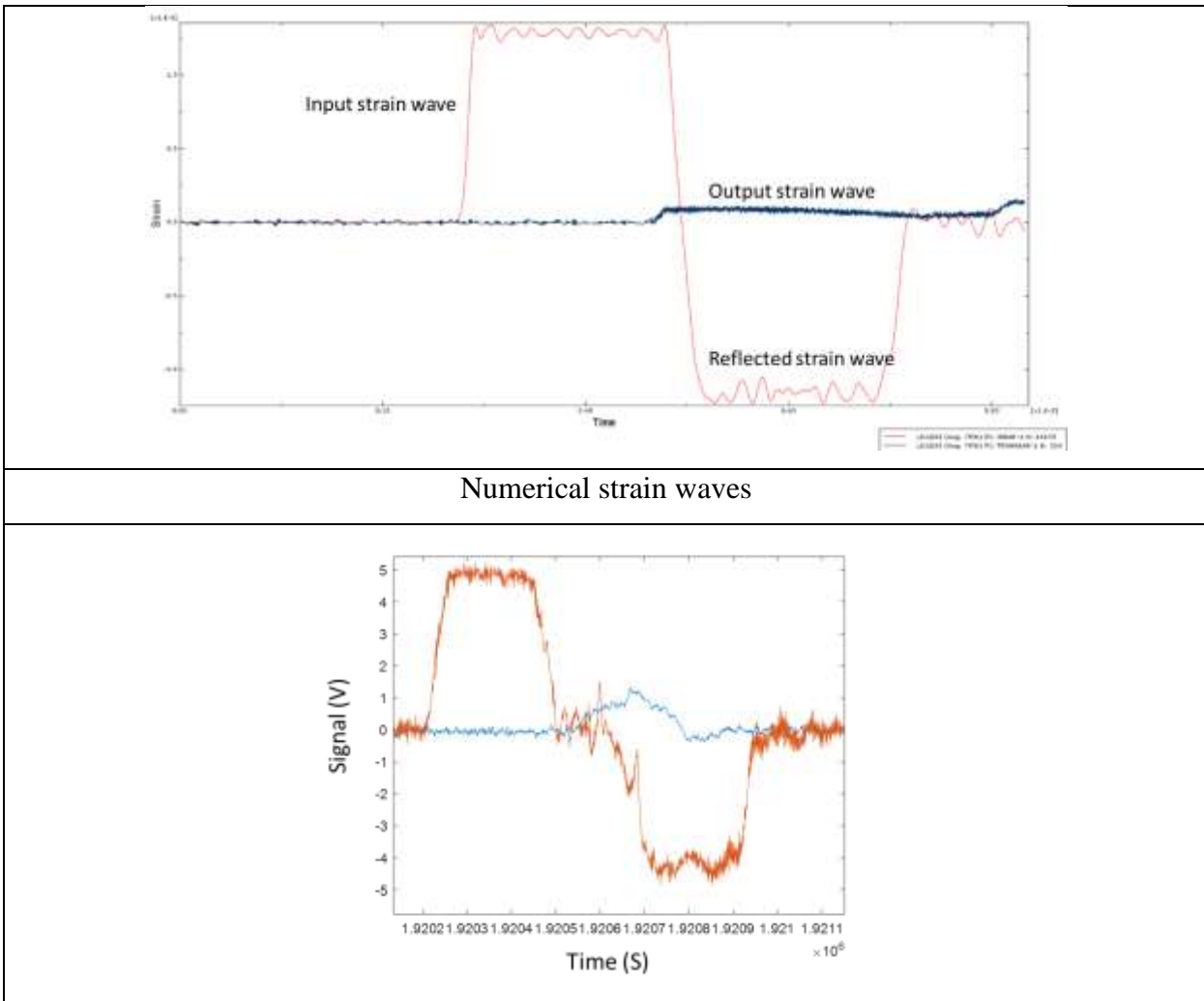


Axial impact on tube 6.5 m/s impact velocity.



Axial impact on tube 9 m/s impact velocity.





Numerical strain waves

SHTB numerical model vs experimental

Part 4



Quasi-static and dynamic tensile behavior of DP and TRIP steels at room temperature

Conducted by Dr. Pouria Bahrami
Supervised by Prof. Dr. Marcilio Alves

March 2023

GMSIE laboratory

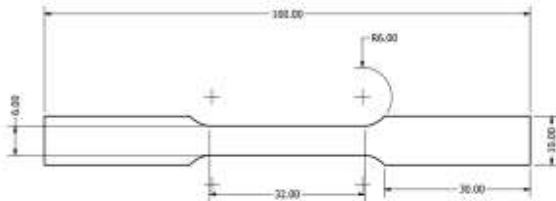
Overview

- Quasi-static tensile test
 - Objective: Johnson-Cook Strain hardening parameters (A, B, n) from Qs tests

 - High strain rate tensile test
 - Objective: Johnson-Cook Strain rate hardening parameter (C) from SHTB tests
-

Quasi-static tensile test

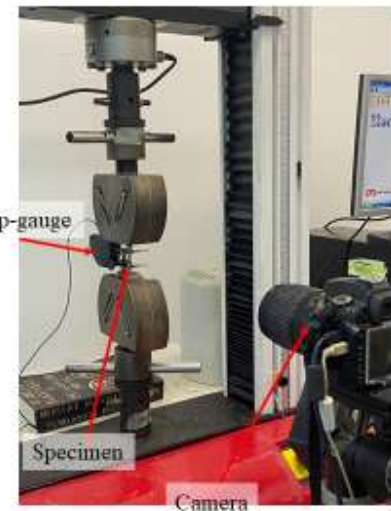
Specimens, sample dimensions based on Standard Test Methods for Tension Testing of Metallic Materials, ASTM E8



Test velocity

The quasi-static tests were conducted at constant velocity

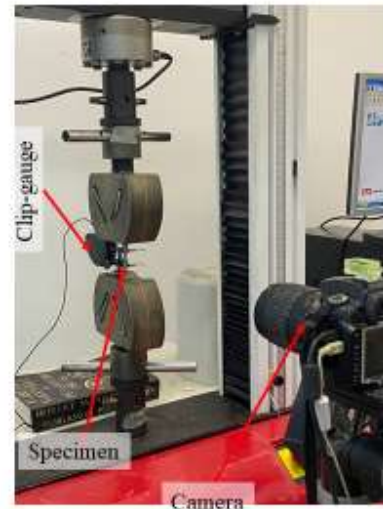
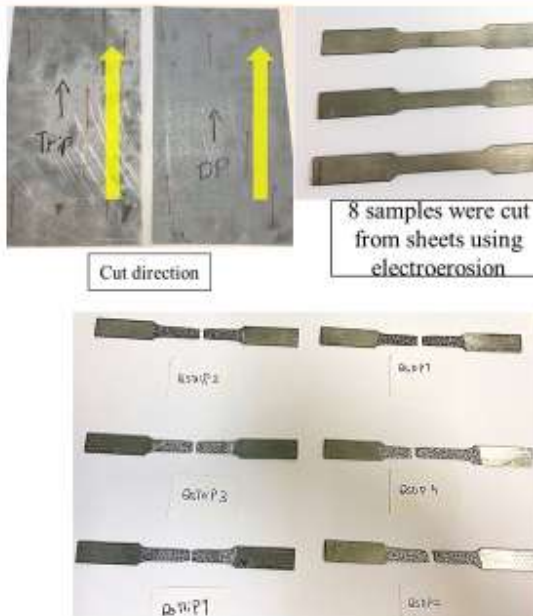
$$\text{nominal strain rate, } \dot{\varepsilon} = \frac{\text{Velocity}}{\text{Gauge length}}$$
$$0.003 \text{ (1/s)} = \frac{\text{velocity}}{25 \text{ mm}} \rightarrow \text{velocity} = 0.075 \text{ (mm/s)}$$



3

Quasi-static tensile test

Specimens

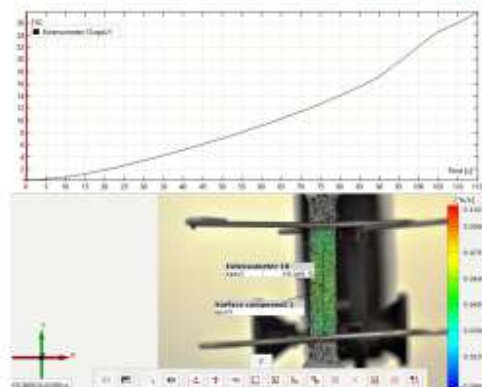


4

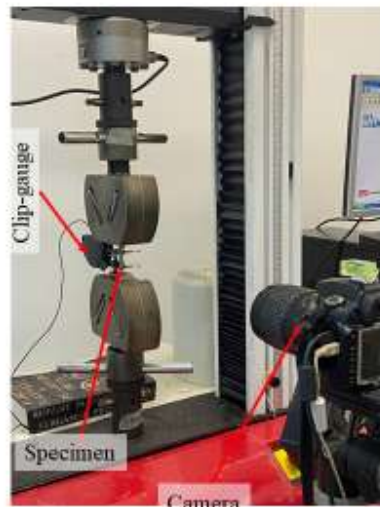
Quasi-static tensile test

Strain measurement

2D DIC, Digital Image Correlation
and clip gauge were used to measure strain



Play it! 2D DIC

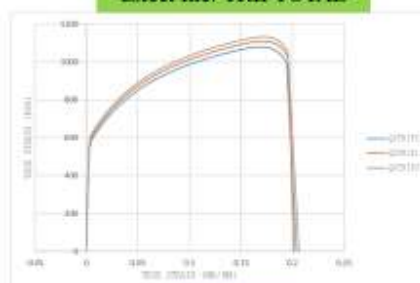


5

Quasi-static tensile test

Results overview

Excel file: TRIPTOTAL



TRIP steel

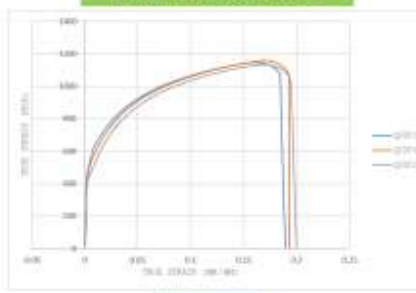
Test ID	ELASTIC MODULUS (GPa)	YIELD STRESS (MPa)	STRAIN @ YIELD (MM/MM)	MAX STRESS (MPa)
QSTRIP1	213.66	594.23	0.00478	1110.18
QSTRIP2	213.63	583.77	0.00488	1080.24
QSTRIP3	228.80	612.47	0.00469	1133.38
Average	218.70	596.82	0.00478	1107.93

6

Quasi-static tensile test

Results overview

Excel file: TOTALDP



DP steel

TEST ID	CROSSHEAD VELOCITY (MM/S)	NOMINAL STRAIN RATE	SAMPLE GL (MM)	ELASTIC MODULUS (GPA)	YIELD STRESS (MPA)	STRAIN @ YIELD (MM/MM)
QSDP4	0.075	0.003	25	212.87	489	0.00430
QSDP3	0.075	0.003	25	215.66	500	0.00399
QSDP2	0.075	0.003	25	217.15	-	-
AVERAGE				215.22	494.50	0.00415

7

Quasi-static tensile test

Johnson-Cook parameters from Qs tests

Strain rate hardening

II

$$\sigma_y = (A + B\varepsilon^n)(1 + C\ln(\dot{\varepsilon}^*))^{(1 - T^{+m})}$$

I

Strain hardening

III

Thermal softening

8

Quasi-static tensile test

Johnson-Cook parameters from Qs tests

$$\sigma = (A + B\varepsilon^n)(1 + C\ln(\dot{\varepsilon}^*))^{(1 - T^{*m})}$$

Strain rate hardening
II
I Strain hardening III Thermal softening

Finding strain hardening parameters (A, B, n)

A: Yield stress, B: Strain hardening modulus, n: Strain hardening exponent

Assumptions
Test @ room temperature (reference temp) $\rightarrow m = 0$ (Thermal softening parameter)
 $\dot{\varepsilon}^* = \frac{\dot{\varepsilon}}{\dot{\varepsilon}_{ref}} = 1 \rightarrow C = CLn(\dot{\varepsilon}^*) = 0$ (Strain rate hardening parameter for QS tests)

9

Quasi-static tensile test

Johnson-Cook parameters from Qs tests

$$\sigma = (A + B\varepsilon^n)(1 + C\ln(\dot{\varepsilon}^*))^{(1 - T^{*m})}$$

Strain rate hardening
II
I Strain hardening III Thermal softening

Finding strain hardening parameters (A, B, n)

$$\ln(\sigma - A) = n\ln(\varepsilon_p) + \ln(B) \longrightarrow$$

- Step-by-step
1. Drawing $\ln(\sigma - A)$ vs $\ln(\text{plastic strain})$ curve
 2. Slope of the linear trend-line of $\ln(\sigma - A)$ vs $\ln(\text{plastic strain})$ curve is n parameter and $\ln(B)$ parameter is its constant value

$$\text{Effective plastic strain } \varepsilon_p = \ln(1 + \varepsilon_E) - \frac{\sigma_{True}}{\text{Elastic modulus}}$$

$$\text{Total engineering strain } \varepsilon_E$$

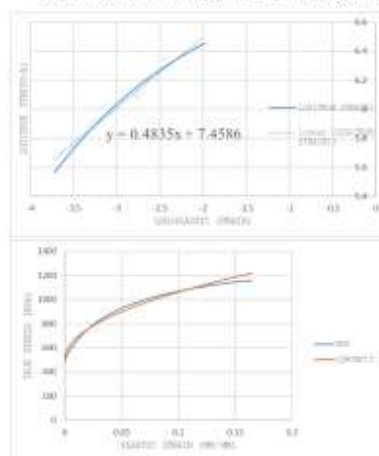
10

Quasi-static tensile test

Johnson-Cook parameters from Qs tests

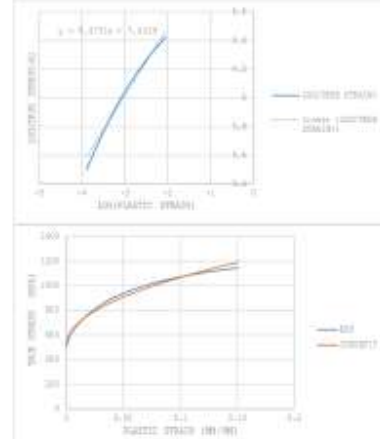
Strain hardening parameters (A, B, n) for DP steel

$$\sigma_y = (A + B\dot{\varepsilon}^n)(1 + Cln(\dot{\varepsilon}^*))^{(1 - T^{+m})}$$



A (Mpa)	B (Mpa)	n
489.51	1734.7	0.4812

QSDP4



A (Mpa)	B (Mpa)	n
500	1690.70	0.4731

QSDP3

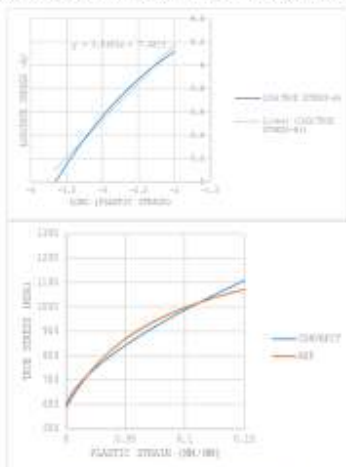
11

Quasi-static tensile test

Johnson-Cook parameters from Qs tests

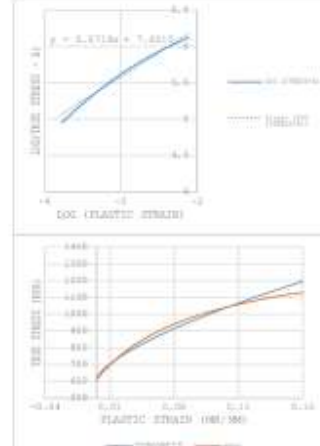
Strain hardening parameters (A, B, n) for TRIP steel

$$\sigma_y = (A + B\dot{\varepsilon}^n)(1 + Cln(\dot{\varepsilon}^*))^{(1 - T^{+m})}$$



A (Mpa)	B (Mpa)	n
589	1774.90	0.65

QSTRIP2

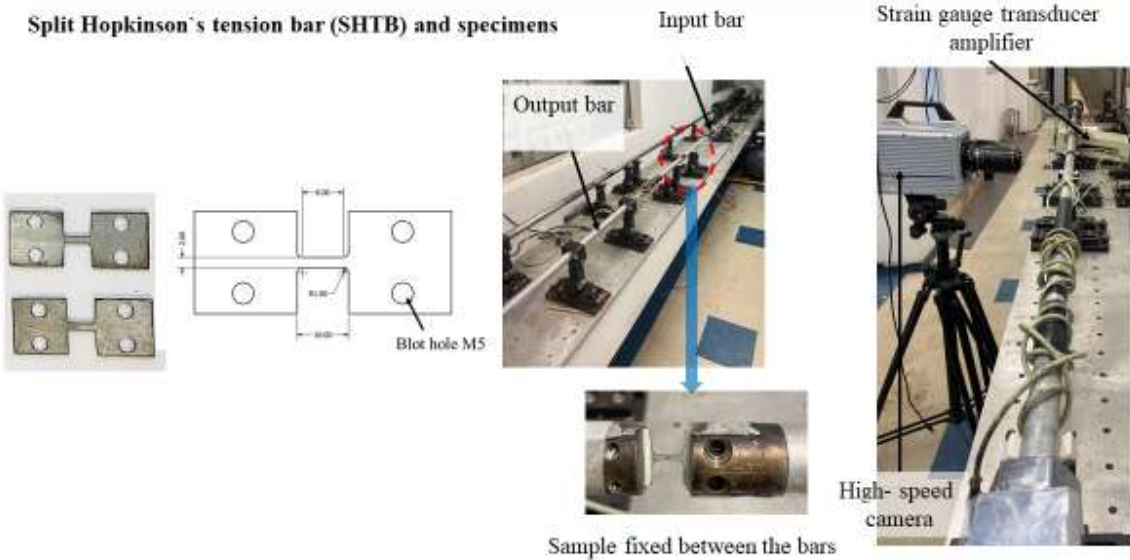


A (Mpa)	B (Mpa)	n
612.47	2001.195	0.6719

QSTRIP3

12

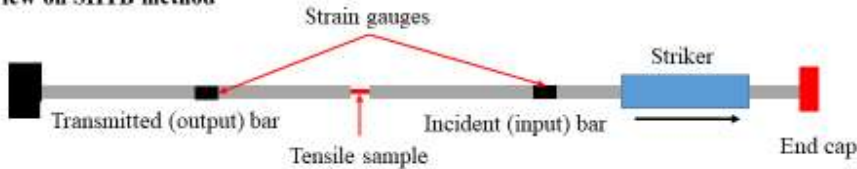
High strain rate tensile test



13

High strain rate tensile test

Brief overview on SHTB method



1. Launch the striker to hit the end cap of incident bar
2. Impact on the end cap, generates a longitudinal tensile stress wave in incident bar
3. Stress wave reaches the specimens and the specimen undergoes tensile tension
4. A part of the stress wave will transmit to the output bar and a part reflects back to input bar
5. These three strain waves, incident (ε_i), reflected (ε_r) and transmitted (ε_t), will be acquired by strain gauges
6. Stress-strain response of the specimens will be calculated using the following Eqs

$$\text{Eq 1: Tensile stress: } \sigma = (E) \frac{A_{\text{bar}}}{A_{\text{sample}}} \varepsilon_t$$

$$\text{Eq 2: Strain rate: } \dot{\varepsilon} = - \frac{2C}{L_{\text{sample}}} \varepsilon_r, C \text{ is speed of sound in the bars}$$

$$\text{Eq 3: Strain: } \varepsilon = - \frac{2C}{L_{\text{sample}}} \int_0^t \varepsilon_r dt, C \text{ is speed of sound in the bars}$$

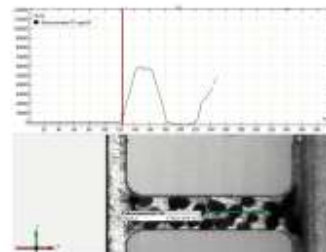
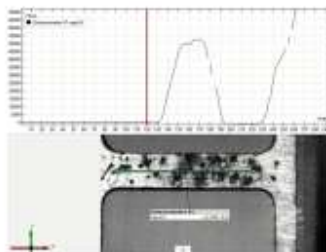
Bars properties	
E	7.17E+10 Pa
ρ	2810 kg/m ³
C	5051.338 m/s
A_{bar}	4.91E-04 m ²

14

High strain rate tensile test

Strain rate check

Method I



Using high-speed camera (with 100kfps) and digital extensometer

Method II

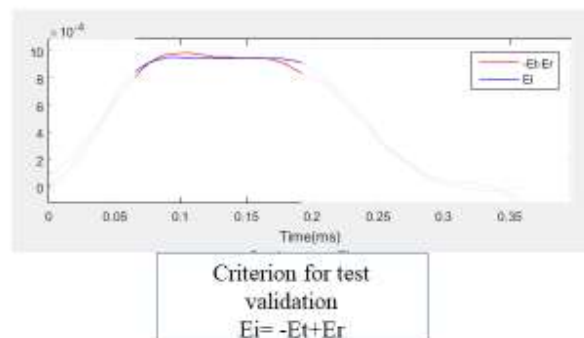
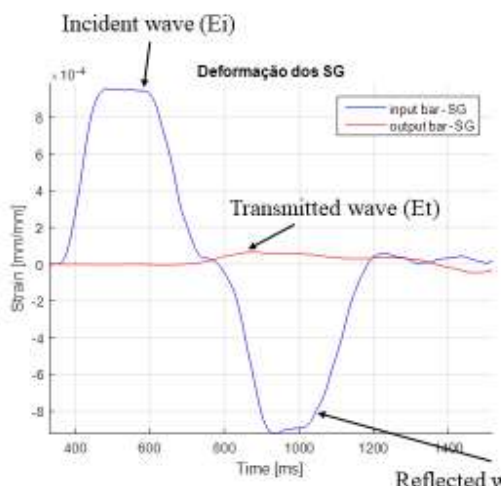
$$\text{Average value of Eq.2 } (\dot{\varepsilon} = -\frac{2C}{L_{sample}} \varepsilon_r)$$

The strain rates measured using digital extensometer were close to the target strain rate (500 (1/s)).
However, strain rate measured using eq.2 was higher than the target value (average 700 (1/s)).

15

High strain rate tensile test

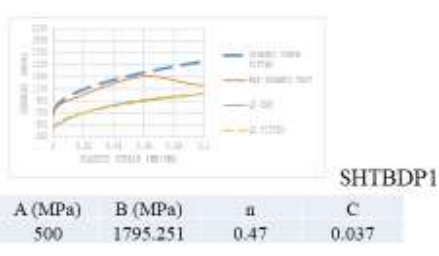
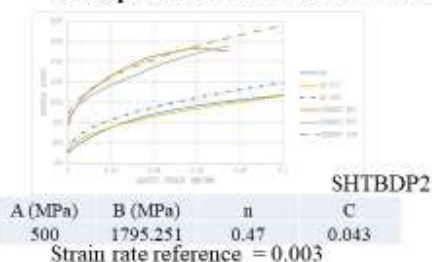
One example of incident, reflected and transmitted signals (SHTBDP1)



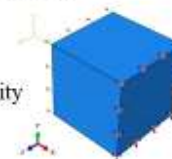
16

High strain rate tensile test

Stress-plastic strain curves for DP steel and value predicted for C (strain rate hardening) parameter



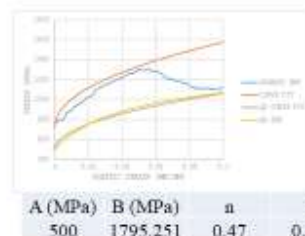
Tensile simulation with JC model



Abaqus/explicit simulation with 500 mm/s velocity on a single solid element

Abaqus/standard simulation with 0.003 mm/s on a single solid element

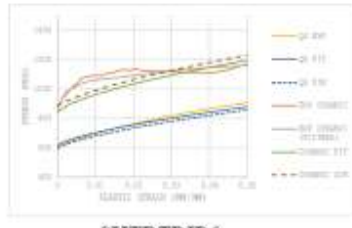
- Reasonable correlation between dynamic simulation and experiment test.
- Difference between simulation stress-strain curve and experimental quasi-static test is remarkable



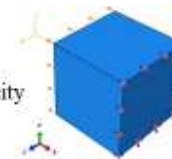
17

High strain rate tensile test

Stress-plastic strain curves for TRIP steel and value predicted for C (strain rate hardening) parameter

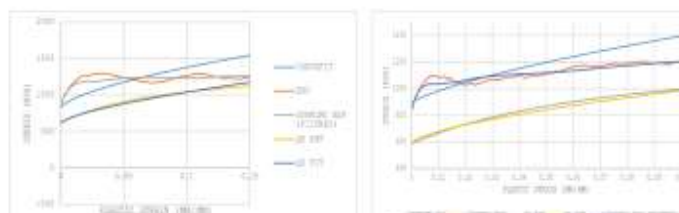


Tensile simulation with JC model



Abaqus/explicit simulation with 500 mm/s velocity on a single solid element

Abaqus/standard simulation with 0.003 mm/s on a single solid element



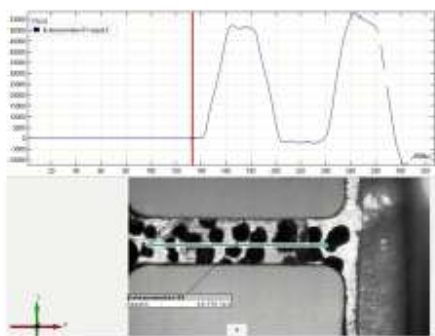
SHTBTRIP3

A (MPa)	B (MPa)	n	C
589	1774.90	0.6492	0.032

A (MPa)	B (MPa)	n	C
589	1774.901132	0.6492	0.032

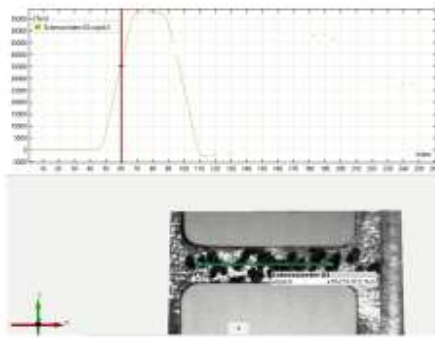
Appendix

Video extensometer



SHTBTRIP5

Strain rate = $\sim 500 \left(\frac{1}{s}\right), 50000 \left(\frac{\%}{s}\right)$



SHTBTDP2

Strain rate = $\sim 550 \left(\frac{1}{s}\right), 55000 \left(\frac{\%}{s}\right)$